AGGREGATION AND GELATION OF SILICA NANOPARTICLES

by

XIUJUAN CAO

A Dissertation Submitted to the Graduate Faculty in Engineering in Partial
Fulfillment of the Requirements for the Degree of Doctor of Philosophy
The City University of New York

2011

This manuscript has been read and accepted for the Graduate Faculty in Engineering in satisfaction of the dissertation requirement for the degree of Doctor of Philosophy.

Date	Prof. Jeffrey F. Morris Chair of Examining Committee
Date	Prof. Mumtaz Kassir Executive Officer

Prof. Morton Denn

Prof. Charles Maldarelli

Prof. Alexander Couzis

Prof. Jiufeng Tu

Supervision Committee

THE CITY UNIVERSITY OF NEW YORK

Abstract

Aggregation and gelation of silica nanoparticles

by

Xiujuan Cao

Advisor: Jeffrey F. Morris

The gelation mechanism was explored in a comprehensive way both experimentally and numerically. The gelation dynamics of a sol of colloidal silica of approximately 7 nm radius particles is studied using a combination of light scattering and rheometry. By changing the ionic strength (by addition of a salt solution resulting in different ultimate molarities) of the mixture, a stable sol can be destabilized, leading to aggregation and later gelation. The gel time t_{gel} can be varied from hours to weeks, indicating a reaction-limited aggregation process. Static light scattering is used to extract the fractal dimension D_f of the aggregates, which is found to be approximately 2. The evolution of cluster size is probed by dynamic light scattering, and follows an exponential growth. Rheometry is used to assess the gelation time and further development of the network strength after gelation. The elastic modulus (G') is found to scale as $G' \sim \phi^{3.3}$, where ϕ is the silica particle volume fraction. It was observed that the gel time (after salt solution addition) depends on both the particle volume fraction and salt concentration, showing a divergence at low volume fraction or low salt concentration. For a single solid fraction, data for the cluster hydrodynamic radius, normalized by the single particle radius, from experiments with a wide range of gel times can be collapsed onto a master curve when the time after the salt addition, t, is scaled as t/t_{gel}; a similar collapse of viscosity and the linear viscoelastic data after gelation can be obtained using the same scaling of time. Salt concentration affects the gel time but not the strength of the gel network, thus allowing very accurate prediction of network formation times and mechanical properties.

The effects of both hydrodynamic and repulsive forces on the rate of aggregation, and on the microstructure and mechanical properties of particle aggregates, are investigated by Brownian dynamics (BD) and Stokesian Dynamics (SD) simulation, over a range of solid volume fraction of $0.04 \leq \phi \leq 0.12$. The simulation methods differ in their treatment of the role of the suspending fluid, as SD includes the configuration-dependent hydrodynamic interactions between particles, whereas BD includes the fluid only though a viscous drag independent of configuration. Typical simulations use $O(1000)$ particles in the simulational unit cell, which is periodically replicated in three dimensions. The interparticle potential is parameterized to include a roughly constant primary minimum near contact with $U_{min}/k_BT > 6$, along with a variable repulsive barrier at slightly larger separations; here U_{min} is the depth of the primary minimum. The structure is characterized through the pair distribution function, $g(r)$, and the static structure factor. The repulsive barrier reduces the rate of aggregation and is also seen to affect the structure, with a large repulsion associated with a more tenuous structure. This is reflected in the potential having a strong effect on the evolution of 'bonds' per particle (defined by a pair of particles being inside the repulsive barrier), with larger repulsion leading to smaller numbers of bonds and hence a more loose and open structure. Hydrodynamics was found to reduce the solid fraction required for percolation, with the influence depending upon the form of the potential; the difference in percolation threshold was significant, $\phi_{c,SD} \doteq 0.06$ and $\phi_{c,BD} \geq 0.08$ for an intermediate level of repulsive force, where the largest fractional difference is observed. The hydrodynamic interactions were examined through analysis of the statistics of the evolution of numerous independent three-particle aggregates. These show that hydrodynamics slows the evolution toward a condensed aggregate of lowest potential energy in a way which cannot be simply scaled by altering the local drag.

The interparticle bonding potential was investigated in a two dimensional system with or without restrictions in the rotational and stretching motion of particles. Two types of non-restrictive bonding force were studied, FENE (finitely extensible nonlinear elastic) and spring potential. Both of the bonding forces are effective in binding two particles together and forming clusters with chain-like structure under the condition that there is no repulsive barrier between particles. However, in the presence of repulsive force, systems with FENE bonding potential form clusters without branched structure; while with spring potential, particles form chain-like clusters which interconnect with each other and evolve into large clusters filling the whole space. In addition, we introduced a spring type of bonding potential that is created on the surface of the two particles within the critical distance instead of the center. The particle pair is restrained in both translational and rotational motion. The particles with high repulsive force form one dimensional chain-like structure. The restrictive bonding potential is also investigated in three dimensional system. We found that only the systems with small repulsive barriers together with restrictive bonding for volume fraction $\phi = 0.1$ can form a percolated network at aggregation time $t = 33$.

Contents

List of Tables

List of Figures

Chapter 1

Introduction

1.1 Basic concepts in gelation

Gel is a material state between solid and fluid. Elasticity is one of its most important mechanical properties, which is strongly related with its structure. We are particularly interested in colloidal silica gel, which forms from silica particles of nanometer or micron scale, in an aqueous dispersion. The aggregation of particles leads to the formation of particle network, which is very tenuous at the gel point and becomes stiffer after more particles and particle clusters attach to the network. The systems display solid-like characters with diverging viscosity [8, 9], a finite yield stress [10] and a low-frequency elastic modulus [11]. The disturbance of a stable colloidal suspension can be caused by the addition of ions, change of charges on the particle surface, by altering pH or by changing temperature. The intrinsic mechanism proposed by Larson [1] with a slightly change in the secondary potential minimum is as follows (see Figure 1.1): The total interaction potential energy consists of double-layer repulsion and van der Waals attraction. The height of repulsive barrier in the total energy curve changes with the particle surface charge, electrolyte concentration and pH. At low electrolyte concentrations, the repulsive barrier prevents particles from aggregating. When a high concentration of electrolyte is added to the suspension, the double layer is compressed (see the inset of Figure 1.1). The thermal energy is enough to activate particles to overcome the repulsive barrier, resulting in aggregation [12]. When the attractive potential minimum (U_{min}) is large, $-U_{min}/k_BT \gg 1$ (k_B is the Boltzman constant; and T is the absolute temperature), once particle-particle contacts are formed, they are released by thermal agitation so infrequently that particle rearrangements are strongly suppressed [1].

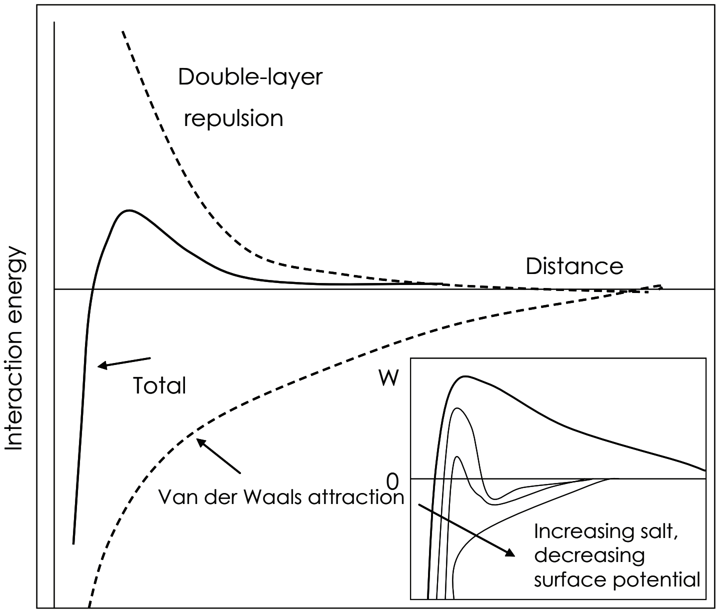

Figure 1.1: Interaction energy as function of particle separation. Ref. [1]

Many studies on the behavior of attractive colloids have been carried out in dispersions with depletion forces [13, 14, 6]. Depletion forces between colloidal particles are induced from dissolved polymer exclusion from the gap between a pair of surfaces, which results in an osmotic force pushing the pair forward contact. One advantage of such systems is that the range and the depth of the potential can be adjusted easily. Prior work has shown the existence of a systematic $\phi - U$ boundary (ϕ is the volume fraction and U is the interaction energy) between fluid-like and space-spanning soft solid. Based on previous studies on aggregation and gelation, a

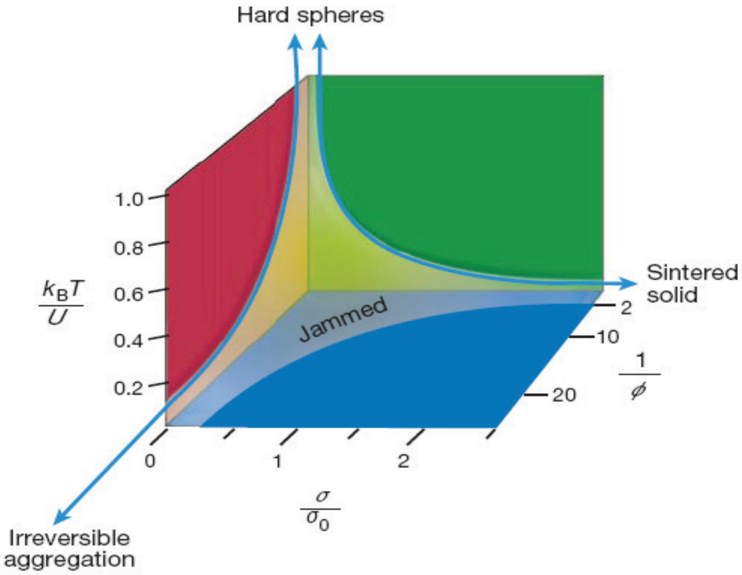

Figure 1.2: Composite jamming phase diagram for attractive colloidal particles (Ref. [2]).

phase diagram for attractive particles (see Figure 1.2) was proposed [2]. This diagram captures the common features of fluid to solid translations, by unifying the behavior as a function of the particle volume fraction, the energy of interparticle attractions, and the applied stress.

1.1.1 Applications

Colloidal dispersions have many applications in industry, such as ceramic processing, polymer materials, pharmaceutical products, food technology, aerosols, and paints [15, 16, 17, 18, 19]. In addition, in the scientific area, colloidal dispersions are good model systems for investigating multibody interactions and phase transitions [20]. In some industrial applications, e.g. coatings or spaying, a gel-like state is desirable due to its uniform distribution of particles, which promotes uniform particle coverage. In some products, certain rheological properties of gel are needed for quality, performance and long shelf-life.

1.1.2 Permanent and transient gels

Based on its state of stability, gels can be categorized into permanent gels and transient gels. In the process of forming a permanent gel, particles stick to each other strongly and form permanent fractal aggregates. Those aggregates gradually evolve and form an interconnected network, which finally fills the whole space and forms an irreversible gel. Irreversible aggregation and gelation, observed through computer simulation [21], is simply due to the result of random irreversible collisions. The aggregation of a charge-stabilized colloidal suspension destabilized by the addition of excess electrolyte is close to the behavior of irreversible aggregation. A transient gel, on the other hand, is formed by a rather weak and reversible bond between particles. When the interparticle bond energy is of the order of thermal energy kT, the colloidal aggregation can be regarded as fully reversible [22]. Weak gels formed by depletion or polymer bridging display yield stress and a strong shear-thinning. Under certain situation, it is very hard to distinct between those two gels. Transient gels may form strong attractive forces and remains stable for a long time before collapse. On the other hand, irreversible gels may deform or rearrange under shear-induced bond-breaking.

1.1.3 Fractal aggregates and gels

Particle aggregates and gels from homogeneously distributed colloidal suspensions usually form self-similar fractal objects. A scaling parameter D_f, the fractal dimension, describes the relation between the number of primary particles N in an aggregate of average radius R:

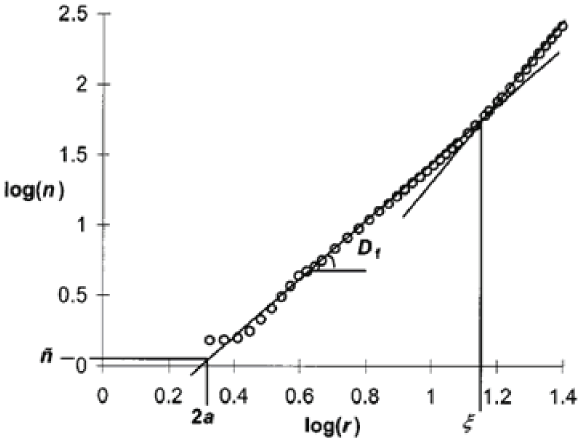

Figure 1.3: Example of a determined number correlation function $n(r)$, indicating how the fractal parameters are derived. Volume fraction $\phi = 3.4$ %. Ref. [3].

$$N \sim (R/a)^{D_f}, . \tag{1.1}$$

where a is the radius of the primary particle. For close packed systems, $D_f = 3$, while for the fractal systems, $D_f < 3$. There are two limits of aggregation mechanism which have been well-studied both experimentally and by numerical modeling. The first case is diffusion-limited cluster aggregation (DLCA), where particles stick together after one collision, so called fast aggregation. In irreversible fast aggregation, a typical value of D_f is about 1.8. The other limit is reaction-limited cluster aggregation (RLCA), where particles form bonds with a probability less than unity in each collision and have a chance to explore the interior parts of the aggregates. This type of aggregation is called slow aggregation, where D_f is about 2.1. For fractal objects, the mass of the cluster grows less rapidly with linear size, compared with the close-packed clusters.

It has been shown [23, 22] that for a fractal gel, the particle-particle distribution $g(r)$ has the following relationship with r over a certain spatial scale:

$$g(r) = (r/\xi)^{D_f - 3}, \tag{1.2}$$

where the parameter ξ is a characteristic correlation length beyond which the structure becomes homogeneous ($g(r) \to 1$). According to Mellema *et al.* [3], at the gel point, ξ equals to the critical cluster size R_c. In an attempt to smooth out the short-ranged liquid-like oscillations in $g(r)$, the authors integrated the pair distribution function [24],

$$n(r) = 4\pi\rho \int_0^r s^2 g(s) ds, \tag{1.3}$$

where $n(r)$ is the average number of particles within range r of another particle, and ρ is the average particle number density. The fractal dimension D_f can be determined by determining the slope of double logarithmic plot of $n(r)$:

$$n(r) = n_0 (r/a)^{D_f} \quad (r < \xi). \tag{1.4}$$

An example of determination of D_f from $n(r)$ is shown in Figure 1.3.

1.1.4 Glasses or gels?

Glasses and gels have many properties in common. Their phase transitions are both from ergodic to nonergodic, which means that they are both kinetically defined states rather than thermodynamic in orgin. It is commonly accepted that glass

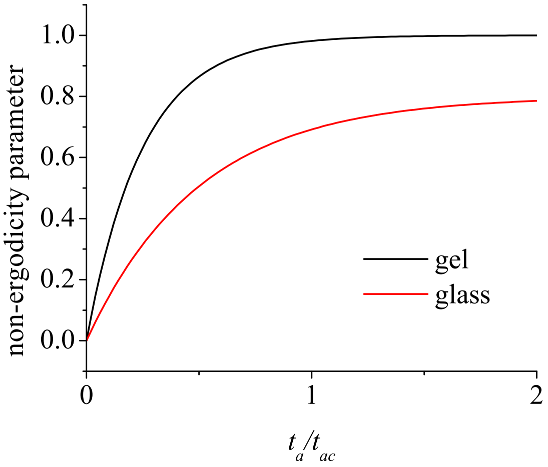

Figure 1.4: Illustration of the evolution of the nonergodicity parameter $f(q, \infty)$ for gel and glass samples. t_a is the time when the particles begin to aggregate; t_{ac} is the critical time. The samples can be divided into two groups according to the evolution of nonergodicity parameters according to Ref. [4].

transition happens at high particle concentration. The motion of the particles in the glass is blocked by the neighboring particles, increasing the viscosity and decreasing the diffusion coefficient. By contrast, gels can form at particle concentration as low as $\phi = 10^{-4}$ to 10^{-2}. Particles typically form gel networks due to strong attractive force. One explanation of the particle aggregation is that the particle moves into the local free energy minimum that they cannot escape [4]. Jabbari-Farouji *et al.* [4] applied the intermediate scattering function $f(q,t)$ to investigate the distinction between glasses and gels. The form of $f(q,t)$ is expressed as:

$$f(q,t) = 1 + (I_t/I_E)[(g_t(q,t) - g_t(q,0))^{1/2} - 1], \tag{1.5}$$

where I_t and I_E are the time-averaged and ensemble-averaged scattered intensity, and $g_t(q,t)$ is the time-averaged intensity correlation function obtained by dynamic light scattering. The system they studied is a suspension of anisotropic and charged

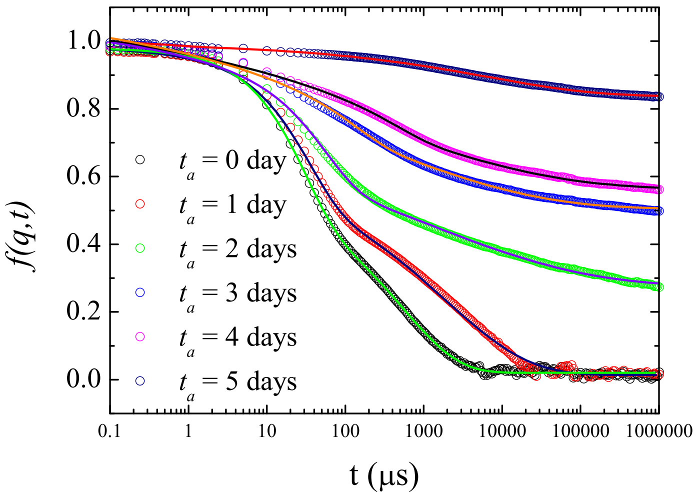

Figure 1.5: Intermediate scattering function for increasing waiting times (from left to right) $t_a = 0$ - 5 days, silica concentration C = 0.37 wt% and particle size 7 nm. The lines are fittings to equation $f(q,t) = f_0 + A_1 \exp[-(t/\tau_1)^\beta + A_2 \exp(-t/\tau_2)$.

Laponite colloidal particles (Synthetic clay). They showed that the nonergodicity parameter $f(q,\infty,t_a)$ (t_a is the waiting time, the time when the particles start to aggregate) for the gel samples falls into a master curve that evolves to 1; for the glass samples, the master curve evolves to 0.8. Illustration of the argument is shown in Figure 1.4. An example of $f(q,t)$ for relatively high silica concentration (0.37 wt%) from our own research work is shown in Figure 1.5. The experimental data was fitted into a model of stretched exponential decay plus an extra exponential decay, $f(q,t) = f_0 + A_1 \exp[-(t/\tau_1)^\beta + A_2 \exp(-t/\tau_2)]$. The different aggregation mechanisms of glass and gel are reflected by the microstructure (e.g. intermediate scattering function $f(q,t)$) and by the mechanical properties (e.g. elasticity).

1.2 Experimental methods to study the gel.

1.2.1 Dynamic light scattering

Dynamic light scattering (DLS), which is also known as Photon Correlation Spectroscopy (PCS), uses scattered light to measure the diffusion rate of the particles and clusters. The diffusion data is usually calculated according to the Stokes equation to derive the hydrodynamic radius of the particles, or the size of the clusters in the aggregating system. A schematic image of the light scattering instrument is shown in Figure 1.6. The sample scattered with the scattering vector denoted $\mathbf{q}$. In the past, many studies were devoted to the investigation of the aggregation and gelation of concentrated systems applying the DLS techniques [25, 8]. Figure 1.7 shows a typical evolution of the time averaged intensity correlation function $g_2(t)$ for colloidal silica suspension with $\phi = 4.7\%$ at various aggregation times. At the gel point (70 – 80 min), where $g_2(t)$ does not decay to 1 and $g_2(t)$ plateau at small t suddenly drops to a lower level, large scale particle motion becomes strongly suppressed and the dynamics becomes nonergodic. Another way of determining the gel point by dynamic light scattering method is by the presence of the typical power-law behaviors of $g_2(t)$ -1 $\propto t^{\mu}$, where μ depends on the particular system [26].

Figure 1.6: Schematic figure of dynamic light scattering instrument.

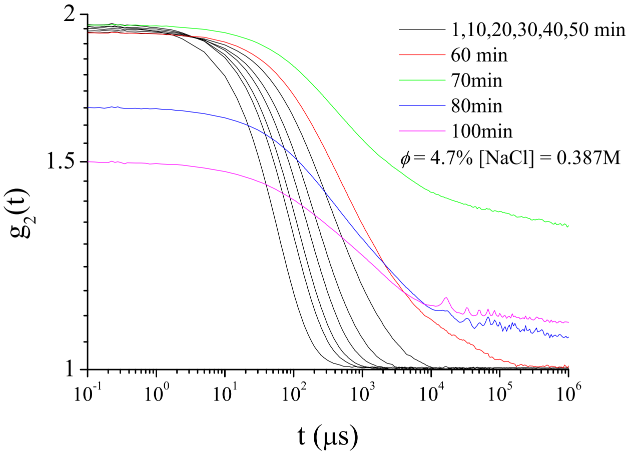

Figure 1.7: Measured intensity correlation functions $g_2(t)$ for silica particle suspension with volume fraction $\phi = 4.7\%$.

1.2.2 Static light scattering

Static light scattering (SLS) is a useful tool to determine the radius of gyration and fractal dimension of aggregates [27]. The fractal dimension can be obtained by the slope of a log-log plot of I vs. q, as shown in Figure 1.8 for an example of colloidal silica suspension of $\phi = 0.1$ % and concentration of salt [NaCl] = 0.51 M. At aggregation time $t = 4$ days, D_f is determined from the slope of linear fitting to the intensity data, $D_f \approx 1.19$. D_f increases gradually to 2.07 at late time ($t = 7$) days when the system forms large clusters. The limitation of this method to determine D_f is that it depends on the selection of data points for linear fitting. This method has been applied for many year to explore the fractal dimension [28, 29, 30, 31, 32, 33, 34]. Schaefer and Martin [28] measured the fractal dimension of small silica particles through the power-law decay of the structure factor $S(q) \sim q^{-D_f}$ by SLS. Aubert and Cannell [29] observed the restructuring of colloidal silica aggregates with $d_f = 1.75$ from rapid aggregation evolving into $d_f = 2.08$, which is normally obtained from slow aggregation. The radius of gyration R_g of a cluster at small particle concentration

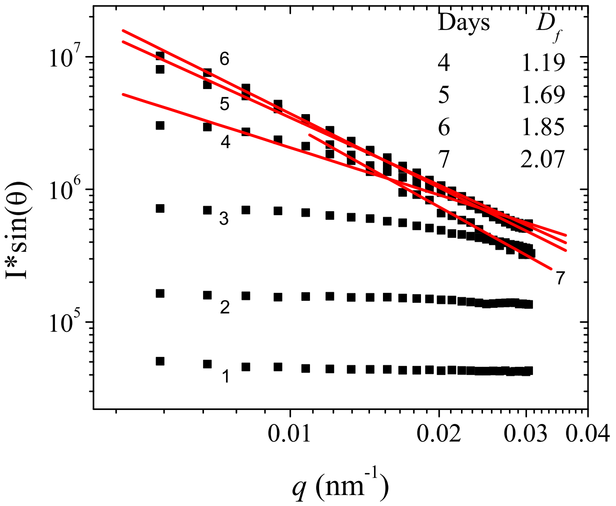

Figure 1.8: An example of plots of the excess light scattering intensity of colloidal silica aggregates versus q for $\phi = 0.1$ % and concentration of salt [NaCl] = 0.51 M.

can be measured by SLS. Carpineti *et al.* [32] studied the growth of R_g of clusters formed by the fast aggregation of polystyrene latex through SLS.

1.2.3 Rheology

In the gelation process, particles aggregate to form large clusters, which then connect with each other to form networks that fill space. The remaining particles and separate clusters will continue to attach to the network to make a stiffer gel. The system experiences a fluid-solid transition, which can be monitored by the change in rheological properties. One method of capturing the sol-gel transition involves the application of oscillatory shear, with the gel criteria [35], given by

$$G'(\omega) \propto G''(\omega) \propto \omega^n, \quad \text{with} \quad 0 < n < 1, \tag{1.6}$$

where $G'(\omega)$ is the storage modulus, $G''(\omega)$ is the loss modulus and ω is the frequency. A schematic illustration of the gel point is indicated in Figure 1.9, where $G'(\omega) > G''(\omega)$ and the two parallels. Richter *et al*. [26] applied this method to study the sol-gel transition of two thermoreversible gelling mixtures, showing $n = 0.59$. Aoki *et al*. investigated the sol-gel transition of carbon black suspension and found $n = 0.71$ - 0.74 [36]. This method requires a relatively slowly evolving systems, as the system should stay in essentially the same condition during the whole frequency exploration during transition. The gel point may also be determined either by the divergence of the viscosity or the onset of shear modulus. These methods cause another problem, as the shear motion of the measurement may cause the breakage of the tenuous network just formed at the critical point.

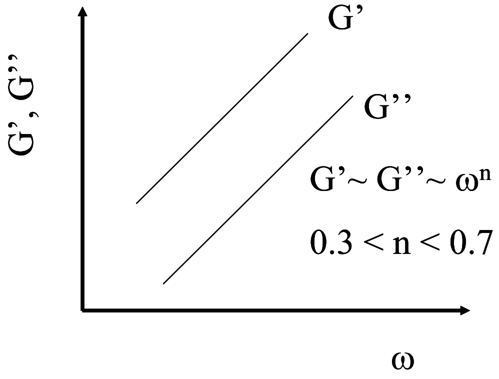

Figure 1.9: Schematic representation of dynamic modulus G' and G'' as function of frequency ω at the gel point according to Ref. [5].

1.2.4 Confocal Microscopy

Confocal microscopy explores the clusters during aggregation by locating individual particles. Compared with dynamic light scattering, one limitation of confocal spectroscopy is that the particles studied should not be too small; several hundred nanometers is the lower limit for measurement. Lu *et al*. applied the confocal method to investigate aggregation of particles of radius $a = 574$ nm, induced by the addition of nonadsorbing polymer(polystyrene, PS) through the depletion force. Some of their confocal images with various ϕ are shown in Figure 1.10. Figure 1.10 (a) and (d) show that no aggregates are found for low polymer concentration, noted by $c_p = 0.34$ (mg PS per ml of solvent); for higher $c_p = 1.31$, large interconnected clusters are observed in Figure 1.10 (c) and (f). At intermediate polymer concentration, large separate clusters surrounded by small aggregates or single particles are present in the system. Dinsmore *et al.* [37] also applied confocal microscopy to determine microscopic structure, connectivity, and elasticity of colloidal gels.

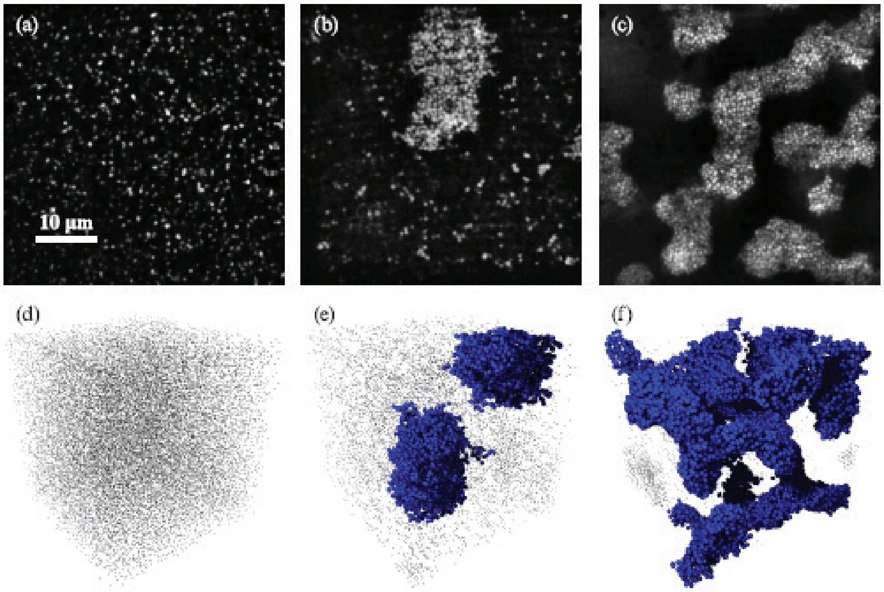

Figure 1.10: (a)-(c) 2D confocal microscope images $(60\mu m)^2$ and (d)-(f) 3D reconstructions $(60\mu m)^2$ of colloid polymer samples with $\phi = 0.15$ and long-polymer depletant. For 3D data, particles in clusters with ≥ 500 particles are shown at actual size; remaining particles are shown at 1/5 actual radius. Ref. [6].

1.3 Simulation and models of the gels.

Simulation is limited in fully describing the complex chemical and physical interactions in real systems. However, it is successful in reproducing many important features of gelling systems. Computer simulation is a very useful tool as it can simultaneously observe the particle aggregation process microscopically and macroscopically, without assumption about the dynamics. The results from simulation calculation are a useful guide to interpret the data of experiments, and provide an opportunity to explore the role of well-defined forces.

1.3.1 Models

The simplest gel network formation model was proposed by Bremer *et al.* [22], that individual clusters grow separately with a constant value of D_f. Those clusters grow gradually until they reach the critical size R_c, after which they connect with each other and form a space-filling network. The illustration of the structure of a colloidal gel at the critical point (the gel point) is shown in Figure 1.11. For a system of colloidal particles of radius a, total volume V and solid volume fraction ϕ_0, the number of primary particles is

$$n_0 = \frac{\phi_0 V}{4\pi a^3/3}. \tag{1.7}$$

According to the fractal theory (1.1), number of particles in a critical cluster is

$$n_c = (R_c/a)^{D_f}. \tag{1.8}$$

The total number of clusters

$$N_c = n_0/n_c. \tag{1.9}$$

At the critical point, the clusters fill the whole volume, i.e.

$$N_c \cdot \frac{4\pi}{3} R_c^3 = V. \tag{1.10}$$

According to (1.7 – 1.10), we can deduce that the critical cluster size is

$$R_c = a\phi^{1/(D_f-3)}. \tag{1.11}$$

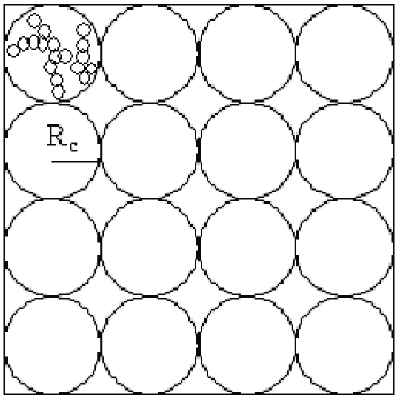

Figure 1.11: Schematic structure of colloidal gel at critical point; the circles indicates fractal clusters of size R_c.

We found that the fractal dimension D_f can be obtained by this model. Figure 1.12(a) shows the growth of cluster size R_h/a as function of scaled time t/t_{gel} for particle volume fraction $\phi_0 = 0.01$, obtained from DLS measurements. The critical cluster size is predicted by the exponential growth of the cluster, $R_c = 78.2\ a$. D_f

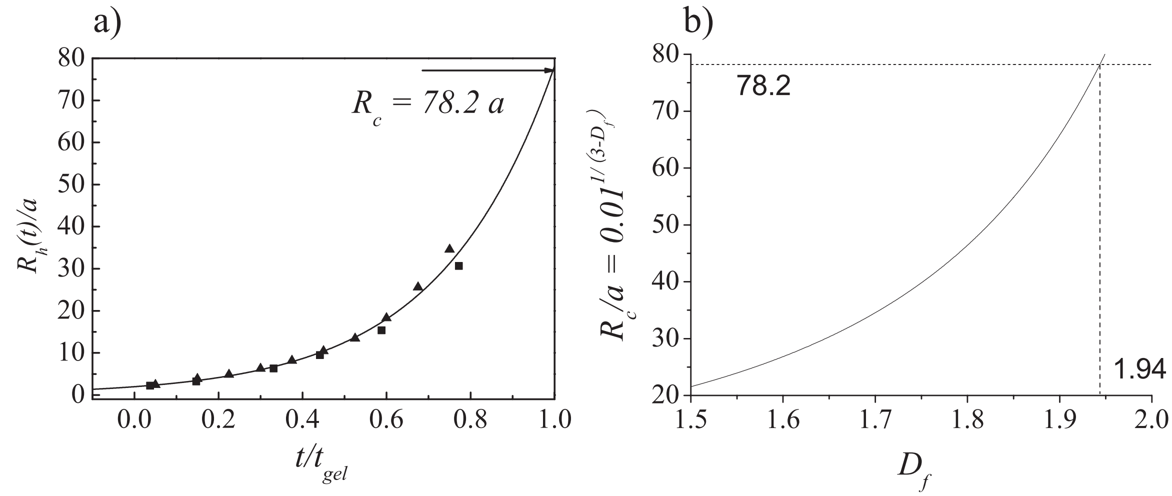

Figure 1.12: a):The growth of cluster size R_h/a as function of scaled time t/t_{gel} for particle volume fraction $\phi_0 = 0.01$ obtained from DLS measurements (details about the experiments are shown in Chapter 2); b): model prediction of fractal dimension D_f.

= 1.94 is determined from (1.11), as indicated in Figure 1.12(b). This model has made a few assumptions, which are not quite true in reality. At the critical point (gel point), it is assumed that all the clusters have the same size. They connect with each other at the same time, the critical time. Aggregation between individual clusters at early times is neglected. In real experiments, clusters formed by DLCA or RLCA have a time-dependent size distribution of cluster size. While large clusters connected to form a space-filling network, small clusters and individual particle still move and gradually attach to the particle network, making contributions to both the structure and the mechanical properties after the gel point.

1.3.2 Fuchs stability ratio

Smoluchowski [38] and Fuchs [39] applied a stability ratio to describe the effectiveness of the potential barrier in preventing particles from aggregating. The definition of W_F is:

$$W_F = \frac{\text{average time for bonding with repulsion}}{\text{average time for bonding without repulsion}} \tag{1.12}$$

The probability of bonding, which is the inverse of W_F, equals J/J_0, where J_0 is the particle flux for dimerisation of a single pair of identical particles; while J is the particle flux for identical particles with a potential force. The form of both J and J_0 were expressed as [3, 39, 38, 40],

$$J_0 = 2aD_c\phi \quad \text{and} \quad J = \frac{D_c\phi}{\int_{2a}^{\infty} \frac{1}{r^2} e^{U(r)/kT} dr}, \tag{1.13}$$

where a is the radius of the primary particle, D_c is diffusion coefficient, ϕ is the particle volume fraction; from that, we can deduce W_F, which equals,

$$W_F = J_0/J = 2a \int_{2a}^{\infty} \frac{1}{r^2} e^{U(r)/kT} dr. \tag{1.14}$$

Mellema *et al.* [3] applied the Fuchs stability ratio W_F to relate the cluster growth and the structure of the cluster with the interpaticle interactions. They investigated the dependence of the fractal dimension D_f on W_F and the particle volume fraction ϕ and found that D_f is slightly dependent on W_F and ϕ for high W_F. The limitation of this approach is that it can only apply to the very early stages of gelation. The Morbidelli group [20] investigated the kinetics of reaction-limited cluster aggregation of fluorinated polymer colloids through by applying experimentally measured W_F in the expression of all the aggregation kernels of the population balance equations [38]. In Chapter 2, we apply W_F as a parameter in the coefficient of the scaled time in a gel kinetic model.

1.3.3 Interparticle Potential

The form of the interparticle potential can have a large effect on the final gel structure. The long-range repulsive interaction favors open structures with cross-linked chains of particles formed at low bonding probabilities, but the attractive force is critical for aggregation. When the attractive force is dominant, it has been observed that dense or loose structure will form, depending on the competition between the cross-linking and the phase separation [7]. Various potential models have been applied in investigations simulating particle aggregation and gelation [41, 42, 43, 7]. In some systems, there is only attractive or repulsive potential, which are idealized systems. In reality, particles interact with both attractive and repulsive forces, generalized by the Lennard-Jones (n-2n) and related potentials $\mathbf{U}(r)/k_BT = A[(\frac{2a}{\mathbf{r}})^{2n} - (\frac{2a}{\mathbf{r}})^{n}]$, with $n = 6$ the classical form of the potential. The interaction force is deduced through $\mathbf{F} = -\nabla U(\mathbf{r})$. Lodge *et al.* [44] applied Brownian Dynamics simulation to investigate the gelation and aging process of colloidal particles interacting via 6:12 Lennard-Jones interaction. They found percolated structures for systems with volume fraction $\phi > 0.07$. Foffi *et al.* [43] also studied low packing volume fraction and indicated that the formation of an arrested state is due to the mobility reduction associated with the glass transition. A Yukawa potential $\mathbf{U}(r)/k_BT = A\exp(-\kappa r)/r$ is sometimes added to represent the long-ranged repulsive force. It has been suggested that the formation of long chain-like structures is related to the repulsive barrier [45, 46, 47]. Other types of potentials describe the formation of reversible or irreversible bonds. Seaton *et al.* and Sánchez *et al.* [48, 49] applied a FENE (finitely extensible nonlinear elastic) potential to simulate the reversible bonding between particles. The spring potential, which was used to describe the bonding between solid atoms in the work of Koplik *et al.* [50], can also be used to simulate the reversible bonding between particles. Whittle *et al*. [7] studied a simple bonding irreversible potential, which is formed between the two nodes created on the surfaces of the two particles by connecting the centers of two particles (indicated in Figure 1.13). Once formed, the bond cannot be broken. The expression of the bonding potential ϕ_B is as follows:

$$\phi_B(b_{ij}) = \varepsilon_b(\frac{b_{ij} - b_1}{b_0}); b_{max} >\mid b_{ij} \mid> b_1, \tag{1.15}$$

$$\phi_B(b_{ij}) = 0; \mid b_{ij} \mid< b_1, \mid b_{ij} \mid> b_{max}, \tag{1.16}$$

where b_{ij} is the distance between the two nodes on particle i and j. The parameters b_0 and b_1 set the range of the potential and ε_b is the bond energy.

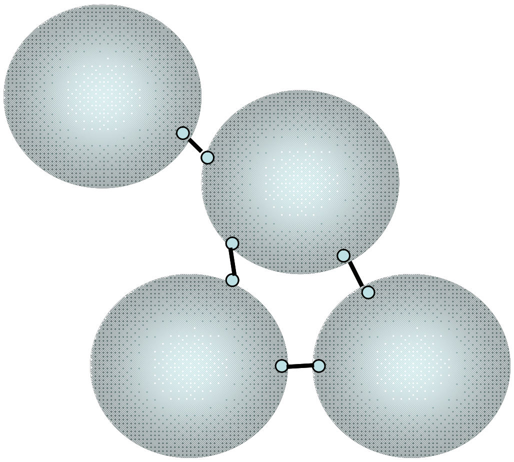

Figure 1.13: Illustration of Bonding assumed in the simulation. Bonds are formed between nodes (small circles) when particles approach to within a critical distance. Once formed, the bonds are permanent and the nodes maintain relative positions on the nominal particle surface ($r = \sigma/2$), sketched according to Ref.[7].

1.3.4 Kinetics

Aggregation from colloidal suspensions is a very important phenomenon in industrial processing. More attention has been taken to understand its main features and model its kinetics. The structure evolution as well as its relationship to the mechanical properties of a system is a useful approach to study the aggregation mechanism. A simple way to describe the kinetics of cluster growth can is by a power law increase of the average radius of gyration as a function of the aggregation time [3, 41]:

$$R_g \propto t^{\alpha}, \tag{1.17}$$

where α is a constant depending on the sticking probability and the particle volume fraction. Generally the exponent is in the range of α = 0.2-0.4. For diffusion-limited growth α equals $1/D_f$ and for reaction-limited growth $R_g \propto e^{\beta}t$, where β is a constant [3, 32, 51]. The aggregation kinetics of cluster growth modelled by the well-established frame work of population balance models were discussed in details in the book of Ramkrishna [52]. Sefcik *et al.* also applied the population balance approach to describe the gel formation kinetics, which has been validated against experimental data obtained from light scattering. They incorporated the concept of fractal theory and the application of Fuchs stability ratio in the description of aggregation kinetics.

1.4 Outline

The thesis has four main chapters and a conclusion chapter. Chapter 2 presents the experimental work for colloidal silica aggregation and gelation. The hydrodynamic radius and the radius of gyration of particle clusters during aggregation are captured by dynamic and static light scattering. The kinetics fall into the reaction-limited cluster aggregation regime, which evolve to fractal objects characterized by the fractal dimension D_f. The rheological properties, e.g viscosity and dynamic modulus, are monitored by the controlled strain rheometer. A gelation mechanism is presented at the end of the chapter which indicates a universal behavior in the gelation process. This model help us to predict particle evolution and optimize properties and structure.

Chapter 3 investigated the role of hydrodynamics and the impact of repulsive barrier of interparticle potentials during particle aggregation in colloidal suspension. Stoksian and Brownian Dynamics techniques were applied to simulate the particle interaction and aggregation. The structure (both local and long-ranged) of particle clusters was investigated in terms of radial distribution function, bonds per particle and static structure factor. The comparison was made between the system with or without many-body hydrodynamic interactions, with a percolation diagram presented to indicate the different percolation lines. Finally, a three-particle investigation reveals the particle evolution with/without hydrodynamic and repulsive interaction.

In Chapter 4, a comprehensive discussion about the interparticle potential with or without restrictions in the rotational and stretching motion of particles was presented in both two-dimensional and three-dimensional systems. Two types of non-restrictive bonding potential (FENE and spring potentials) and one spring-type potential with restriction in the rotational motion are discussed in the chapter. Chapter 5 shows the numerical results of rheological properties during particle aggregation. The stress relaxation function as well as the dynamic moduli at various time was presented. Finally, a conclusion was made at Chapter 6.

Chapter 2

Structural and Rheological Evolution of Silica Nanoparticle Gels

2.1 Introduction

This chapter describes a study of colloidal gelation base on rheological and light scattering experiments. Movitivation for the work is found in the fact that colloidal gels are found in a wide variety of applications such as processing of ceramics, coatings, inks, personal care products, and minerals [53, 8]. Understanding the relationship between particle interactions, the resulting gel structure and rheology is important where a particular texture or structure of gel is needed. We investigate the microstructural changes during the gelation process, and their influence on the rheological properties of the system.

The problem of gelation has been studied for a number of years. Many studies have been devoted to polymer and thermal gels to probe the characteristic gel behavior and mechanical properties of these systems [54, 55, 56, 57, 58]. While many studies have been devoted also to colloidal gels forming fractal structures, parameters controlling

---

This chapter is published as *Structural and Rheological Evolution of Silica Nanoparticle Gels*, X. J. Cao, H. Z. Cummins and J. F. Morris, Soft matter. **6**, 5425-5433 (2010) the behavior of the transition, the onset and nature of the stress-bearing properties of the solid-like phase, remain poorly understood. In this work, we have considered the dynamics of gelation in a colloidal silica dispersion with primary particles of $O(10)$ nm diameter. We provide a very comprehensive study of gelation dynamics and the material properties, considering both the approach to gelation and the property evolution after gelation. Gelation is induced by adding salt to the suspending liquid, leading to screening of the silica surface charge providing a stabilizing barrier against aggregation.

The primary contributions of this work to the rather sizable literature on related systems are the determination of the gelation times by two methods, as we apply both light scattering and rheometry, for the same system over a wide range of parameters. We demonstrate that for dilute ($\leq$ 4% solids by volume) dispersions, the gelation process induced by addition of salt can be scaled to master curves both before and after the gelation point using the measured gel time. The properties when presented as functions of dimensionless time are then independent of the actual rate of aggregation over orders of magnitude in this rate (or, alternatively considered, over orders of magnitude in the gel time); the properties both before the gel time (cluster size, for example) and after gelation (elastic modulus) are then functions of the particle fraction and dimensionless time only. A similar collapse, of the post-gelation properties only, was described [59] for gelation of a surfactant-stabilized polymer latex at somewhat higher solids fractions of $\phi = 5 - 9\%$; in the referenced work, the scaling of time used microscopic information only and some discussion of insight resulting from a consideration of the relation between the scalings of time in our work and the Sefcik *et al.* [59] study is given following the presentation of our results. A practical contribution arising from this scaling is that it allows prediction of properties for conditions outside the range studied in detail.

As suggested by the comments on the contributions of this work just above, the characteristics of the colloidal suspensions can be controlled by the particle size, adjusting interparticle forces (for example, by addition of electrolyte), and the volume fraction of the dispersed phase. In an aqueous colloidal silica suspension, there is negative charge on the surface of the particles at high pH. The resulting electrostatic repulsion stabilizes the dispersion against flocculation. The ionic strength of the solution and pH control the strength of the repulsion. Addition of ions decreases both the range and the magnitude of electrostatic repulsion by reducing the Debye screening length and the zeta-potential. This screening effect of added salt leads to destabilization of the kinetically stable system and hence to aggregation and gelation [60]. Change in pH alters the surface charge of silica particles, and thus destabilizes the colloidal suspension. In this chapter, we focus on the effect of salt concentration and the change in solid volume fraction.

There are two limiting cases of fluid to solid transition which have been studied recently [61, 62]. The first is for high volume fraction hard sphere particles, forming a colloidal glass characterized by trapping of particles within cages formed by nearest neighbors. The caging of the hard sphere particles leads to a colloidal glass at volume fraction $\phi_g \approx 0.58$. The colloidal hard sphere glass transition has been successfully studied by mode coupling theory (MCT) [63, 64, 65, 66]. The second limiting case is for systems with low volume fraction but strongly attractive particles. Fractal clusters are formed due to the strong interparticle interactions, finally leading to a continuous but tenuous space-filling network of colloidal gel. We study this system.

At low ϕ, a scaling theory which relates the elastic properties of a gel to its network structure was developed by considering the structure of the gel network as a collection of flocs [67, 28, 31, 29]. The structure of the colloidal clusters formed during the aggregation process can be described by fractal behavior, which is a simple description of the cluster geometry. It relates the mass of the cluster to its characteristic size with a single parameter, the fractal dimension D_f, which depends on the aggregation process. The fractal dimension of an object of mass N and radius r is defined by the relation[67] $N \propto r^{D_f}$. Shih *et al.* (1989) found the fractal dimension of colloidal alumina gels for dilute suspensions $D_f \cong 1.95$ and $D_f \cong 2.04$ from rheological measurements and static light scattering respectively[12]. Similarly, Lin *et al.* (1990) studied the aggregation of three different colloids (gold, silica, and polystyrene) and found the identical fractal dimension $D_f = 2.1 \pm 0.05$ for all cases[68]. Later, Rueb & Zukoski (1997) studied the shear-densification effect of concentrated colloidal gels and found $D_f = 2.5$ with preshear compared with $D_f = 1.4$ without shear[69]. In addition, they demonstrated that the elastic modulus G' and the maximum strain γ_M in linear viscoelastic limit both scale as $\phi/\phi_G - 1$, where ϕ_G is the gel volume fraction. Hanley *et al.* (1999) investigated the gelation of a colloidal silica system under a constant shear rate and concluded that a drop in viscosity corresponds to a structural densification[70]. Krall & Weitz (1997) used dynamic light scattering to measure the internal dynamics of weak fractal colloidal gels, and developed a model to determine elastic modulus which scales as $G' \sim \phi_0^{3.9}$, where ϕ_0 is the solid volume fraction[71]. Zackrisson *et al.* (2006) studied the effect of particle concentration and ionic strength on the irreversible colloidal silica gelation and suggested separate types of microstructure for *in situ* generation of salt and direct addition of salt solutions[8]. They determined the gel boundary by a prominent increase of the optical density and incipient non-ergodicity.

In this chapter we present the results of a study of the aggregation kinetics of silica colloidal particles in aqueous solutions. This chapter is organized in three parts. We first introduce dynamic and static light scattering and rheological methods, their basic theory and experimental set up in Part 2. Then, we discuss in Part 3 the results of dynamic and static light scattering and rheological tests performed on identically prepared samples. A short conclusion and discussion of our work follows.

2.2 Experimental methods

We used the aqueous colloidal silica suspension *LudoxSM*, pH = 10.47 (Sigma-Aldrich), consisting of amorphous silica particles with radius 7.0 nm, as reported by the manufacturer and confirmed by light scattering on diluted samples, and with 30 mass% SiO_2 (corresponding to a volume fraction $\phi = 16.0\%$). Aggregation is initiated by the addition of aqueous NaCl (Fisher) at varying molarity under stirring. The resulting mixture was filtered across a 0.8 μm Millipore filter for light scattering, to remove dust contamination. We will briefly outline the methods and the formulae applied in the interpretation of experiments.

2.2.1 Dynamic light scattering (DLS)

Light scattering is a method to probe the structure and dynamics of the colloidal suspension. We use it here also to determine the gelation boundary. Dynamic light scattering, which probes the size of dispersed matter, and therefore the aggregation kinetics, measures the time-averaged time correlation function of the intensity $I(\mathbf{q},\tau)$ of light scattered by the sample in the direction described by the scattering vector $\mathbf{q}$, $|q| = (4\pi n/\lambda) sin(\theta/2)$; here the refractive index of the solvent $n = 1.33$, wavelength $\lambda = 488\ nm$, and the scattering angle $\theta = 90°$. For simplicity, we will write $I(\tau)$ instead of $I(\mathbf{q},\tau)$ since $|q|$ is constant for all DLS experiments.

The normalized intensity correlation function is $g_2(\tau)$, described as

$$g_2(\tau) =< I(\tau_\circ) I(\tau_\circ + \tau) > / < I(\tau) >^2 . \tag{2.1}$$

For an ergodic system, the Siegert relation for the ergodic system is

$$g_2(\tau) = 1 + |g_1(\tau)|^2, \tag{2.2}$$

where $g_1(\tau)$ is the normalized autocorrelation function of the scattered electric field; $\mid g_1(\tau) \mid$ is also equal to the normalized intermediate dynamic structure factor of the sample, $S(q,\tau)/S(q,0)$, where $S(q) = \frac{1}{N}\langle \sum_i \sum_j e^{i\mathbf{k}(\mathbf{r}_i - \mathbf{r}_j)} \rangle$ with position vector of particles denoted $\mathbf{r}_i$ and $\mathbf{r}_j$. In practice, the amplitude of the second term of (2.2) will be slightly reduced by the detection optics, so that

$$g_2(\tau) = 1 + a|g_1(\tau)|^2, \tag{2.3}$$

with $a \leq 1$. For a dilute suspension of spheres of hydrodynamic radius R_h,

$$|g_1(\tau)| = \exp[-Dq^2\tau], \tag{2.4}$$

where D is the translational diffusion constant given by the Stokes - Einstein relation $D = kT/6\pi\eta R_h$. Here, η is the viscosity of the solvent. Equation (2.4) can also be written as

$$|g_1(\tau)| = \exp[-\Gamma\tau] = \exp[-\tau/\tau_m], \tag{2.5}$$

where $\Gamma = 1/\tau_m = Dq^2$, τ_m is the relaxation time. Then, the normalized intensity correlation data for a dilute monodisperse colloidal dispersion can be fit directly to $g_2(\tau) = 1 + ae^{-2(\tau/\tau_m)}$ and the radius of the colloidal particles is determined by $1/\tau = Dq^2$, with $D \sim 1/R_h$. For a polydisperse system, the stretched exponential function $\exp[-2(\tau/\tau_m)^\beta]$ was used to obtain

$$|g_2(\tau)| = 1 + a\exp[-2(\tau/\tau_m)^\beta], \tag{2.6}$$

which can be used to fit the intensity correlation function data in order to obtain the average hydrodynamic radius R_h.

Matsunaga & Shibayama (2007) proposed several methods to determine the gel point by dynamic light scattering; one of them is "a depression of the initial amplitude of intensity correlation function (ICF)" [72]. We will apply this criterion to determine the gel point when the $g_2(\tau \to 0)$ plateau drops suddenly from the value of $g_2 \approx 2$.

2.2.2 Static light scattering (SLS)

Static light scattering has been widely used in the study of the fractal behavior of clusters. Our SLS experiments were carried out in a BIC BI-200SM computer-controlled goniometer fitted with toluene bath. The light source is a Coherent DPSS532 532 nm diode laser. The intensity of the laser was adjusted with a variable neutral density filter to keep the intensity at the smallest scattering angle (15°) below 2 $\times 10^6$ counts per second (Mcps). Data was collected at 5° intervals from 15° to 150°. At each angle data was collected during three repeats of 10 seconds each. The intensity data was collected and converted to $I(q)$ for q values between 0.004 and 0.03 nm^{-1}. This experiment was designed to determine the fractal dimension as well as the radius of gyration of growing silica clusters after the addition of salt to dilute silica suspensions.

If the clusters are sufficiently large, D_f can be determined directly from the angular dependence of the light-scattering intensity through a log-log plot of the static light scattering intensity $I_{ex} = Isin(\theta)$ vs q, which is expected to be a straight line whose slope is $-D_f$. The angle dependence of intensity can be fitted by the Fisher-Burford approximant [73],

$$I(q) = I(0)[1 + (2/3D_f)(qR_g)^2]^{-D_f/2}, \tag{2.7}$$

where R_g is radius of gyration. This form has the correct limiting values:

$$(qR_g) \ll 1 : I(q) = I(0)[1 - 1/3(qR_g)^2], \tag{2.8}$$

$$(qR_g) \gg 1 : I(q) = I(0)(qR_g)^{-D_f}. \tag{2.9}$$

2.2.3 Rheometry

Transitions of colloidal silica suspensions from liquid to gel were also monitored by rheological measurements in the linear viscoelastic regime by a strain controlled rheometer (ARES). In order to investigate the gelation transition rheologically, we continuously measured after the initiation of the aggregation with Couette geometry (cup diameter: 34 mm, bob diameter: 32 mm, bob length: 33.3 mm) in oscillatory shear flow at constant frequency $\omega = 1Hz$ and fixed strain 0.01. All rheological measurements were conducted at a fixed temperature of 25°C. In order to investigate the viscosity of the aggregating sample, we conducted steady shear rate measurements with low shear rate $\dot{\gamma} = 0.01s^{-1}$ in the same Couette geometry at temperature 25°C.

A classical definition of gel point (GP)[74] is when the steady-shear viscosity diverges to infinity, and the equilibrium modulus starts to rise, i.e. $\eta_0 \rightarrow \infty, G_\infty =$

0. However, since they involve limiting properties, GP can only be determined by extrapolation from this definition.

Another method to probe the gel transition is performed by a dynamic rheological test. The storage modulus G' and loss modulus G'' obtained from the test have the same power law dependence on strain frequency at the gel point [69, 5],

$$G'(\omega) \sim G''(\omega) \sim \omega^m. \tag{2.10}$$

This is the Winter & Chambon (1987) criterion for gelation[75]. Here, the determination of the gel point comes from the crossover of storage and loss modulus (G' and G'') after which G' increases more quickly than G'' consistent with Drabarek *et al.* (2002)[76] and Matsunaga & Shibayama (2007)[72]. It is confirmed in these studies that the crossover time is approximately equal to the gel time. Rheological determination of the gelation boundary thus rests on our ability to measure the onset of an elastic modulus; this can be quite difficult if the elastic modulus is very low, as is the case for the very tenuous solid networks. The minimum torque we can evaluate in the rheometer is approximately $1.9 \times 10^{-6}\ Nm$ with a minimum value of $G' \approx 3.6Pa$.

2.3 Results

Without salt addition, the colloidal silica suspension is stable. Repulsive forces due to the surface charge maintain particles in a non-aggregating state. Salt addition destabilizes the system by screening the Coulomb repulsion and brings the onset of aggregation and later gelation. The kinetics and mechanical properties of the gel at any time following the salt addition depend on both the salt concentration and particle volume fraction; kinetics and mechanical properties are monitored by light scattering and rheometry.

2.3.1 Dynamic light scattering

Fig. 2.1 shows typical intensity correlation data, $g_2(\tau)$ from DLS after the addition of the salt solution ($\phi = 2\%$, [NaCl] $= 0.454\ M$). Data was collected at time intervals of 15 min. Note that $g_2(\tau)$ decays at all relaxation times τ_m below the gel time t_{gel}, determined by the sudden decrease of the $g_2(\tau \rightarrow 0)$ plateau (indicated by the arrow in the figure). In addition, the relaxation times gradually increase during the gelation process; and the measured relaxation times appear to diverge as the time goes beyond about 80 min, as shown in Fig. 2.2. The drop of the plateau of $g_2(\tau)$ to a much lower level indicates a reduced mobility due to long-ranged network formation. Another consequence from a rheological perspective is that the system starts to have a finite shear modulus or rigidity. Particles can move by Brownian motion, but those which are physically bonded into the network cannot move far. If they do not move at all then their correlation function is time independent and finite, which contributes to the static part of the correlation function. If they move slightly then the ensemble-averaged correlation function decays to a nonzero value at long times [54].

The average hydrodynamic radius of the clusters is calculated through the intensity correlation function fitted as $g_2(\tau) = b + a \exp[-2(\tau/\tau_m)^{\beta}]$ and $< R_h >= \tau_m \frac{k_B T}{6\pi} \cdot \frac{1}{\eta}$; a, b, τ_m,and β are determined by fitting the experimental data using a least-squares algorithm. The viscosity of water is used, which is correct for dilute ϕ in the early aggregation as confirmed by viscosity measurement (Ubbelohde viscometer). The system shows an exponential decay at the early stage of the aggregation process, with β equal to 1; approaching the gel point, the correlation functions progressively deviate from the exponential decay, with a continuous decrease in β, which is an

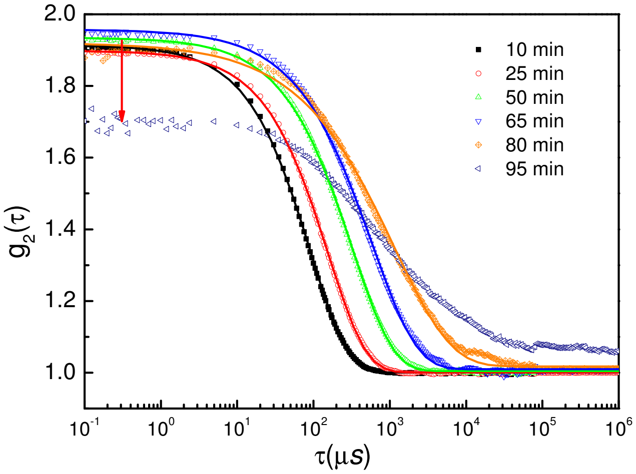

Figure 2.1: Intensity correlation functions $g_2(\tau)$ during the gelation process ($\phi = 2$ %, [NaCl] $= 0.454$ M; dot: original data; line: fitting to $g_2(\tau) = b + a\exp[-2(\tau/\tau_m)^\beta]$).

indication of polydispersity. The size of the clusters increases rapidly with the time as shown in Fig. 2.3. Approaching the gel point, the average cluster size appears to diverges (though it does not) as the system forms a space-filling network. For all three cases, the initial aggregation rate is relatively slow and the rate increases as the size of the cluster increases, as large clusters have more possibilities to connect to particles and clusters [68]. Upon such observation, we present a simple aggregation kinetics model that the aggregation rate dN/dt is proportional to $R(t)^\alpha$, where N is average number of particles in an aggregate, and $R(t)$ is the linear size of the aggregate. As mentioned in the introduction, $N \propto R^{D_f}$, so that this simple model can be expressed as

$$dN/dt = k_r R(t)^\alpha = k_r N^{\alpha/D_f}, \tag{2.11}$$

where k_r is the rate of aggregation with units of min^{-1} for the systems we studied.

For reaction-limited aggregation system (RLA), we treat α/D_f as unity; then $N = N_0\exp(k_r t)$ and $R(t) = R_0\exp(k_r t/D_f)$. In Fig. 2.3, we show the average radius of clusters as a function of time for different salt and solid systems. The solid curves represent fittings to the exponential growth of aggregates (RLA). The aggregation constant depends on both the salt and silica concentration. The coefficient R_0 and k_r are treated as adjustable parameters in the fit; while D_f is kept as a constant 2, an average number of fractal dimension as indicated by the static light scattering results in Table 2.2. The fitting parameters are shown in Table 2.1. R_0 is the size of initial cluster at $t = 0$ immediately after the salt addition. For the same silica volume fraction, the rate of aggregation (k_r) is much faster for samples with high salt concentration and leads to more rapid gelation, in agreement with the rheological evaluation, discussed in § 3.4.

Table 2.1: Parameters of aggregation kinetics ($R(t) = R_0\exp(k_r t/D_f)$) for volume fraction 1% - 4% at different salt concentrations.

ϕ	[NaCl]/M	R_0/nm	k_r
1 %	0.454	14.8 +/- 2.70	0.018 +/- 0.0001
1 %	0.497	12.7 +/- 0.71	0.039 +/- 0.0004
1 %	0.548	17.0 +/- 1.24	0.067 +/- 0.0018
2 %	0.398	12.1 +/- 0.91	0.030 +/- 0.0005
2 %	0.454	14.8 +/- 2.70	0.078 +/- 0.0030
4 %	0.348	6.8 +/- 1.52	0.048 +/- 0.0014

When the aggregation time t is scaled by the measured gel time t_{gel} and $R_h(t)$ is scaled by the particle radius estimated as $R_h(0)$, the normalized average hydrodynamic radius of clusters, $R_h(t)/R_h(0)$, collapses into a master curve and shows an exponential growth as a function of t/t_{gel} for the same silica volume fraction (Fig. 2.4). Hence, as a function of t/t_{gel}, the growth of cluster size is independent of the salt concentration and depends on the silica volume fraction only.

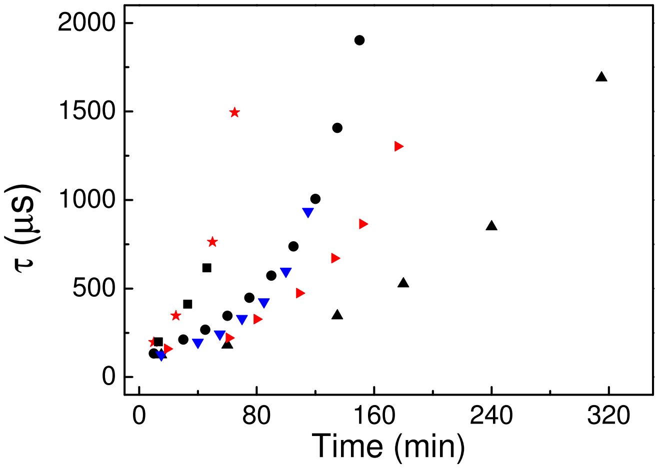

Figure 2.2: Relaxation time τ during gelation process. ■, ϕ = 1.0 %, [NaCl] = 0.548 M; ●, ϕ = 1.0 %, [NaCl] = 0.497 M; ▲, ϕ = 1.0 %, [NaCl] = 0.454 M. Red ★, ϕ = 2.0 %, [NaCl] = 0.454 M; Red ▶, ϕ = 2.0 %, [NaCl] = 0.398 M; Blue ▼, ϕ = 4.0 %, [NaCl] = 0.348 M.

2.3.2 Static light scattering

Table 2.2: The fractal dimension D_f and radius of gyration R_g during gelation process obtained by Fisher-Burford method compared with hydrodynamic radius R_h (ϕ = 1%, [NaCl] = 0.454 M).

Time/min	D_f	R_g/nm	R_h/nm
140	2.10 +/- 0.05	45.0 +/- 0.11	44
185	2.02 +/- 0.07	68.8 +/- 0.14	67
245	2.00 +/- 0.05	85.0 +/- 0.84	108
320	2.04 +/- 0.01	94.0 +/- 0.14	215

The structure of the aggregates was investigated by the application of static light scattering. Fig. 2.5 shows the evolution of the scattered light intensity as a function of the scattering vector q at low volume fraction ϕ = 0.1%. At early aggregation time (0 - 23 min), the intensity is low and is independent of the scattering angle. As the clusters grow larger, the intensity increases and shows variation with angle. The intensity gradually grows and shows significant angular dependence until it

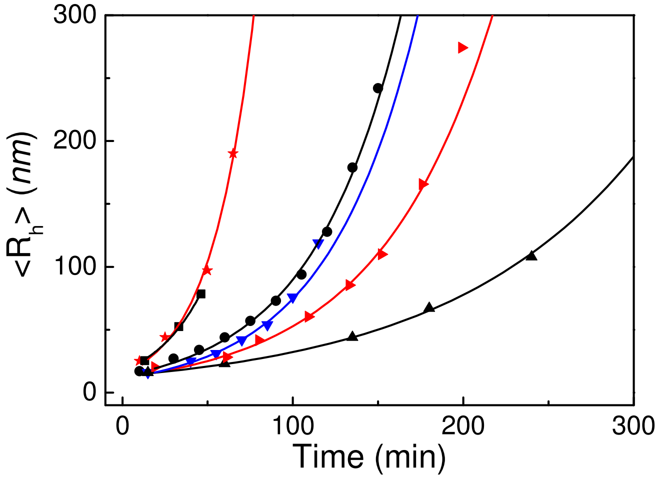

Figure 2.3: The growth of average hydrodynamic radius of clusters for samples ■, $\phi = 1.0$ %, [NaCl] $= 0.548$ M; ●, $\phi = 1.0$ %, [NaCl] $= 0.497$ M; ▲, $\phi = 1.0$ %, [NaCl] $= 0.454$ M. Red ★, $\phi = 2.0$ %, [NaCl] $= 0.454$ M; Red ►, $\phi = 2.0$ %, [NaCl] $= 0.398$ M; Blue ▼, $\phi = 4.0$ %, [NaCl] $= 0.348$ M; solid curves are exponential fittings to $R(t) = R_0 \exp(k_r t/D_f)$.

approximates a straight line in $\ln(I sin\theta)$ vs $\ln q$, shown in Fig. 2.5. The amplitude of intensity changes very little when very large clusters form. A better observation can be found in Fig. 2.6 for times longer than 117 hours. We obtain the fractal dimension D_f and the radius of gyration R_g by fitting the intensity data by the Fisher-Burford method for both $\phi = 1$ % and $\phi = 0.1$ % , as shown in Table 2.2 and Fig. 2.6, respectively. For systems with volume fraction $\phi = 1$ %, they form physically visible gels, which means the systems will not flow after being upside-down. We did not observe physically visible gels for systems with $\phi \leq 0.75$ %. As mentioned by Lin *et. al* [68], the critical volume fraction ϕ_0 to complete gelation is $\phi_0 \approx 10^{-5}$. The radius of gyration (R_g) is defined by the expression given below,

$$R_g^2 = \frac{\sum m_i r_i^2}{m_i r_i}, \tag{2.12}$$

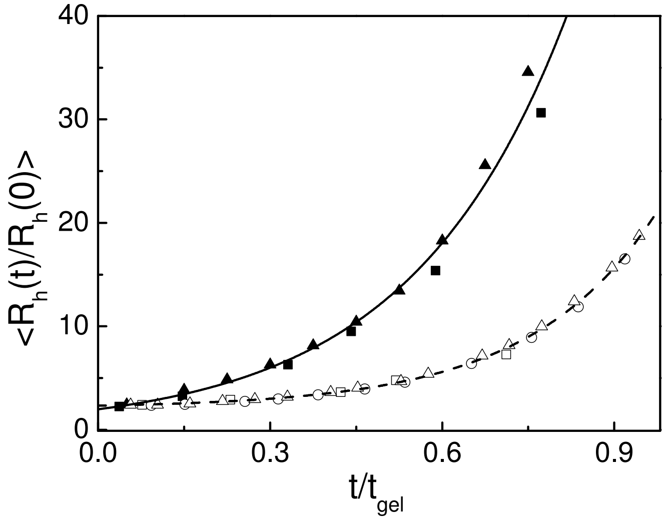

Figure 2.4: The scaled average hydrodynamic radius of clusters. ■, ϕ = 1.0 %, [NaCl] = 0.497 M; ▲, ϕ = 1.0 %, [NaCl] = 0.454 M; yellow ▲, ϕ = 4.0 %, [NaCl] = 0.348 M; □, ϕ = 5.0 %, [NaCl] = 0.38 M; ○, ϕ = 5.0 %, [NaCl] = 0.37 M; △ = 5.0 %, [NaCl] = 0.35 M (Lines are exponential fittings).

where m_i is the mass of the i^{th} particle in the cluster and r_i is the distance from the center of mass to the i^{th} particle. The hydrodynamic radius, as introduced in § 2.1, is calculated from the diffusional properties of the particle cluster and is indicative of the apparent size of the dynamic hydrated/solvated cluster. The comparison of R_g and R_h in Table 2.2 shows that they agree with each other at earlier time; approaching to the gel point, the size of the hydrodynamic radius is larger than the radius of gyration, which indicates that the system starts to form fractal objects. The fractal dimension from the Fisher-Burford method is slightly higher than that obtained from the linear fitting method, as indicated in Fig. 2.7. However, the results from the latter method also depend on the selection of the data points for linear fitting (Fig. 2.6).

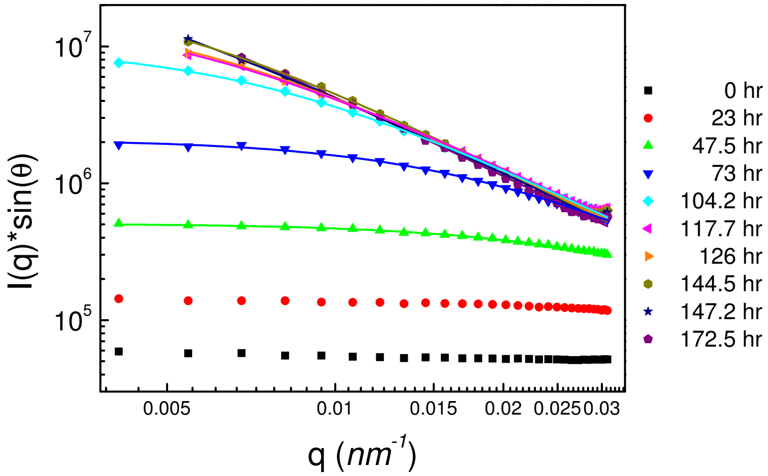

Figure 2.5: The angular dependence of intensity during the gelation process $\phi = 0.1\%$, [NaCl] $= 0.51$ M (Dots are experimental results; Lines are Fisher-Burford fittings;).

2.3.3 Rheological results

Transition of aqueous silica suspensions from liquid-like to solid-like state was examined by rheological methods. We determine the dependence of the linear viscoelastic properties as a function of time for systems of various particle volume fractions and salt concentrations. The linear visco-elastic regime is determined by strain sweep measurement, in which an increasing strain is applied to the formed gel. A maximum strain γ_m was obtained by the response of the storage and loss modulus (G' and G'') to the applied strain. For the gels we studied here, γ_m is between 10% - 15 %, determined by the point where G' and G'' starts to have 10% deviation from the plateau level of G' and G'' of small strains.

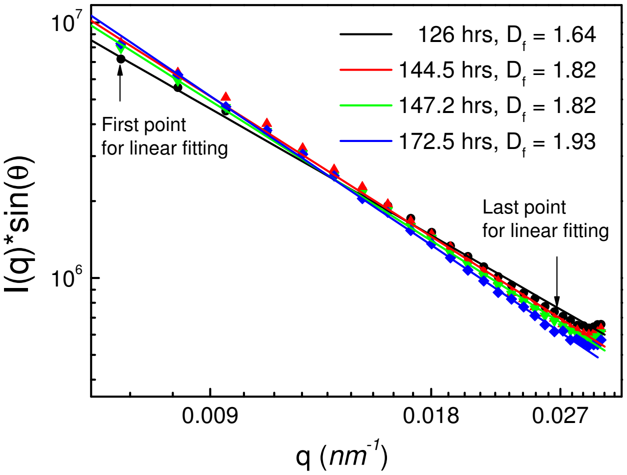

Figure 2.6: Determination of the fractal dimension during the gelation process $\phi = 0.1\%$, [NaCl] $= 0.51$ M (Dots are experimental results; Lines are linear fittings;).

Gel times

In Fig. 2.8, the gel time determined rheologically is shown as a function of salt concentration for several volume fractions (ϕ = 1% - 4.7 %). As we decrease the concentration of the salt, the gel time increases rapidly and tends to diverge at low salt concentration, consistent with stability (i.e. $t_{gel} \rightarrow \infty$) of the as-received (no added salt) dispersion. Larger salt concentration induces a shorter time to GP, due to the stronger screening effect. The effect of silica concentration on the aggregation kinetics can also be observed in this figure. Samples with relatively low silica volume fraction evolve slowly and take more time to form space-filling gel networks, indicated by the arrow in Fig. 2.8 at salt concentration 0.348 M. The gel time can be fitted into equation $t_{gel} = Aexp(-\kappa[NaCl])$, with $\kappa = 8.3 \pm 1.2$ for ϕ = 1% - 4.7 %, and showing no clear trend of variation.

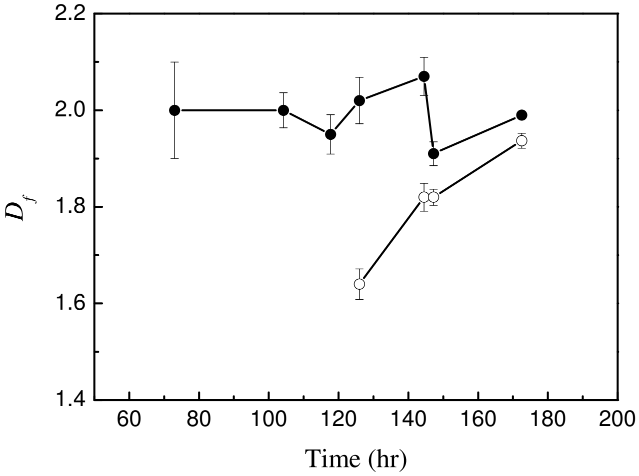

Figure 2.7: The fractal dimension D_f during the gelation process ($\phi = 0.1\%$, [NaCl] = 0.51 M). •, obtained by Fisher-Burford Fitting; ○, calculated by linear fitting.

Effect of salt concentration on kinetics and gel structure

Keeping the volume fraction of silica particles fixed at 1 %, storage (G') and loss (G'') modulus were measured as a function of time following salt addition at different molarities at fixed frequency 1.0 Hz and constant strain 0.01. The results are shown in Fig. 2.9.

For all samples, G' and G'' increase with time after the network formation during the gelation process. The addition of salt solution leads to compression of the electrical double layer around each particle, and eventually to particle aggregation; the connected particles form large aggregates and finally a connected network fills the whole volume, leading to arrest. Phenomenologically, the system exhibits a "gel state". At the same time, G' and G'' become measurable in a rheological test. We determine the crossover time (when G' becomes larger than G'') as the gel time (t_{gel}, indicated by the dashed lines in Fig. 2.9). After the GP, dynamics are largely due

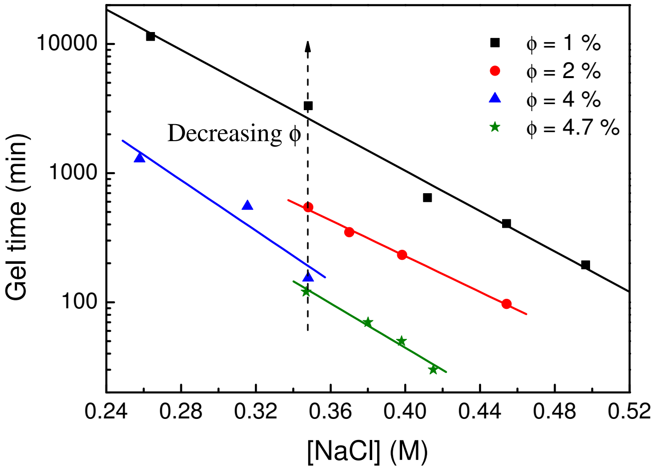

Figure 2.8: Gel time determined rheologically as a function of salt concentration for several volume fractions (ϕ = 1% - 4.7 %); lines are given by data fitting to equation $t_{gel} = Aexp(-\kappa[NaCl])$, with $\kappa = 7.8, 6.9, 9.7, 8.6$ for ϕ = 1, 2, 4, 4.7 %. The arrow in the figure indicates the growth in gel time as function of ϕ for the same salt concentration [NaCl] = 0.348 M.

to the unconnected particles and loose particle clusters among the network, which continue to make contributions to the stiffness of the system as they attach to the space-filling network (increasing G'). Growth in G' and G'' becomes progressively slower.

It is shown in Fig. 2.9 that, for fixed ϕ, the salt concentration affects the time at which the system forms a space-filling network. The suspension with highest salt concentration ([NaCl] = 0.497 M) gels at the earliest time (t_{gel} = 195 min). When the aggregation time is scaled by the gel time, G' collapses into a single master curve for the same silica volume fraction but with various salt concentrations, as shown in Fig. 2.10. This result indicates that during the gelation process, the three samples of the same ϕ and different [NaCl] have similar mechanical strength at the scaled time, which can be further extended to argue that the gel under the same silica volume

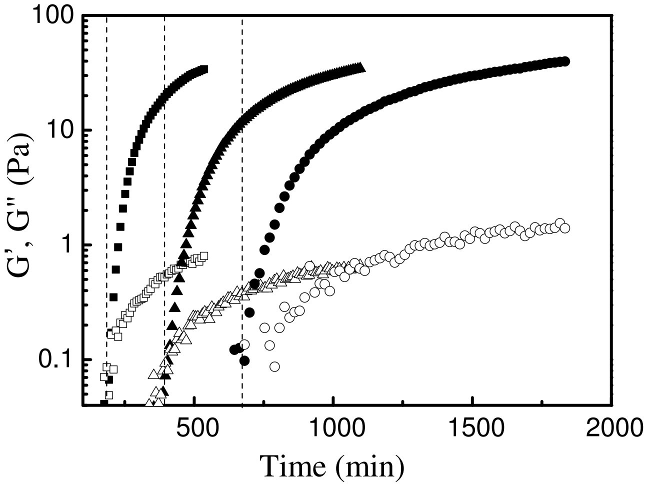

Figure 2.9: The evolution of storage (G', solid) and loss modulus (G'', open) of samples with low silica volume fraction ($\phi = 1\%$). ■,□ ([NaCl] = 0.497 M, $t_{gel} = 195$ min); ▲,△ ([NaCl] = 0.454 M, $t_{gel} = 407$ min); ●, ○ ([NaCl] = 0.412 M, $t_{gel} = 645$ min). Frequency, 1 Hz; Strain, 1 %. The dash lines indicate the gel time.

fraction has similar structure at this scaled time, t/t_{gel}. When combined with the results in DLS (as shown in Fig. 2.11), both the hydrodynamic radius R_h and storage modulus G' can be scaled by the gel time t_{gel} and collapse into two separate master curves. From the scaling behavior of different systems, we suggest there is a universal behavior in aggregation kinetics which can be related to the gel time. For the RLA process leading to the gels studied here, salt concentration only affects the aggregation rate but not the microstructure. The parameter that determines the microstructure and the strength of gel network is the silica volume fraction ϕ.

The inset of Fig. 2.12 shows the viscosity change during the gelation process under weak shearing of $\dot{\gamma} = 0.01$ s^{-1}. Upon mixing, the viscosity of the system is low and close to the viscosity of the solvent (water). Approaching the critical time, the viscosity increases until it reaches a peak value; and then it decreases rapidly. As predicted by Jansen *et al.* (1986) the suspension gels after this point, the gel

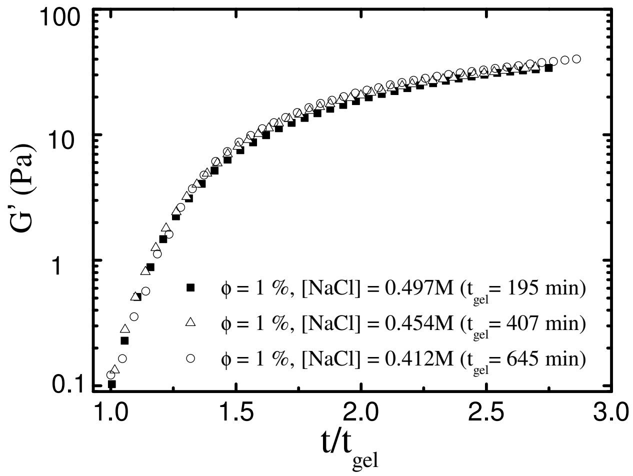

Figure 2.10: The scaling behavior of the storage modulus G' for samples with same silica volume fraction $\phi = 1.0\%$ but various salt concentrations when time is scaled by gel time t_{gel}.

time[77]. The rapid increase in viscosity is due to the formation of large clusters and newly-formed particle network; and the decrease in viscosity is due to the break-up of the newly-formed weak network, which then does not reform under the flow. When the time is scaled by t/t_{gel}, the viscosity also collapses into a master curve (Fig. 2.12). This scaling behavior is consistent with the one found in the growth of hydrodynamics radius and storage modulus of gel network. We note that there is some difference in the peak viscosities, but this is not systematic.

Effect of silica concentration on kinetics and gel structure

Above, we showed that only silica volume fraction, ϕ, plays a significant role in both the structure and ultimate mechanical properties of the gels. The influence of ϕ on the gel formation is illustrated in Fig. 2.13, in which we present the storage modulus G' and loss modulus G'' at constant salt concentration ([NaCl] $= 0.454$ M)

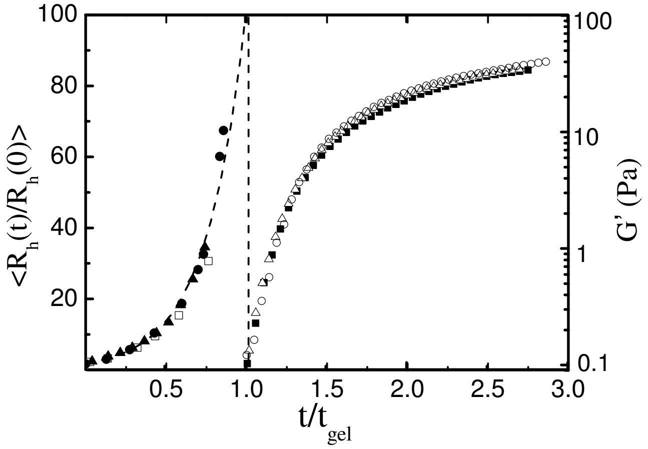

Figure 2.11: Combination of the growth of hydrodynamic radius R_h and storage modulus G' as function of time for samples with silica volume fraction $\phi = 1.0$ % and varies salt concentration. The left dashed line is exponential fitting to R_h; the other line indicates the gel time.

and frequency (1 Hz) for $\phi = 1\%$ and $\phi = 2\%$. The increase in G' and G'' is quite similar to the case seen above. Here, we see that the particles aggregate faster in the higher-ϕ sample: the gel time for $\phi = 2$ % is roughly 1/4 the value of the more dilute $\phi = 1\%$ ($t_{gel} = 97$ min and $t_{gel} = 407$ min respectively). The gel with high silica volume fraction ($\phi = 2\%$) builds a stronger network, with G' almost 10 times larger than the one with $\phi = 1\%$, roughly consistent with $G' \sim \phi^{3.3}$. For higher ϕ, particles are in closer proximity, giving rise to a shorter gel time. In addition, there are more particles in a unit volume for higher ϕ, making contributions to the gel network; as a result, the system displays a stronger network, and hence higher value of G'. Fig. 2.14 shows that the scaling behavior of t/t_{gel} collapses the G' data for $1\% \leq \phi \leq 4\%$, showing again that the salt concentration only effects the gel time not the strength of the particle network at the scaled time. Rueb & Zukoski (1997) used a first-order model[69] to describe the growth of G'. Based on their model, we proposed a similar

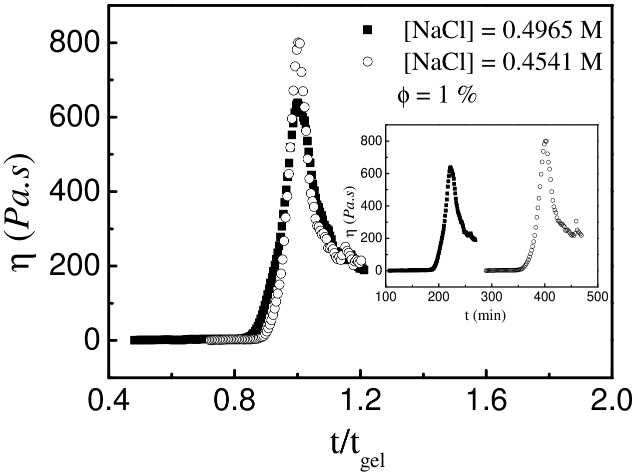

Figure 2.12: The change in viscosity, η, during gelation process at a shear rate of $\dot{\gamma} = 0.01\ s^{-1}$ ($\blacksquare, \phi = 1.0\%$, [NaCl] = 0.4965; $\square, \phi = 1.0\%$, [NaCl] = 0.4541 M).

model,

$$G' = G'_{\infty}(1 - \exp[-\alpha(t/t_{gel} - 1)^{\beta}]), \tag{2.13}$$

where α is the rate of increase of G', which is a measure of the rate of increase in structure or the degree of connectedness within the gel; β is a stretched exponential coefficient (due to low solid volume fraction compared with Rueb's dense systems). The red solid curves show the results of fitting the experimental data to the above model within a scaled time $1 \leq t/t_{gel} \leq 4$. The model matches the data well in the scaled time range. The inset of Fig. 2.14 shows the growth of storage modulus of system with volume fraction $\phi = 2$ % for larger time range, in order to check the prediction of this fit. As shown in the inset, the model works well to the scaled time $t/t_{gel} = 10$; after which, the prediction saturates more rapidly than the experimental G', which continues to grow. Although it does not perfectly match the experimental

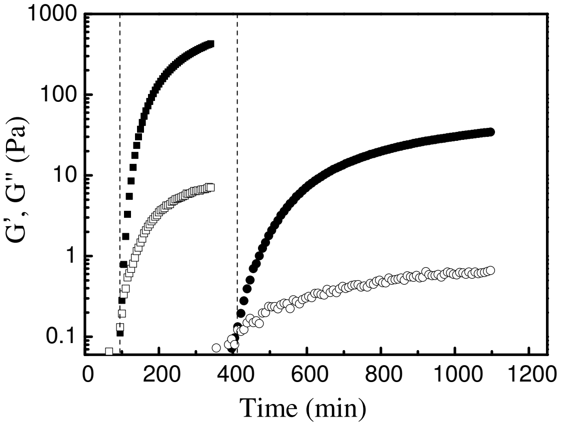

Figure 2.13: The growth of G' (solid) and G'' (open) as function of time for samples with the same salt concentration [NaCl] = 0.454 M ($\blacksquare, \square, \phi = 2.0$ %, $t_{gel} = 97$ min; $\bullet, \circ, \phi = 1.0$ %, $t_{gel} = 407$ min). The dash lines indicate the gel time.

data, it enable us to predict the stiffness of the gel network a relatively long time after salt addition.

2.4 Discussion and Conclusion

In this study, we have focused on the gelation of low volume fraction colloidal silica suspensions. We have modified the effect of interparticle force by manipulating ionic strength of the dispersion, simply by changing salt concentration in the aqueous suspending fluid. We have explored the gel time, gel structure and properties by DLS, SLS and rheological measurements. In particular, we have determined the time to gelation by each method. Accordingly, we have gained understanding on the sudden reduction of mobility as well as the divergence of relaxation time from DLS on the threshold of gelation, which coincides with a measurable elastic modulus in the rheology; the viscosity shows a dramatic increase at the gel point under weak shear. The structure of the aggregates during the gelation process is

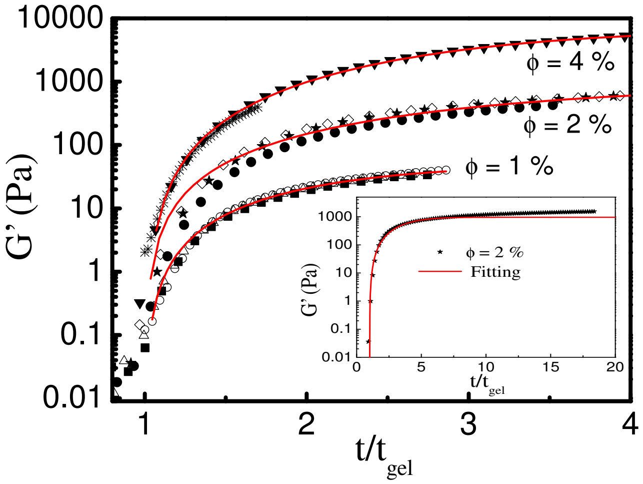

Figure 2.14: The scaling behavior of the storage modulus G' for samples with silica volume fraction $\phi = 1.0 - 4.0\%$ when time is scaled by t/t_{gel}. Dots: experimental data; solid red lines: fittings to equation $G' = G'_\infty(1 - \exp[-\alpha(t/t_{gel} - 1)^\beta])$. For $\phi = 1, 2, 4$ %, respectively, $G'_\infty = 49.1, 954.2, 6700.7\ Pa$; $\alpha = 0.55, 0.17, 0.16$; $\beta = 1.64, 1.61, 2.07$.

investigated by static light scattering to determine the fractal dimension, D_f. We found $D_f \approx 2.0$. This fractal dimension is slightly below values found by other authors for a reaction-limited aggregation process (e.g. [68]), but we have demonstrated the ability to tune the aggregation rate (and hence gelation time) over orders of magnitude using the dependence of the repulsive portion of the interparticle force potential upon the ionic strength of the solvent. It is generally agreed that the RLA process provides more opportunities for particles and clusters to interpenetrate and results in more compact clusters than diffusion-limited aggregation [78]. However, our results finding values of the fractal dimension slightly below the value of $D_f = 2.1$ predicted by RLA simulations suggest that the detailed form of the repulsive potential and the hydrodynamic interactions of particles must be accounted in simulation of nanoparticle gelation. Our ongoing work explores this last issue, and will be reported later.

The combination of results from both dynamic light scattering and rheology indicates that there is a universal behavior in the particle aggregation and gelation process. We found that the size, the structure, the viscosity and the elastic properties of the aggregates/gel exhibit similar behavior for a given silica volume fraction when the time is scaled as t/t_{gel}. This suggests that the salt concentration only affects the electrostatic repulsive barrier, and consequently changes the aggregation rate and the gel time. The observation that scaling by the measured gel time in RLA for silica particle gelation provides a collapse of the data both before and after the gelation for same ϕ leads to the interpretation that cluster growth and gelation are composed of a set of microscopic aggregation events, which are, statistically speaking, essentially similar for different gel times. Thus the gel time may be viewed as some multiple N of a microscopic time t_{micro}, i.e. $t_{\text{gel}} = Nt_{\text{micro}}$, which varies with the salt concentration; the salt concentration effect is presumably due to the change in the pair interaction potential, with the 'reaction time' reduced as the repulsive part of the pair potential decreases owing to salt addition.

The microscopic time has not been probed here, but we can gain insight by noting that a similar collapse of data by Sefcik *et al.*[59] for the post-gelation properties only in a surfactant-stabilized polymer latex, used a scaling of time as t/t^* where $t^* = (3\eta W)/(8kTn_0)$ is a time scale based on microscopic properties of the sol. The quantity W is termed the *stability ratio* of primary particles and captures the 'reaction' aspect of the process, n_0 is the number density of primary particles in the initial sol, and other symbols have their definition used above in describing our work. The stability ratio is defined as the rate of aggregation of pairs in the pure diffusion limit to this rate under the actual conditions and is thus deduced from data on the initial growth of clusters; for RLA, $W > 1$ and can, in fact, be very large. The number density can be written $n_0 = 3\phi/(4\pi a^3)$. Hence, if there is no repulsion between particles, $W \to 1$ and this time may be written $t^* = 4\pi\eta a^3/8kT\phi$, showing that intrinsic rate for motion on the particle scale is given by Brownian diffusion $t_{\mathrm{Br}} \sim a^2/D_0 \sim \eta a^3/kT$ and increasing ϕ decreases aggregation time as distances between particles are decreased. However, when there is a repulsive portion of the pair interaction, many 'attempts' are needed for a particle to cross the barrier and become a part of an aggregate, so that the microscopic timescale becomes

$$t^*(= t_{\mathrm{micro}}) = \frac{4\pi\eta a^3 W}{8kT\phi},$$

where we now suggest that it may be appropriate to equate $t^* = t_{\mathrm{micro}}$ in our expression $t_{\mathrm{gel}} = Nt_{\mathrm{micro}}$.

The remarkable aspect of the collapse under this scaling is that a single time is able to satisfactorily describe the basic process for materials which are radically different in structure and properties. This collapse was limited in our work to $\phi \leq 4\%$, but extended to higher ϕ in [59] suggesting some differences in the extent of the repulsive potential relative to the particle size (i.e. Debye length effects). We propose a simple gelation mechanism to help illustrate the gelation process. The transition from sol to initial gel and final gel is composed of a series of identical steps (t_{micro}). The number of steps (N) needed to reach initial gel or final gel state are the same for fixed ϕ, independent of salt concentration. However, the height of the step varies with the salt concentration (higher salt concentration means smaller t_{micro}). At each step ($t = n_i t_{\mathrm{micro}}$), the cluster or gel has the same structure and properties. When the time ($t = n_i t_{\mathrm{micro}}$) is scaled by the gel time ($t_{gel} = Nt_{\mathrm{micro}}$), the scaled time will be $t/t_{gel} = n_i/N$. The cluster or gel properties as a function of the scaled time thus are independent of the salt concentration during the gelation process. The key point is that for a fixed ϕ, the gel time is a *fixed* multiple $N(\phi)$

independent of the ionic strength. Since the dynamic data continue to be collapsed to a master curve after gelation when time is scaled by t_{gel}, we conclude that a similar microscopic timescale is operative in setting the growth rate of the network after initial gel formation. A practical benefit is that this scaling behavior enables us to predict the kinetic and mechanical properties for the gelation of colloidal silica suspensions for salt concentrations not studied.

Chapter 3

Hydrodynamic and interparticle potential effects on aggregation of colloidal particles

3.1 Introduction

This work studies the aggregation of dispersed Brownian particles through dynamic simulation. In applications, good control of aggregation and gelation of colloidal systems is desired, and it is very well established that this may be achieved through tuning of the particle interaction potential. In addition to interaction through a potential, the particles interact hydrodynamically. Because the gelation process results in a nonequilibrium structure, hydrodynamic interactions, which result from the flow induced by the motion of one particle affecting the motion of neighboring particles, may also play a role in setting the structure. It is our general goal to develop understanding of how the potential and hydrodynamic interactions give rise to the microscopic and mesoscopic features of aggregation relevant to gelation of colloidal dispersions. To date, the role of hydrodynamic interactions has not been explored in detail, in particular not for a range of interaction potentials which allow control of the rate of aggregation. To determine the role of hydrodynamics on the process, we compare results of the aggregation process from two established simulation methods for colloidal particle dynamics, namely Brownian Dynamics and Stokesian Dynamics. We study a wide range of interaction potentials for each method.

In practice, the interaction potential, U, between the suspended particles may be varied in a number of ways, each specific to the type of colloidal dispersion studied. These include alteration of the pH, ionic strength, temperature, or size and concentration of a soluble polymer (which induces depletion forces between the colloidal particles) [79, 80]. We consider particles which interact through a long-ranged interaction potential with both a strongly attracting portion as well as a variable strength repulsion, modeling particles that carry a surface charge yielding the repulsive part of the interaction; the attractive portion of the potential may result in physical systems from van der Waals or solvation forces [81, 82, 83]. This work addresses particles with interaction range on the order of the particle size. This is most often representative of nanoparticle dispersions, although Campbell *et al.* [84] showed that near micron scale, particles could have decay length comparable to their size in nonaqueous liquids.

The balance of particle forces during gelation determines the kinetics and mechanism of aggregation and the resulting structure and properties of the final gel. Many studies have been devoted to the study of gelation simulation [44, 3, 43, 42]. Clearly, the liquid in which the particles are dispersed will influence the rate of Brownian motion through the viscosity of the fluid, η, which sets the isolated particle diffusivity $D_0 = k_B T/(6\pi\eta a)$. The long-ranged many-body hydrodynamic interactions result from the fact that a particle motion generates a flow field, and this must be accounted for to properly describe the dynamics of aggregation processes. Our interest is to address whether the hydrodynamic interactions alter the dynamics in such a way that they alter the ultimate structure of the gelled or percolated structure. Hydrodynamic interactions (HI) have not been included in most simulational studies of aggregation or gelation [44, 85, 24, 41, 3].

Quite recently, however, this has begun to change. Yamamoto *et al.* [86] and Furukawa *et al.* [87] both used direct solution methods to resolve the fluid mechanics and capture HI in simulations of colloidal dispersions undergoing aggregation; the results of these simulations were compared against Brownian Dynamics simulations in which interactions by hydrodynamics are neglected. In each of these studies, the potential lacks a long-range repulsion, with Yamamoto *et al.* [86] considering a standard Lennard-Jones 6-12 potential, and Furukawa *et al.* [87] using an Asakura-Oosawa-type potential (modeling depletion flocculation). Implications of the repulsive portion of the potential, which is considered in most of our simulations reported here, is discussed below in relation to whether the aggregation mechanism is 'diffusion-' or 'reaction-limited'. Yamamoto *et al.* [86] studied transient gels (where the interaction potential minimum is typically less than 5 k_BT) in both two and three dimensions, exploring the earlier observation from two-dimensional simulations by Tanaka *et al.* [88] that HI had stabilizing effects on tenuous network-forming nonequilibrium structures. However, when they considered three-dimensional dispersions, Yamamoto *et al.* [86] found that HI had only minor influence on the structure. By contrast, Furukawa *et al.* [87] argued based on their simulations that HI plays a key role, lowering the particle volume fraction threshold necessary for percolation. By considering the evolution of isolated groups of particles under conditions with and without HI, Furukawa *et al.* [87] showed that there is a distinct difference in the evolution of structure of such small systems, providing some indication of the way in which the HI caused the observed changes.

There is thus some confusion over the influence of hydrodynamic effects in aggregation even in the limited body of study addressing this basic question. In addition, the effects of hydrodynamic interactions for variation of the potential have not been explored. We consider in this work a system corresponding qualitatively to a charge-stabilized dispersion rendered unstable by addition of ions (Lattuada *et al.* 2003, Cao *et al.* 2010). The most well-studied case corresponding to this description is colloidal silica dispersion in aqueous solvent. Under basic conditions (high pH), there is negative charge on the surface of the particles, which stabilizes the dispersion against flocculation by making close approach of particles energetically unfavorable, and the dispersion can be stable indefinitely. Increasing the ionic strength by adding an ionic solution to the dispersion decreases both the range and the magnitude of electrostatic repulsion by reducing the Debye screening length. This screening effect of added salt leads to destabilization of the kinetically stable system and hence to aggregation and space-filling network formation (gelation) [60].

The aggregates (or clusters) in a gelling dispersion can be described by their fractal dimension D_f defined in terms of the radius of gyration of the cluster, R_g, as $R_g \propto N^{1/D_f}$ where N is the number of particles in the cluster. The radius of gyration can be obtained experimentally by static light scattering method as shown by numerous authors. There are two limits for particle gels in the aggregation process, diffusion-limited cluster aggregation (DLCA) and reaction-limited cluster aggregation (RLCA), as defined by Meakin [89] with respect to 'probability of bonding' due to particle interactions. In DLCA, particles form bonds with probability one on contact. As there are more opportunities for contact at the periphery of a cluster, growth of the number of particles is dominated by attachment there, and DLCA yields a large-pore structure with fractal dimension of $D_{f,\mathrm{DLCA}} \approx 1.8$. In RLCA, the bonding probability is less than unity, and particles thus have a chance to explore multiple bonding sites including those on the interior of cluster, leading to a more condensed network with higher fractal dimension of $D_{f,\mathrm{RLCA}} \approx 2.1$ [68, 24]. The 'reaction' here is the passage across an energy barrier, which in the charge-stabilized system results from the Coulombic repulsion. This may be tuned by ionic strength to vary the rate of the so-called reaction, as shown in our recent work to explore the evolution of the structure and rheology of colloidal silica [90]. The rate of aggregation, Z, may be written for a dilute dispersion as $Z = K\phi^2$ with ϕ the particle volume fraction, and the rate constant K is proportional to the probability a pair of particles near contact will pass over the barrier. This concept is captured by the 'stability ratio' W_F of the primary particles with $K \sim D_0 a^2 W_F^{-1}$, where D_0 is the diffusivity, a is the particle radius, and $W_F = 2a \int [\exp{(U(r)/kT)}/r^2] dr$ with r the center-to-center distance of the pair. In general, W_F is difficult to compute for an experimental system, and is determined from observation as the ratio of dimer formation in the case of no barrier (i.e., DLCA conditions without hydrodynamics) to that under the actual conditions. In a dispersion aggregating under truly reaction-limited conditions, values of $W_F \gg 1$ are expected, as illustrated in the work of Lattuada *et al.* (2003), with the application of W_F in the expression of all the aggregation kernels of the population balance equations [38]. Mellema *et al.* (1999) applied the stability ratio W_F to relate the cluster growth and the structure of the cluster with the interpaticle interactions. They investigated the dependence of the fractal dimension D_f on W_F and the particle volume fraction ϕ and found that D_f is less dependent on W_F and ϕ for high W_F.

As noted, a repulsive potential is able to stabilize colloidal dispersions indefinitely, and thus the potential is of pronounced influence on the dynamics of diffusing particles. The influence of interaction potentials on dispersion behavior in the absence of hydrodynamic influence has been studied by simulation by many authors in recent years, and we cite a few examples considering different forms of the potential. For example, in a study of a short-range potential of purely attractive interactions, modeling depletion-induced aggregating systems, Lodge *et al.* [41] applied Brownian Dynamics simulation to investigate the dynamics and rheology of transient colloidal gels formed by particles interacting via generalized Lennard-Jones interaction $U(r)/k_BT = A[(2a/r)^{2n} - (2a/r)^n]$ with $n = 6$, 12 and 18, with a the spherical particle radius and r the pair center separation. They found that the arrested state is due to an interrupted phase separation. It is well-known that repulsive potentials can lead to colloidal crystals [91]. Interestingly, Zaccarelli *et al.* [92] showed that a long-ranged repulsion may generate Wigner glasses in simulations of dilute binary (50 %- 50 %) systems. The case of a combined short-ranged attractive potential and long-ranged repulsive potential is the most complicated; note that there is also a repulsive interaction at contact. Sciortino *et al.* [45] studied the equilibrium cluster phase by molecular dynamics simulations in a system where particles interacted through such a combined potential. By the proper choice of parameters of the potential, they were able to obtain a disordered nonequilibrium arrested state. Charbonneau *et al.* [46] applied the Gibbs ensemble Monte Carlo technique to study phase behavior in two-dimensional systems with long-ranged repulsive and short-ranged attractive interactions. They demonstrate that gelation may occur as the result of arrested micro-phase separation. Kumar *et al.* [47] investigated the structural properties of chain-like clusters.

In this chapter, we focus on the effect of repulsive barrier and the hydrodynamic effects during the aggregation process. The potential studied includes a generalized Lennard-Jones potential and a Yukawa potential which captures a short range (e.g. van der Waals) attraction and long range screened electrostatic repulsion between particles. In addition, we study the influence of hydrodynamic interactions on the gel network formation. The simulation systems are limited in size to less than 1000 particles in order to consider hydrodynamic effects for the extended physical times studied. It is thus not possible to capture the behavior of numerous interacting clusters for dilute dispersions, and we instead seek to use these simulations to understand the development of structure on the microscopic scale of the particles and at the mesoscopic scale where the structure transitions to a fractal scaling.

We begin, in the following section, by describing the simulation methods. Results and discussion are presented in Section 3, followed by conclusions drawn from the work.

3.2 Numerical Simulations

We study the dynamical aggregation process in a particle dispersion, with monodisperse spherical particles of radius a interacting under continuous interparticle potentials. The potential of interaction between any pair is identical within a given simulation but is varied widely in different simulations. We apply both Accelerated Stokesian Dynamics (ASD [93] will be used to denote this implementation; SD described in [94] will be used to denote the general algorithm) and Brownian Dynamics (BD) [95] techniques to simulate three-dimensional motions in a periodically replicated cubic unit cell. The ASD method reduces the calculation cost of the standard SD algorithm through a particle-mesh Ewald treatment of the interactions of particles at large; the method inclusive of Brownian motion is described by Banchio *et al*. [96] and a similar technique is described for both nonBrownian and Brownian particles in the papers [97, 98].

The number of particles simulated within the unit cell is denoted N and we report results almost exclusively for $N = 864$ in this chapter. In the final part of the results, a study of three-particle clusters is described; in this case, the simulation box contains 64 groups of three particles, so that $N = 192$.

In the discussion which follows we will consider time in dimensionless form, with the scaling being $\tau = a^2/D_0$, i.e. the time for a particle to diffuse its own radius at infinite dilution, where $D_0 = k_BT/(6\pi\eta a)$ is the Stokes-Einstein diffusivity and η is the viscosity of the solvent and k_BT is the thermal energy (k_B is the Boltzmann constant and T is absolute temperature). Starting configurations for the simulations were generated from initially random distributions of particles having the appropriate solid fraction.

Because the scale of the particles is very small, we assume the fluid motion is decribed by the Stokes equations. The particle motion is described by the N-body Langevin equation,

$$\mathbf{M}\frac{d\mathbf{U}}{dt} = \mathbf{F}^H + \mathbf{F}^B + \mathbf{F}^P, \tag{3.1}$$

where $\mathbf{M}$ is the combined particle mass and moment of inertia tensor, $\mathbf{F}^H$ is the hydrodynamic force-plus-torque exerted by the fluid on the particles, $\mathbf{F}^B$ is the stochastic force due to Brownian motion, and $\mathbf{F}^P$ represents the interparticle force.

The two simulation methods used differ in the treatment of the hydrodynamic interactions (HI). The primary influence is thus seen in $\mathbf{F}^H$ which is written for SD (whether in standard or accelerated form) on the basis of linearity of the governing Stokes equations as $\mathbf{F}^H = -\mathbf{R}_{FU} \cdot U^* + \mathbf{R}_{FE} : \mathbf{E}^\infty$, where U^* describes the particle translational-angular velocity relative to the bulk fluid translational-angular velocity at the particle center. The tensor $\mathbf{R}_{FU}$ defines the hydrodynamic force-plus-torque on the particles due to their motion relative to fluid while the term $\mathbf{R}_{FE}$ relates the hydrodynamic force-plus-torque on the particles due to imposed shear flow. The symmetric part of the bulk velocity gradient tensor is the strain rate, denoted $\mathbf{E}^\infty$. For most of this work we will consider a system with no bulk flow, so that $\mathbf{E}^\infty = 0$, but the presence of the $\mathbf{R}_{FE}$ term (which is absent if hydrodynamics is neglected) illustrates a key concept of HI: the disturbance flow caused by one particle in a flow causes a second particle to move (or experience a force); for an isolated pair of spheres, $\mathbf{R}_{FE} \sim r^{-3}$ with r the separation of the pair. More directly relevant for the present study is the fact that $\mathbf{R}_{FU}$ depends on r, with a long-range effect owing to the slowly decaying velocity field on a particle translating due to a force (e.g. in a sedimentation): this velocity decays as r^{-1} where r is the distance from the particle; thus there is significant effect on the motion of (or forces on) particles even many diameters away. At close separations, where the gap between particle surfaces becomes small, i.e. $O(\epsilon a)$ with $\epsilon \ll 1$, lubrication interactions lead to $\mathbf{R}_{FU} \propto \epsilon^{-1}$ and thus relative motions of particles are strongly inhibited by the intervening fluid in near-contact configurations. Detailed description of hydrodynamic interactions is available in Kim & Karrila (1989) [99]. In BD, the HI is neglected and only the hydrodynamic drag from the fluid is considered. For the case of BD, the hydrodynamic force can be simply expressed as $\mathbf{F}^H$ = -ζU, where $\zeta = 6\pi\eta a$ where η is the fluid viscosity.

To account for the thermal collisions of the solvent molecules with the particles, the Brownian force satisfies the fluctuation-dissipation theorem at equilibrium and its strength is described by $\langle \mathbf{F}^B(0)\mathbf{F}^B(t)\rangle = 2k_BT\mathbf{R}_{FU}\delta(t)$.

The interparticle force $\mathbf{F}^P$ is the same for the two simulation techniques, and is written as the gradient of a pair interaction potential $U_N(\mathbf{x}^N)$ with the argument indicating the dependence of the energy on all particle positions,

$$\mathbf{F}_i^P = -\nabla_i U_N,$$

and ∇_i indicating the gradient with respect to the position of particle i. The form of the potential U studied here is pairwise additive with the pair potential given by the specific form

$$U(r)/k_BT = A[(\frac{2a}{r})^{2n} - (\frac{2a}{r})^{n}] + B\exp[-\kappa(r-a)]/r, \tag{3.2}$$

where $r = |\mathbf{r}|$ is the magnitude of the center-to-center pair separation vector, $\mathbf{r}$. The pair potential is illustrated in Figure 3.1: note that there is a repulsive barrier away from contact and a generalized Lennard-Jones $(n - 2n)$ form. We have plotted the pair potential for several values of κ with the standard set of other parameters used, namely $A = 60$, $B = 20$, and $n = 18$; slight alterations of the parameters used to maintain the depth of the primary minimum will be noted later. The electrostatic energy of repulsion between like charge surface arises from the surface charges and from overlap of electrical double layers surrounding the two particles. The range of interaction is of the order of the Debye length (κ^{-1}). For 1:1 electrolytes the value of κ^{-1} is approximately 10, 3, 1 nm for concentrations of $10^{-3}, 10^{-2}$,and 10^{-1} M, respectively [100]. The Debye length becomes comparable to the particle size for 10-nanometer particle dispersions in aqueous media at low ionic strength. For particles of micron scale, experimental work by Campbell *et al.* [84] showed that in non-aqueous media, κ^{-1} can be comparable to the particle size because ion solubility is low. The model of the repulsion is thus broadly relevant in terms of the particle size for which it is experimentally realizable.

3.3 Results and Discussion

3.3.1 Evolution of aggregate structure

The evolution with time of the aggregation process for one realization is shown in Figure 3.2, where snapshots are presented. Here, the conditions are $\phi = 0.12$ and

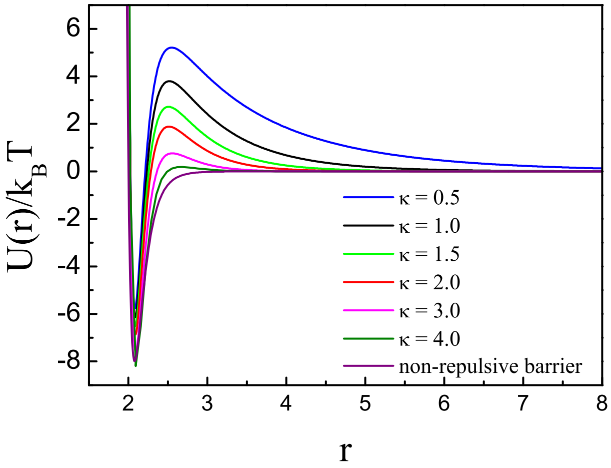

Figure 3.1: Potential energy ($U(r)/k_BT = A[(\frac{2a}{r})^{2n} - (\frac{2a}{r})^n] + B\exp[-\kappa(r-a)]/r$) with $A = 60$, $B = 20$, $n = 18$ and varying κ. For the potential without repulsive barrier, $A = 32$ and $B = 0$ are used to maintain the depth of the primary minimum.

$\kappa = 3.0$. The particles are homogeneously distributed within the simulation box in the initial configuration at $t = 0$. Under the influence of Brownian motion, particle interaction and hydrodynamic force, the particles form clusters. The clusters grow and merge until they percolate across the unit cell at $t \approx 50$, with time scaled by a^2/D_0. Particles and smaller clusters which are not at this time part of the percolated network continue to move. The aggregation rate slows as larger clusters form. The structure does not appear visually to change much from time $t = 100$ to 150, although additional particles gradually attach to the arrested network.

The influence of the repulsive potential on the cluster structure is considered in Figure 3.3. The structure of the aggregates at $t = 109$ and $\phi = 0.12$ is significantly affected by the form of the potential. For the lower repulsive barriers of $\kappa = 3.0$ and 4.0, large condensed clusters appear along with large regions of low or no particle concentration. With increasing repulsive barrier (reducing κ), the systems form a

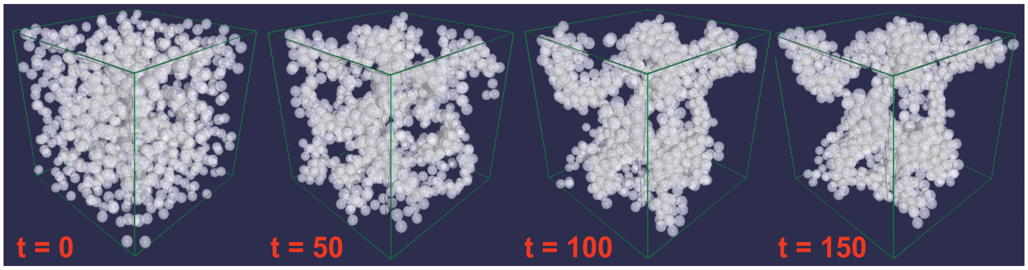

Figure 3.2: The evolution of cluster structure during aggregation $\phi = 0.12$, $\kappa = 3.0$ for different times, t; recall that time is scaled by a^2/D_0.

more loose structure with a more homogeneous particle distribution.

3.3.2 Radial distribution function

The pair distribution function, $g(\mathbf{r})$, gives the probability of finding a particle at position $\mathbf{r}$ from another particle, relative to the likelihood without knowledge of a particle position. Because the dispersions studied are isotropic in average, we consider the radial distribution function, $g(r)$, evaluated by sampling of all pairs and binning the results in the r direction. We use bins of $\Delta r/a = 0.025$.

The evolution of $g(r)$ for $\phi = 0.12$ and $\kappa = 3$ is shown in Figure 3.4. Initially, particles are homogeneously distributed with $g(r)$ showing in Figure 3.4 (a), indicating fluid-like state. At $t = 5$, Figure 3.4 (b) shows a rapid increase in $g(r/a = 2.09)$, indicating the formation of doublets, triplets and small particle clusters. During the aggregation process, $g(r)$ at $r/a = 2.2 - 3.0$ drops sharply; while at $r/a \doteq 3.5$, 4.2, and 5.4, $g(r)$ gradually forms peaks, indicating local structure formation. $g(r/a = 2.09)$ evolves very slowly from $t = 50 - 150$, as a space-filling particle network forms. Figure 3.5 shows the radial distribution function in the time window t = 105 - 110, for $r/a = 2 - 6$, in dispersions of $\phi = 0.12$ for $\kappa = 0.5$, 1.5 and 4.0. For each of the three systems, there is a large peak near contact, at $r/a = 2.09$ which is roughly the point of the minimum in the pair potential. The peak in g increases modestly

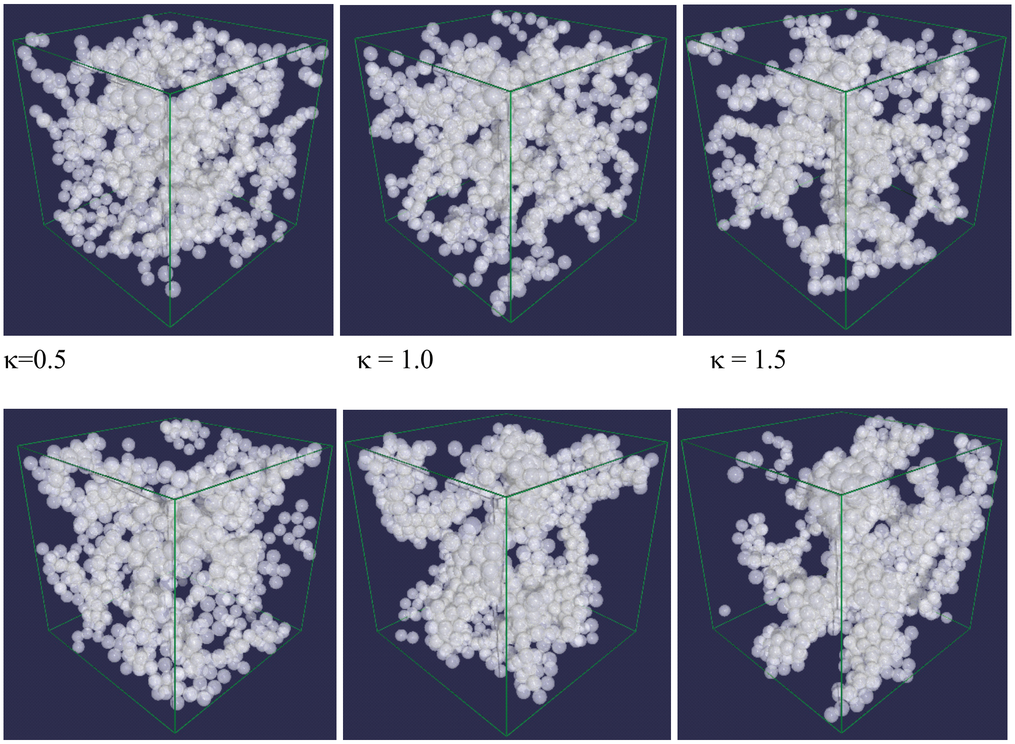

$\kappa=0.5$ $\kappa = 1.0$ $\kappa = 1.5$

$\kappa = 2.0$ $\kappa = 3.0$ $\kappa = 4.0$

Figure 3.3: Instantaneous aggregate structure for $\phi = 0.12$ with different repulsive barriers at time $t = 109$; recall that time is scaled by a^2/D_0.

in value for a lower repulsive barrier. The possibility of finding another particle in the spherical annulus $2.2 \leq r/a \leq 3.1$ is very small for systems with $\kappa = 0.5$; as κ increases, neighboring particles are increasingly found here. There are three local maxima at $r/a \doteq 3.5$, 4.2, and 5.4, for each of the values of the potential plotted in figure 3.5, indicating general similarity of the structure, but the magnitudes of g at these positions increases with increasing κ (reduction of the repulsive barrier).

Figure 3.6 compares $g(r)$ from ASD and BD simulations for $\phi = 0.12$ for repulsive barrier parameters of $\kappa = 0.5$ and $\kappa = 4$ at simulation time $t \approx 110$. For a large repulsive barrier (e.g., $\kappa = 0.5$), the major peaks at $r/a = 2.09$ are similar from the two simulation methods (inset of Figure 3.6 (a)). The first minor peak at $r/a = 3.5$ from BD simulation is slightly larger than that from ASD simulation. For a smaller

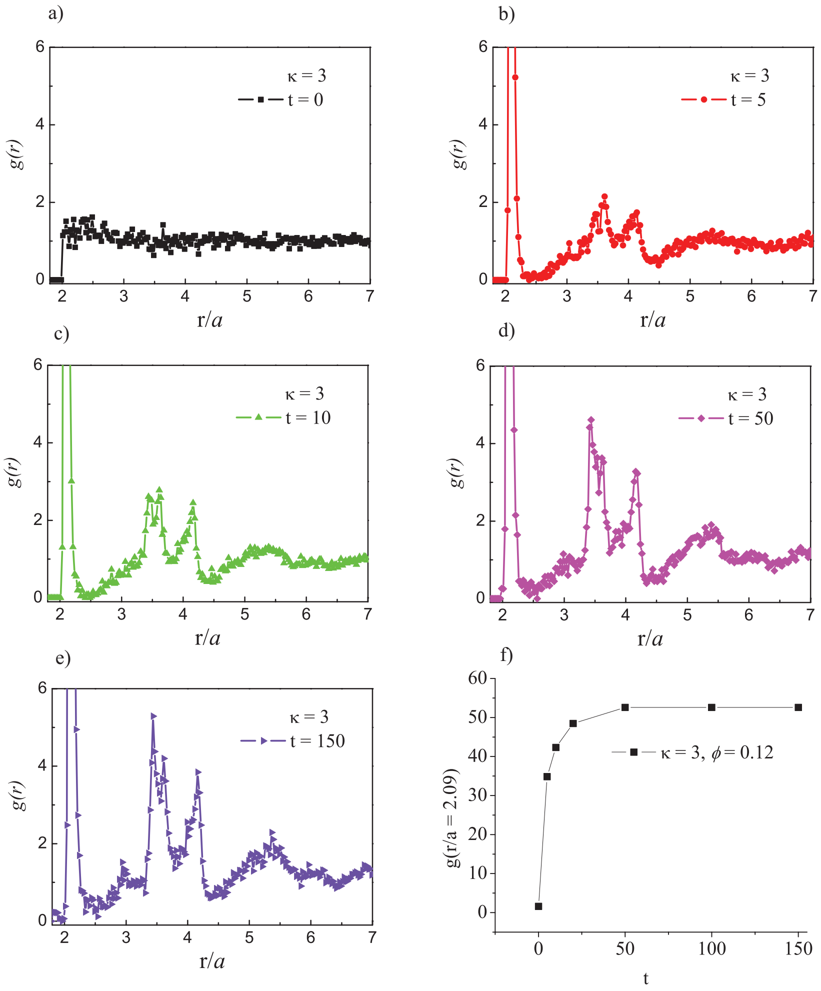

Figure 3.4: (a) - (e): The radial distribution function $g(r)$ at various times t (t scaled by a^2/D_0) for $\phi = 0.12$ and $\kappa = 3$; (f): $g(r/a = 2.09)$ as function of time t.

repulsive barrier, e.g. $\kappa = 4$ as shown in Figure 3.6 (b), there is a small difference in the major peak. The results of the minor peaks from both ASD and BD simulations are similar, indicating similarity in the computed local structure.

3.3.3 Number of bonds

During the aggregation process, if particles are driven over the repulsive barrier, they tend to remain for the remainder of the simulated time in the primary minimum of the energy potential ($r_{E_{min}}/a \doteq 2.09$). The depth of the energy minimum relative

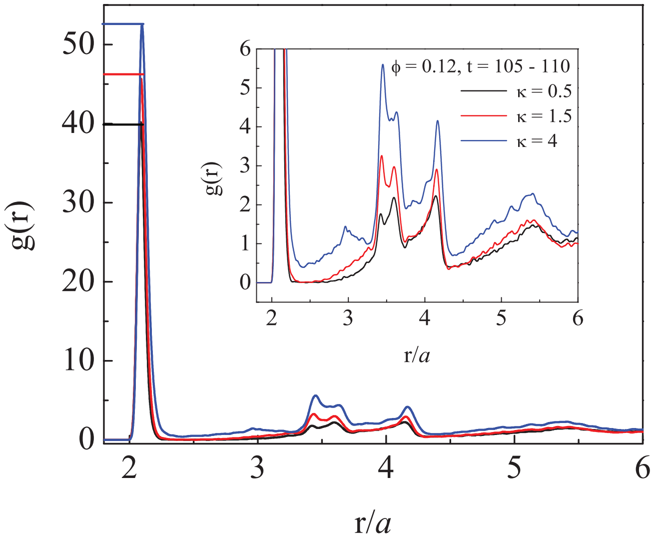

Figure 3.5: The radial distribution function $g(r)$ averaged over the time window t = 105-110 (t scaled by a^2/D_0) for $\phi = 0.12$, with κ = 0.5, 1.5, and 4.0; inset: blow up of $g(r)$ for the same conditions.

to the maximum of the repulsion varies depending on κ but is in all cases greater than $6k_BT$. We thus consider a 'bond' to be formed if a particle pair is at a distance less than $r_{max,bond}/a = 2.21$, which is the outer limit of the attractive portion of the potential. The number of bonds is denoted N_b.

The growth of the bonds per particle, N_b/N, for $\phi = 0.12$ and varying repulsive potential is indicated in Figure 3.7; note that a case with no long-range repulsion is included, and here $A = 32$ is used to maintain similar depth of the primary minimum. For each κ, the number of bonds per particle grows quickly in the early stages of aggregation, and the rate of growth slows as large clusters appear. For larger repulsive force ($\kappa = 0.5$ and $\kappa = 1.0$), the rate of bond formation is slower than the systems with low repulsive barrier ($\kappa = 3.0$ and $\kappa = 4.0$), as indicated by the initial slope in Figure 3.7. This rate is termed the aggregation rate. At $\kappa = 4.0$, the aggregation rate approaches that for a dispersion modeled with no repulsion. Considering Figures 3.3 and 3.7 together, for a high repulsive barrier (small κ), the aggregates form with

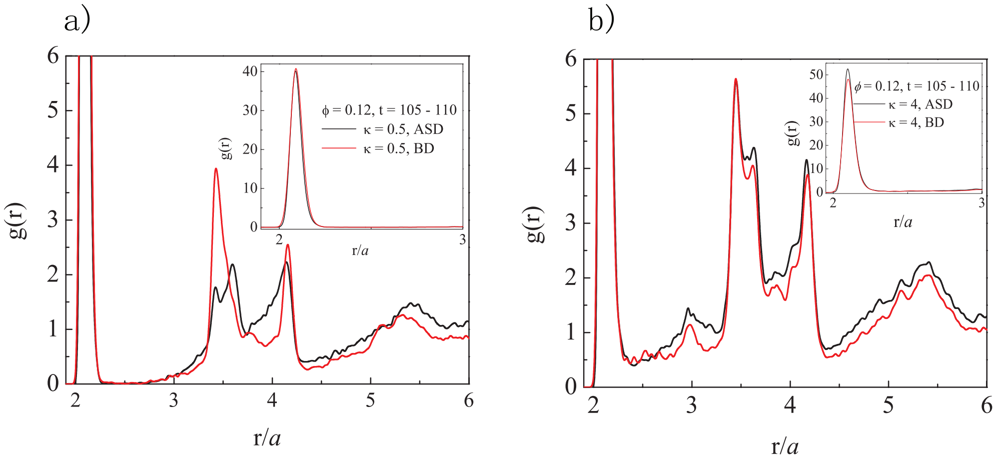

Figure 3.6: The radial distribution function $g(r)$ averaged over $105 < t < 110$ (scaled by a^2/D_0) from Accelerated Stokesian Dynamics and Brownian Dynamics simulations. (a): $\phi = 0.12$, $\kappa = 0.5$; (b): $\phi = 0.12$, $\kappa = 4$; inset: blow up of $g(r)$ for the same conditions.

fewer bonds per particle, and at a later time. This is consistent with the possibility that the long-ranged repulsion may lead to the formation of an arrested state in a low-density particle system, as discussed in the work of Sciortino *et al.* [45] and Charbonneau *et al.* [46]. The bonds per particle increase as the repulsive barrier is suppressed, suggesting more particles in dense clusters, together with large portions of the volume devoid of particles.

The effect of the particle volume fraction on bonds per particle for systems with $\kappa = 3.0$ is weak as shown in Figure 3.8. At early aggregation time ($t = 0$ - 75), the rate of bonds per particle depends slightly on ϕ in the range studied of $0.05 \leq \phi \leq 0.12$. The bond formation rate increases with ϕ as indicated by the arrow in the figure. At later time, the variation in bonds per particle diminishes for the various ϕ, as this quantity approaches a plateau value which is roughly independent of the volume fraction.

The average bonds per particle from ASD and BD are compared in Figure 3.9 for $\phi = 0.12$, and $\kappa = 1$, 2, and 3. We observe that the bonds per particle from BD simulations are greater than from ASD for each κ. Particles in the BD simulation,

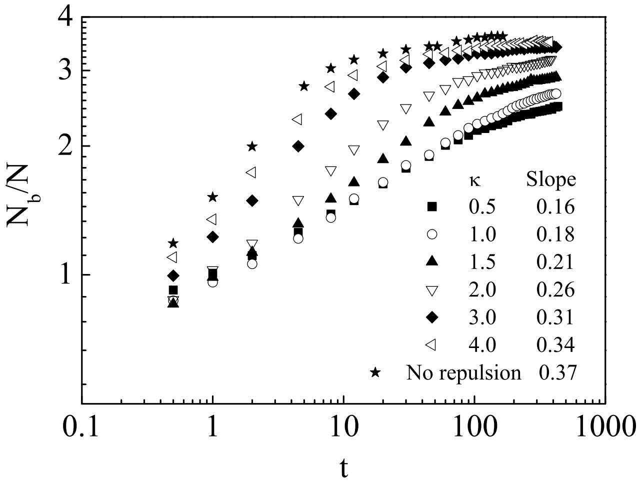

Figure 3.7: Evolution of bonds per particle, N_b/N, for $\phi = 0.12$ and different pair potentials in a dispersion simulated by ASD; time is scaled by a^2/D_0. The legend describes the repulsion parameter (inverse Debye length) κ, except for the case of no repulsion (in this case, the coefficient $A = 32$).

where HI is neglected, aggregate more rapidly. As the repulsive barrier is reduced, the difference of bonds per particle between ASD and BD decreases. This suggests that under the condition when there is no repulsive force, the results from ASD and BD will be similar. The combined effect of hydrodynamic and repulsive forces on the bonds per particle leads to a ramified particle network. Both repulsive and hydrodynamic forces tend to slow the bond formation, leading to the difference in network formation.

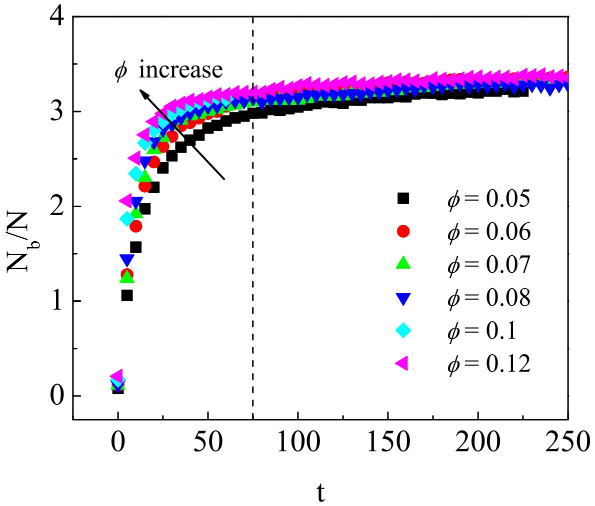

Figure 3.8: Evolution of bonds per particle, N_b/N, for a dispersion simulated by ASD with the standard interparticle potential and $\kappa = 3.0$, at volume fractions $\phi = 0.05 - 0.12$; time is scaled as a^2/D_0.

3.3.4 Static structure factor

To quantify the structural evolution of the system, we have also studied the static structure factor defined by

$$S(\mathbf{q}) = 1 + \rho \int [g(\mathbf{r}) - 1] \exp{(i\mathbf{q} \cdot \mathbf{r})} d\mathbf{r},$$

where ρ is the mean particle number density. While related to the pair (or radial, if isotropic) distribution function the static structure factor provides a useful perspective on the structure at large length scales. Rather than using the above definition, it is convenient for our purposes to compute $S(\mathbf{q})$ directly from the particle positions [101, 102]:

$$S(\mathbf{q}) = \frac{1}{N} \langle \sum_{i,j=1}^{N} e^{iq(r_i - r_j)} \rangle, \tag{3.3}$$

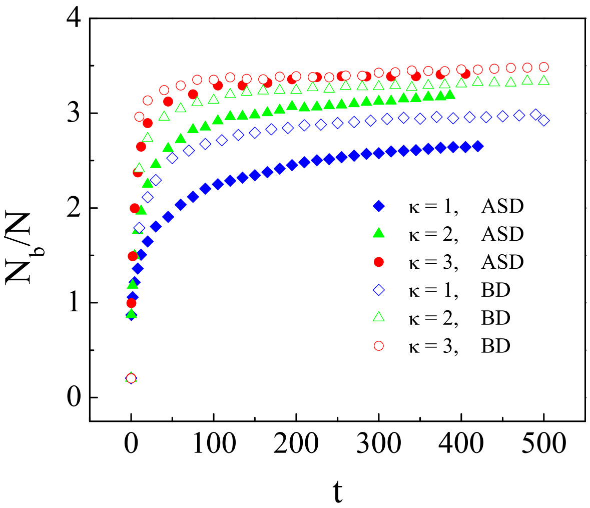

Figure 3.9: Evolution of bonds per particle, N_b/N, for $\phi = 0.12$, and various κ, with time scaled by a^2/D_0. Open symbols represent data from BD simulation; solid symbols represent data from ASD simulation.

where the allowed wavevectors $\mathbf{q}$ are dependent on the size of the simulation box. The allowed values are

$$q_{n_{x,y,z}} = \frac{2\pi}{L} n_{x,y,z}. \tag{3.4}$$

The dispersions are studied without flow and thus $S(\mathbf{q})$ reduces to the isotropic $S(q)$. Computed $S(q)$ for $\phi = 0.12$ and $\kappa = 3$ at different times are plotted as a function of qa, where $q = |\mathbf{q}|$ in Figure 3.10. As the aggregation proceeds $S(q)$ evolves, showing an increase at small wavevectors. The values at small q saturate to a constant value after $t = 100$. This correlates with the behavior seen in Figure 3.9, where most of the bonds have formed by $t = 100$ with a slowing of dynamics afterwards.

The long-wavelength density fluctuations of a system, as characterized by $S(q \rightarrow$

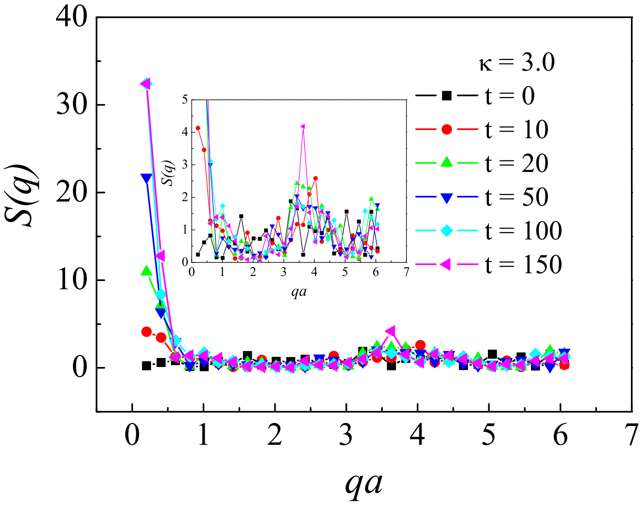

Figure 3.10: Evolution of static structure factor for a dispersion of $\phi = 0.12$ and $\kappa = 3.0$, simulated by ASD with time scaled by a^2/D_0.

0), are related to macroscopic thermodynamics,

$$S(q \to 0) = 1 + \rho \int [g(r) - 1] d\mathbf{r} = \rho k_B T \chi_T, \tag{3.5}$$

where χ_T is the isothermal compressibility. The implication is that a system with large susceptibility to fluctuations approaching macroscopic scale is highly compressible–here the compressibility is of the particles as a phase. Thus, the evolution of $S(q \to 0)$ indicates the development of large inhomogeneities. Several authors have observed the increase in $S(q)$ at small wave vector both in experiments and in simulations [42, 103, 104]. The peak between $qa = 3$ and $qa = 4$ shows that the close-pair structure, as also seen in $g(r)$ for $r \approx 2.09$, develops dense local clustering near contact. Due to the limitation in the simulation box size, the limit $q \to 0$ is inaccessible, and we present $S(q_{min})$, with q_{min} obtained by averaging over the results obtained for wavevectors with $n \leq 3$ in (3.4). The evolution with time of $S(q_{min})$ for different interparticle

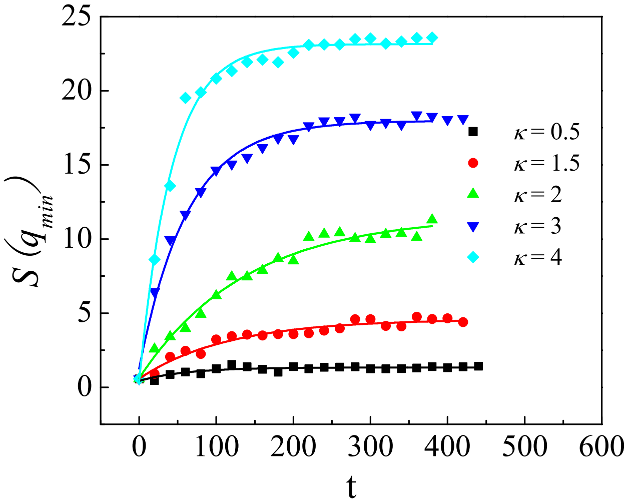

Figure 3.11: Evolution of $S(q_{min})$ for a dispersion of $\phi = 0.12$, at varying κ, from ASD simulation with time scaled by a^2/D_0. Symbols represent the experimental data; lines are fits to the form $S(q_{min}) = S(q_{min})_{plateau} + C * [1 - \exp(-t/\tau)]$.

potential is presented in Figure 3.11. We see that $S(q_{min})$ increases rapidly for $t < 100$, with a slowing down in dynamics afterwards. The plateau level of $S(q_{min})$ is larger for dispersions with larger κ, indicating that decreasing the repulsive barrier between particles increases the heterogeneity on the largest scales accessible (the simulation box size).

Figure 3.12 compares the growth of $S(q_{min})$ at $\phi = 0.12$, for $\kappa = 0.5$, 2.0, 3.0 from both ASD and BD simulations. For larger repulsive barriers, $S(q_{min})$ obtained from ASD simulation is lower than that from BD simulation; this indicates less heterogeneity at the large scale. We interpret large-scale heterogeneity to be associated with complete separation, i.e. similar to phase separation. The ASD simulations which include the influence of hydrodynamics appear to slow this separation, leading to a more ramified and looser structure which spans the unit cell at smaller ϕ than in the BD simulation in which HI are neglected.

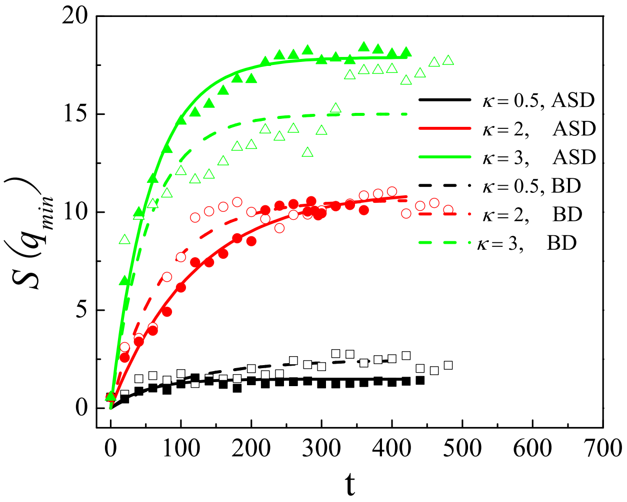

Figure 3.12: Evolution of $S(q_{min})$ with time (scaled by a^2/D_0) for $\phi = 0.12$, and varying κ. Solid symbols are from ASD simulation; open symbols are from BD simulation; solid and dash lines: fittings to $S(q_{min}) = S(q_{min})_{plateau} + C * [1 - \exp(-t/\tau)]$ for ASD and BD simulation, respectively.

3.3.5 Stress evolution during aggregation process

The previous results have shown the structure evolution of the aggregated particle network under various conditions. Here, the development of the mechanical properties of the network are analyzed by considering the stress σ_U arising from the particle interaction potential. Because the dispersion is unsheared, we consider only the isotropic normal stress, with value given by

$$\sigma_U = -\frac{1}{3V} \sum \mathbf{r}_{ij} \mathbf{F}_{ij}, \tag{3.6}$$

where $\mathbf{F}_{ij}$ is the interparticle force, i and j label the particles, and V is the total volume. Figure 3.13 shows the plot of the stress -Trσ_U during the aggregation process for volume fraction $\phi = 0.12$ and different interparticle potentials.

The stress grows quickly immediately after the aggregation begins. The rate of

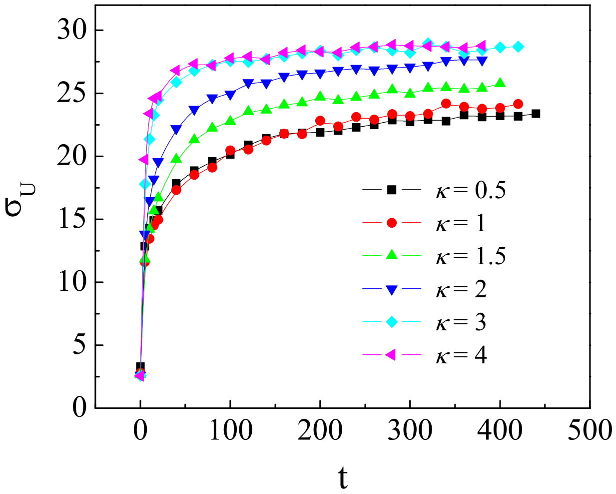

Figure 3.13: Evolution of the isotropic interparticle force stress, σ_U during the aggregation process for $\phi = 0.12$ and various κ, from simulation by ASD; $t \sim a^2/D_0$.

growth slows at $t = 50 - 100$ regardless of the pair potential, and eventually plateaus at $\sigma_{U-plateau}$. Small repulsive barriers lead to more rapid approach to the plateau. At the same ϕ, lower repulsive barriers result in networks with a larger stress.

We note that if each of a pair of particles is located exactly in the potential minimum, there will be no force due to the interparticle potential. Due to Brownian motion and the constraints associated with each pair being part of a complex network, the distance between any pair is typically not at the energy minimum, and thus there is a stress. A detailed investigation shows that the dominant contribution to the stress comes from particle pairs whose distance is less than 2.09 a. Thus the stress is compressive (i.e. it is a positive pressure).

We see also from Figure 3.13 that for fixed ϕ, the stress plateau increases as the repulsive barrier decreases (κ increases). The impact of the particle volume fraction on the stress evolution for $\kappa = 3.0$ is illustrated in Figure 3.14. Higher concentration results in a larger stress. The relation between the stress plateau and the volume

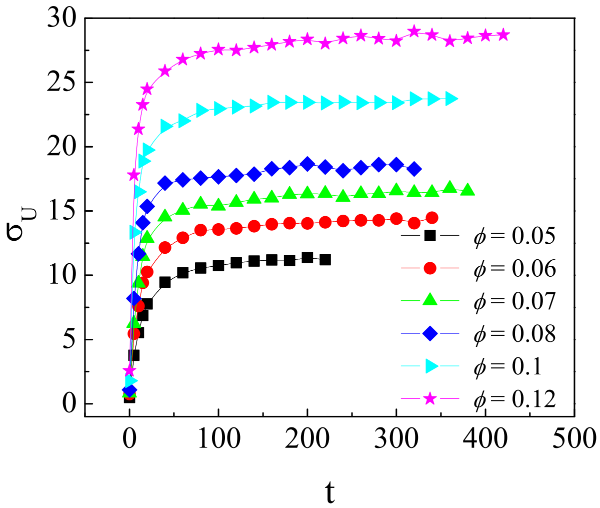

Figure 3.14: Impact of particle volume fraction on stress evolution $\kappa = 3.0$ (ASD); $t \sim a^2/D_0$.

fraction is roughly linear in the range studied, i.e. $\sigma_{U-plateau} \sim \phi$.

The stress plateau for systems of $\phi = 0.08$ and $\phi = 0.12$ with various repulsive barriers is compared in Figure 3.15, for results obtained from both ASD and BD simulation. In both simulation conditions, the stress plateau shows a lower limit for $\kappa < 1$, and an upper limit for $\kappa > 3$. For all conditions studied, the plateau stress due to the interparticle potential is larger for BD than ASD. This result appears to correlate with the more condensed clusters found in BD; note that more condensed clusters and greater inhomogeneity are also found for larger κ, and the stress increases with κ. As discussed in § 3.3, particles form more bonds per particle in the BD simulation for the same condition when compared with ASD. Hence the result is not due to the effect of hydrodynamics in the instantaneous force balance, but instead to the effect of HI in combination with the conservative potential on the structure of the particle network. Considering carefully $g(r)$ in § 3.3.2, the possibilities of particles in $2.1\ a \leq r \leq 3.3\ a$ is higher for low repulsive barriers, suggesting a structural basis for the higher stress plateau.

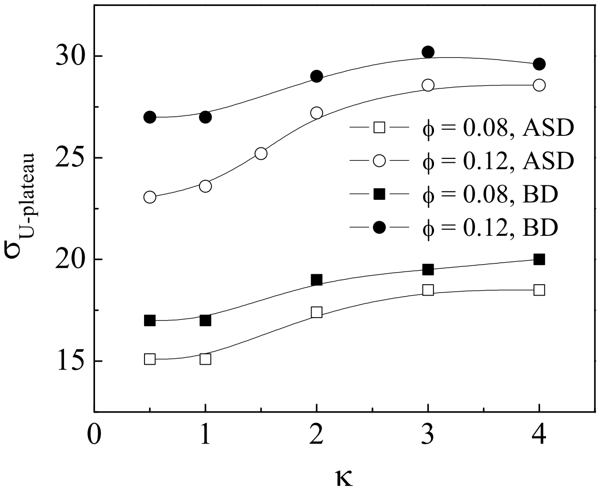

Figure 3.15: Stress plateau as function of κ for $\phi = 0.08$ and 0.12; open dots: data from ASD simulation; solid dots: data from BD simulation.

3.3.6 Percolation

A diagram summarizing the ultimate state (taken for t= 300 a^2/D_0) of the ASD and BD simulation results for $0.04 \leq \phi \leq 0.12$ (4 – 12%) and $\kappa = 0.5 - 4.0$ is shown in Figure 3.16. The separation between the percolated network and un-percolated structures is indicated roughly by the dashed lines in the figure. In general, particles form a percolated network more readily on the scales simulated for potential with lower repulsive barrier. For systems with the same interparticle potential (same κ), the one with hydrodynamic interactions included (ASD) forms a percolated network at a lower volume fraction. The basis for this finding, similar to the result of Furukawa *et al*. [87] for a potential without long-range repulsion, is probed below where we describe our study of isolated groups of three particles.

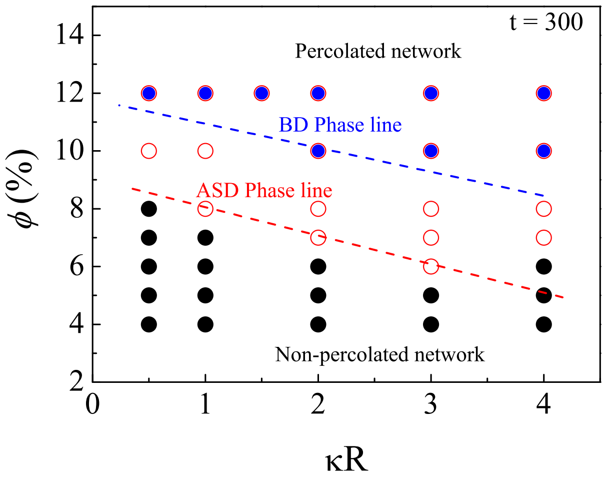

Figure 3.16: Percolation diagram at $t = 300\ a^2/D_0$. Filled blue circles indicate conditions where a percolated network obtained in BD and ASD simulation; open red circles inidicate a percolated network obtained in ASD simulation, but not BD; black circles indicate that an unpercolated structure was found in both methods. Dashed lines represent approximate boundaries between the regions.

3.3.7 Radius of gyration and fractal dimension

Table 3.1: The computed fractal dimension, D_f, for $\kappa = 2.0$ and $\phi = 0.08$, obtained from both ASD and BD simulation. Time is scaled by a^2/D_0.

Time	20	30	60
D_f (ASD)	1.99	2.08	2.08
D_f (BD)	2.07	2.05	2.00

The aggregation process is characterized by particle cluster growth. The size of clusters, as measured by the radius of gyration R_g, may be related to the number of particles N in the cluster by the fractal dimension, D_f. The relationship is $N \sim (R_g/a)^{D_f}$. For primary particles of equal size and same material, the radius of gyration

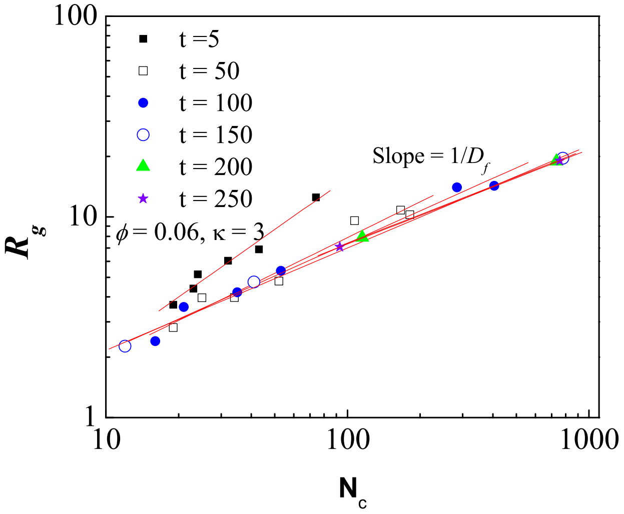

Figure 3.17: Radius of gyration as a function of number of particles N in a cluster at simulation times t = 5, 50, 100, 150, 200, 250 (scaled by a^2/D_0) for $\phi = 0.06$ and $\kappa = 3.0$.

of the clusters can be calculated through the particle positions as [105, 101]

$$R_g = \sqrt{\frac{1}{N}\sum_{i=1}^{N}(\mathbf{r}_i - \mathbf{r}_{com})^2}, \tag{3.7}$$

where $\mathbf{r}_{com}$ is the position of the center of mass of the cluster.

At each simulation time t, each cluster was identified and the number of particles was determined; this was performed by a validated computational algorithm. The radius of gyration of each cluster was then calculated. Values of R_g for a potential with $\kappa = 3.0$ and volume fraction $\phi = 0.06$ are plotted as a function of the number of particles in the cluster for various times from $t = 5$ to $t = 250$ in Figure 3.17. Based on the relation $N \sim (R_g/a)^{D_f}$, we see that $\ln R_g \sim (1/D_f)\ln N$, so that that the fractal dimension may be obtained as the inverse of the slope of $\ln R_g$ plotted as a function of $\ln N$. The results from ASD are indicated in Figure 3.18, which shows that D_f gradually increases as time progresses, eventually reaching a value of

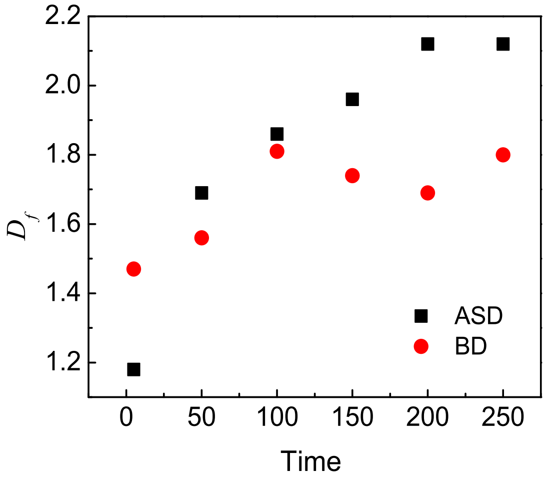

Figure 3.18: Evolution of the fractal dimension, D_f, for $\phi = 0.06$ and $\kappa = 3.0$.

about 2.1. The D_f results from BD simulation for the same system is also shown in this figure, with highest value of about 1.8. As indicated in the percolation diagram figure, this system with $\phi = 0.06$ does not percolate in the BD simulation. A further comparison of D_f results from ASD and BD simulations for $\kappa = 2.0$ and $\phi = 0.08$ is shown in Table 3.1. For this condition, D_f values from ASD and BD simulations are very similar, with values from ASD slightly larger at later times. It is unclear that these results are statistically significant.

3.3.8 Three particle interaction

In order to determine the basis for the coupled influence of hydrodynamic and interparticle forces on aggregation into networks, we have examined the behavior of three particles in isolation, using standard SD and BD simulation techniques, for a limited number of potential interactions. In these simulations, 64 groups of three particles are studied in each case. The groups are sufficiently separated (by 10 radii in each direction) that the triplets do not significantly interact; this has been validated by using larger separations and establishing statistical equivalence of the results.

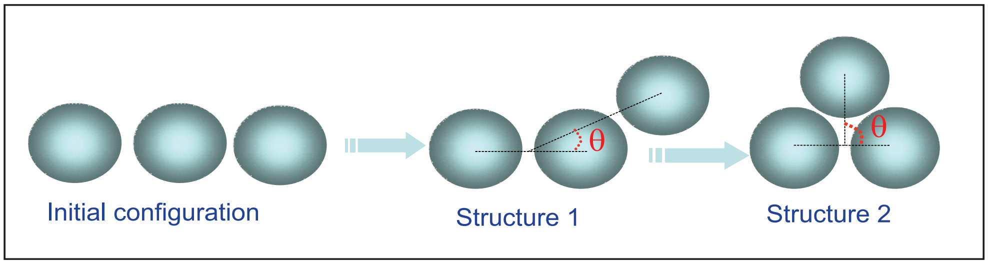

Figure 3.19: Configurations for three particles. Initial configuration, intermediate angular configuration, and highest probability configuration at equilibrium (long time) evolution of three particles.

The initial position of the particles takes the three particles to lie along a line, separated from their nearest neighbor by a center-to-center distance of 2.21 a. The choice of an initially linear triplet is made because access of a third particle to the pair is easiest away from the midplane of this pair, as there is a maximum in the repulsive potential on this plane owing to addition of the repulsion from the members of the pair. The angle from the vector between the first two (arbitrarily choosing one end to be the first of these two) and the vector from the mid-point of the first two to the center of the third particle is denoted θ, as indicated in Figure 3.19; this figure shows the initial linear condition, a small angle intermediate between the initial condition, and $\theta = 90°$, which is the low-energy state and thus the statistically most likely position based on the Boltzmann distribution, $P \sim e^{-U/k_BT}$. This lowest energy state is an equilateral triangle, so that each particle sits at the minimum relative to both of the others. The results of θ from the 64 groups of three particles in an individual simulation (and replicate simulations where applicable) were averaged to give statistically reliable values.

There is a significant difference in the angular probability distribution for θ when we compare SD and BD simulation results. This is true of both repulsive barrier conditions studied, $\kappa = 1$ and 3. The angles from BD simulation have a relatively high probability in the large-angle regime at simulation time $t = 1$, for both $\kappa = 1.0$ and 3.0, as shown in Figure 3.20. Hydrodynamic interaction slows the motion of the triplet toward the minimum energy equilateral position. This maintains a more linear structure to longer times, making access to the condensed triplet more difficult. The peak at angles near 90°, the most likely eventual position as noted above, appears quite early, but is weaker for the SD simulation.

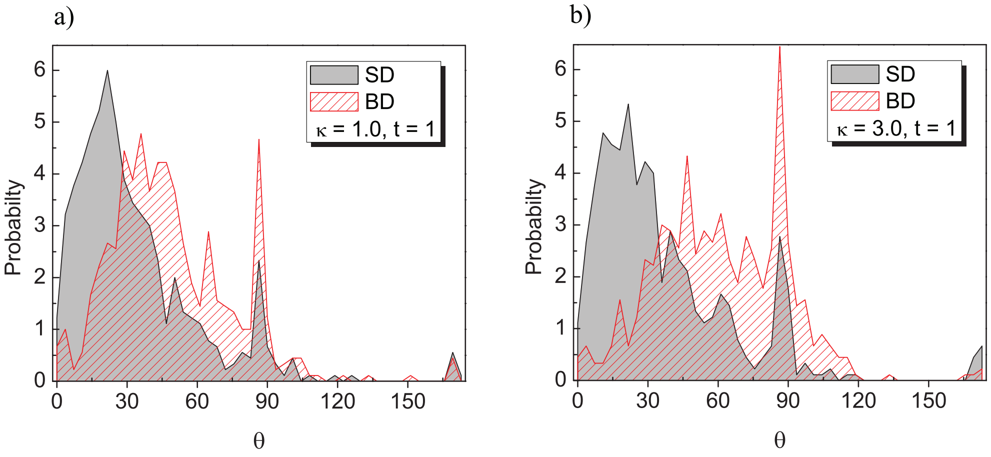

Figure 3.20: Angular probability distribution of three particles obtained from SD and BD simulations at $t = 1$ (scaled by a^2/D_0). a): $\kappa = 1.0$ and b): $\kappa = 3.0$.

Figure 3.21 shows the evolution of the probability distribution for the angle θ, comparing results from SD and BD simulation both at $\kappa = 1.0$. The angular probability distribution evolves more slowly in the SD results, compared with little change observed in the interval $10 \leq t \leq 75$. The majority of 3-particle groups show an open structure, indicated by high probability in $\theta = 0° - 60°$. In the absence of hydrodynamic effects (BD simulation), θ evolves quickly and reaches a relatively stable condition even at $t = 10$, with a symmetric probability distribution of θ from 0° - 180°. Subtle changes can be found as t increases. At long time, most of the triplets are found in a configuration in the range $50° < \theta < 130°$.

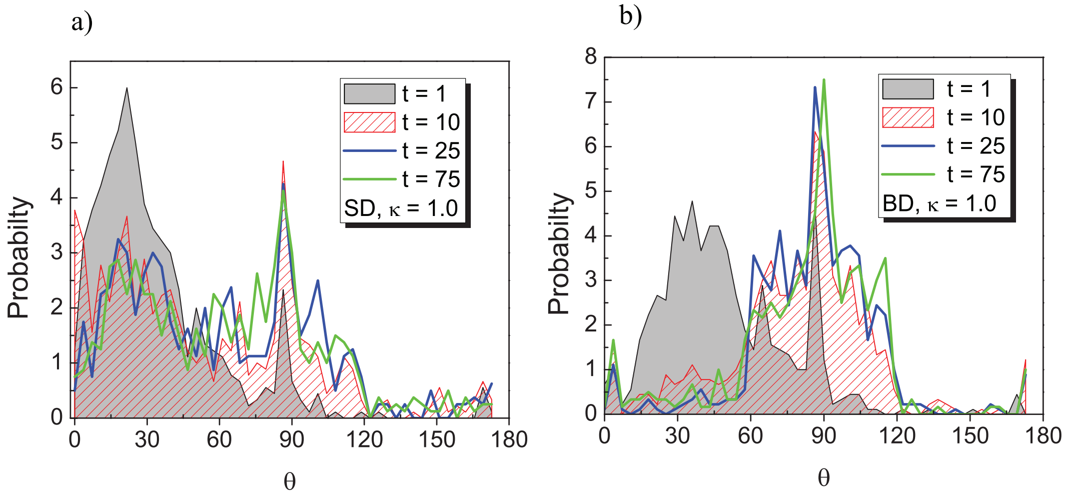

Figure 3.21: Evolution of the angular probability distribution for three particles for the potential with $\kappa = 1.0$; a) SD simulation; b): BD simulation. Time is scaled by a^2/D_0.

While comparing the results from SD and BD simulation, the lubrication effect for two particles near contact needs to be considered. For two rigid particles in relative motion, as one sphere moving past a second stationary sphere in a direction transverse to the sphere axis, the hydrodynamic force caused by the "shearing" motion can be obtained by the lubrication theory [99]. The ratio of timescales predicted by the shearing resistance should be

$$t_{SD}/t_{BD} = \ln(1/\epsilon), \tag{3.8}$$

where ϵ is the ratio of separation between the closet points on the two particle surfaces and the particle radius a. For two particles at their energy minimum ($r = 2.09$), t_{SD}/t_{BD}= 2.4. Figure 3.22(a) shows the comparison between SD and BD for $t_{BD} = 10$ and $t_{SD} = 25$ and 75 with $\kappa = 1.0$. θ shows high probabilities in the range of 0° - 45° for the three-particle groups obtained by SD simulation at $t_{SD} = 25$ and 75 than from BD simulation at $t_{SD} = 10$, which clearly indicates more correlated motions of SD being important, not simply a change in timescale for the same uncorrelated motions.

The comparison between Figure 3.22 and Figure 3.21 (a) shows that, for large κ, the third particle can easily cross over the repulsive barrier and enter into the energy minimum, and large θ values are rapidly populated. As shown in Figure 3.22, the majority of the angular probability lies in the range of 60° - 120°.

We find from this analysis of triplet evolution that both the repulsive potential and hydrodynamic interactions play a significant role in determining the angular structure. The observations from simulation of a dispersion without repulsive interaction by Furukawa *et al.* [87] agree with our observation that hydrodynamics keeps the triplets more open. Their simulations analyzed a more complicated isolated cluster and found a very different evolution when hydrodynamics was accounted properly. It appears from our study that hydrodynamics is influential because it resists local rearrangements which require independent movements of the individual particles. This means that the initially linear triplet is retained because of correlations in motion induced by hydrodynamics. When a long-ranged repulsive potential acts in concert with hydrodynamics, the influence of hydrodynamics arises from the same source: it now appears that the potential becomes more difficult to surmount because of correlated motion: the potential moves with the pair, and rather than a large kick simply moving one particle relative to the other two, there is a component of motion of the cluster center of mass induced. Thus, a fluctuating force must act longer, and this is a lower-probability sequence of events, to drive a particle into the low-energy condensed (equilateral) state. It is the combined effect of both that slows down the third particle moving towards the energy minimum, leading to a more linear structure.

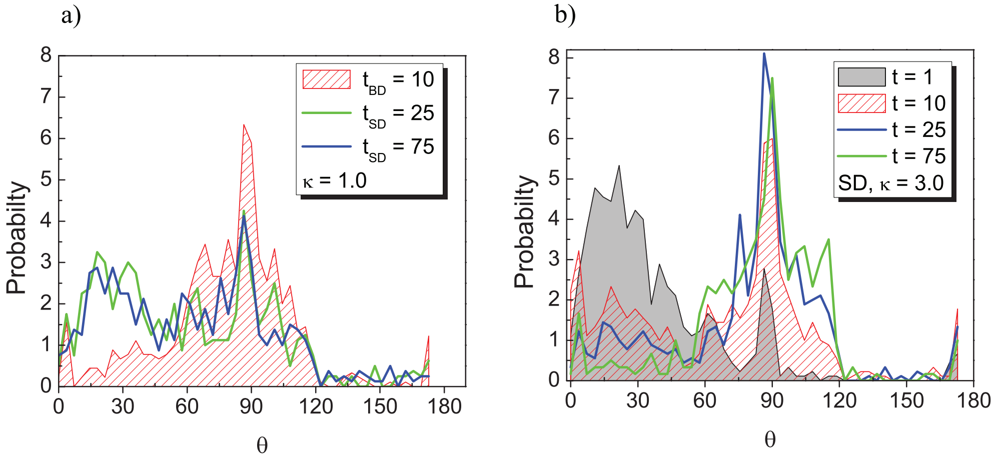

Figure 3.22: a): Comparison of SD and BD results at time scale t_{SD}/t_{BD}= 2.4 for k = 1.0; b): Evolution of angular probability distribution of three particles for the potential with $\kappa = 3.0$, from SD simulation. $t \sim a^2/D_0$.

3.4 Conclusion

By applying two simulation methods, Stokesian Dynamics and Brownian Dynamics, to study the aggregation process in colloidal dispersions, with the methods differing in whether they include the influence of hydrodynamic interactions (HI), this work has shown that HI leads to percolation at lower volume fraction of solids, ϕ. The SD algorithm includes HI while BD considers particle motion influenced by motion relative to the fluid only through a constant drag coefficient. The simulations considered dispersions interacting through both a short-ranged attractive force and long-ranged repulsive 'barrier' force. This models the behavior of charge stabilized dispersions, with the level of the repulsive barrier tunable through the ionic strength in physical experiments [90]. The process of aggregation from initially homogeneously distributed particles is characterized by the development of clusters which exhibit fractal properties. These clusters join and may eventually percolate. While it is our interest to explore the development of structure in gelation processes and understand the influence of the forces working in these systems, we caution that the numbers of particles simulated (and hence the accessible length scales) in this work are not large enough to fully replicate the merging of clusters seen in gelation processes. Hence we retain the terminology of ‘percolate’, rather than ‘gel’.

The formation of structure of the particle network is controlled in large part by the interparticle force. A weak repulsive force is associated with formation of a more closely packed local particle structure, with large fluctuations in number density at large scales, and hence a high compressibility, χ_T as approximated by the small-wavenumber structure factor. The combined effects of a large repulsive barrier and hydrodynamic forces slows the motion of particles into the deep primary minimum of the potential. The slowing down by hydrodynamics is much more than can be captured by a simple rescaling by the squeeze-flow lubrication interaction: a factor of about 2.4 in slow-down is expected in the pair motion along line of centers at $r/a = 2.09$ relative to the simple constant Stokes-Einstein drag interaction used in our Brownian Dynamics simulations, but in our three-particle simulations we see the approach to an equilibrium distribution at a much smaller rate than predicted by this scaling. These three-particle studies reveal that the correlated motions induced by hydrodynamics make rapid particle rearrangement at the smallest scale, i.e. adjacent to contact, more difficult. This affects the influence of the repulsive barrier in a subtle fashion: passage across the barrier is rendered less likely when part of the thermal motion goes into the cluster center of mass rather than strictly independently into individual particle motions, and this makes the repulsive barrier more effective.

Detailed analysis of local structure shows the coupled influence of hydrodynamics and the interparticle potential. The effect of the interparticle potential on the local structure was seen in the radial distribution function, $g(r)$. A large near-contact maximum in g is observed in all conditions, with slight differences in value depending on the repulsive barrier. We observe a reduction in the first minor peak in $g(r)$ when hydrodynamic effects are included (in ASD simulation). The structure of network during the particle aggregation was also monitored at large scale by the evolution of the structure factor, $S(q)$, and in particular by considering its value at small wavenumber, $S(q_{min})$: the latter quantity was observed to increase rapidly toward a plateau whose magnitude was strongly dependent on the interparticle potential. The particle networks are found to have larger heterogeneity on large scales at small repulsive barrier, as noted above in discussion of the compressibility, as $S(q \to 0) \sim \chi_T$. The structure of particle networks is closely related to the bond formation process during the aggregation process. The number of bonds per particle is found to decrease as the repulsive barrier increases. We observe a generally consistent picture that a slowing of the rate of aggregation results in a more open structure.

We conclude by noting that the ability to compare methods with and without HI is critical to analysis of the role of hydrodynamics. This approach was taken by Furukawa *et al.* [87] for simulation of a depletion driven aggregation, without repulsive interaction at long range. This study of diffusion-limited aggregation concluded that hydrodynamics results in a lower-ϕ percolation threshold relative to the artificial physics of a simulation algorithm which neglects this factor. Our work confirms this observation over a wide range of conditions, and shows that there is a coupling of hydrodynamic and interparticle potential effects under reaction limited conditions. As computational power expands, it will be feasible to more accurately capture the structure and properties of gelation processes with algorithms inclusive of hydrodynamic interactions, by considering more particles and smaller solid fractions in particular.

Chapter 4

Bonding potential

4.1 Introduction

From our experimental study of the colloidal gelation process, we found that a system can form a gel-like state at a particle volume fraction as low as $\phi = 1$ % and much lower values have been reported [68]. From previous simulation study, a percolated network can not easily form as the particle volume fraction is less than 6 %. The results from simulation are limited in the number of particles compared with experimental data; it may not be able to explore the whole space, instead, restricted to a certain portion of the real gel network. Our investigation also shows that in order to obtain a percolated network with fractal dimension $D_f = 2.0$ for a system with volume fraction $\phi = 1.0$ %, at least 10,000 primary particles are needed for simulation investigation, obtained by (1.8) and (1.11). In real experiments, particles in the suspension may actually form a bond that restrict them from coarsening and form clusters with more linear chain-like structure, which interconnect with each other to fill the whole space and finally form a gel. To describe this type of particle interaction, bonding potentials are induced [7, 48, 49], which takes place at a relatively short distance (near contact). The interaction between particles through bonding potential is usually very strong; once formed, it is hard to break the bond.

Based on the degrees of restrictions in the particle motion and the reversibility of the bond formation, the bonding potential can be classified into non-restrictive and restrictive bonding. For the first type, the non-restrictive bonding potential takes place when the distance between two particles is within a critical 'bonding distance' r_b, a distance slightly bigger than the one of energy minimum r_{min}. This type of bonding potential acts on the center of particles, which allows the rotational motion of the particle pair and the stretch of the bonding. Most pair of particles stay in the energy well once they form a bonding between them. In some occasions where the external disturbance is high, the bond between two particles can be broken, with a distance greater than r_b. The FENE (finitely extensible nonlinear elastic) potential, with form illustrated in Figure 4.1, is harmonic at its minimum but the bonds cannot be stretched beyond a maximum length determined by a characteristic length r_0. It is one kind of potential to describe the reversible bonding interaction between particles. Seaton *et al.* and Sánchez *et al.* [48, 49] used FENE potential to simulate the bonding between particles in chains. Koplik *et al.* [50] applied FENE potential to group atoms into freely jointed chain molecules having four atoms in length in their molecular dynamics simulation. Spring potential, with form illustrated in Figure 4.2, was used to describe the bonding between solid atoms and two layers of fcc lattice sites at a molecular scale [50]. Also the spring potential was used to describe the hydrogen binding force between biotin ligand and residues at macromolecular scale [106]. We apply the same concept of spring potential to describe the reversible bonding between colloidal particles. Compared with the FENE potential, the spring potential has relatively strong bonding force even through the two particles are very close to each other, as illustrated in Figure 4.1 (b) and 4.2 (b).

Compared with the non-restrictive bonding potential, the restrictive bonding potential is irreversible; once formed, the bond is permanent and cannot be broken by external forces. Both the rotational and translational motion of a particle are constrained by the position or the motion of other particles, which connect the particle through the restrictive bonding. In the latter part of this chapter, we applied the spring-type of bonding potential to represent the irreversible bonding, which acts on the surfaces of two particles, instead of the centers of particles. Whittle *et al.* [7] applied a bonding potential to study the gelation of soft sphere particles with irreversible bond formation. They investigated the structure and small-deformation shear rheology of particle gels. An essential part of the restrictive bonding potential is the restriction of rearrangement by the angular motion of particles in aggregates or gels.

Most of this Chapter is focused on the cluster aggregation in two dimensional systems. We applied both Brownian Dynamic (BD) and Stokesian Dynamics (SD) techniques to simulate the particle aggregation process. One particle pair $N = 2$ was applied to study the length of bonding under various potentials. For the system with non-restrictive bonding potential, a total number of $N = 529$ particles in two dimensional systems were investigated with an initial homogeneous distribution in simulation box, various in the length. Due to computational speed, we used $N = 256$ in both two and three dimensional system with restrictive bonding potential. Finally, the results of a three dimensional system with restrictive bonding between particles are presented.

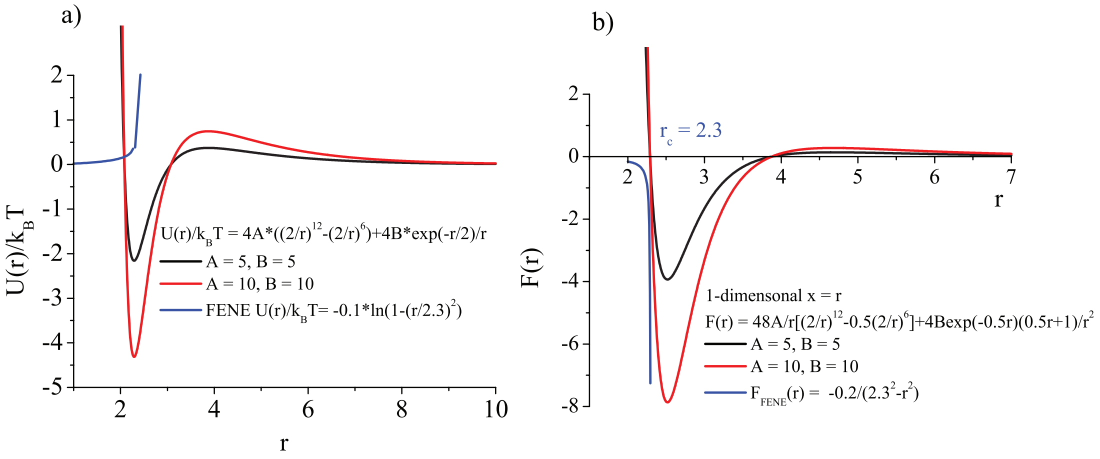

Figure 4.1: Lennard-Jones-Yukawa potential and FENE potential

4.2 Non-restrictive bonding potentials

4.2.1 Interparticle Potentials

We used two dimensional Brownian Dynamics to investigate two types of bonding potentials 1) Non-restrictive bonding; 2) Restrictive bonding. For the first case, we studied the effect of a FENE potential and spring potential (with restrictions only on the distance between two particles) on the structure of clusters during aggregation. For the second case, we probe a special spring potential with restrictions both on the distance between a pair of particles and on the rotational motion of the pair. Brownian Dynamic simulation (described in Chapter 3) was applied to investigate the particle aggregation under various potentials in two-dimensional systems. The main potential form existing between particles is the Lennard-Jones (L-J) potential with or without the long-range repulsive Yukawa potential. An additional potential, the bonding potential, applies when two particles approach below a certain distance $r \leqslant r_c$. The types of potentials ($U(r)$) can be expressed as:

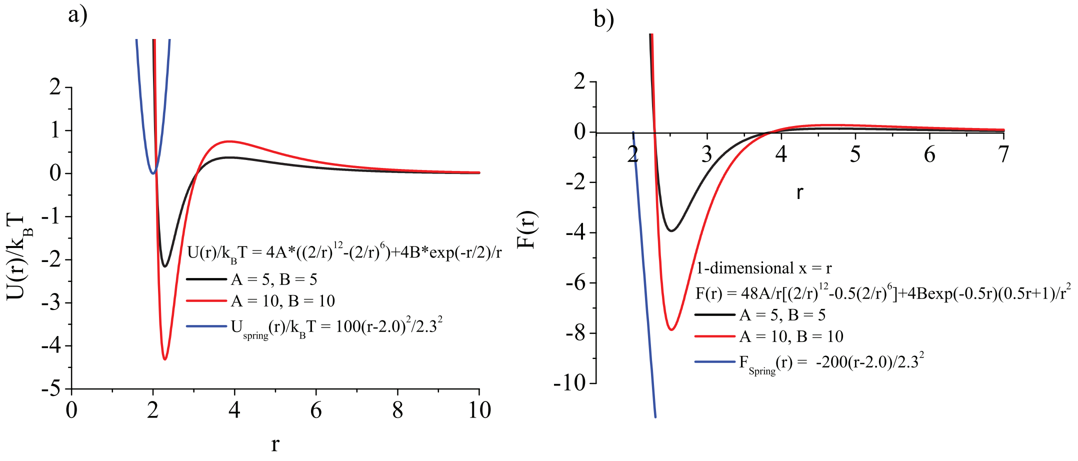

Figure 4.2: Lennard-Jones-Yukawa potential and spring potential

Lennard-Jones potential,

$$U(r)/k_BT = 4A[(\frac{2a}{r})^{2n} - (\frac{2a}{r})^{n}]; \tag{4.1}$$

Yukawa potential,

$$U(r)/k_BT = 4Be^{-r/2}/r; \tag{4.2}$$

FENE potential,

$$U_F/k_BT = -a\ln[1 - (r/r_0)^2] + u_f; \tag{4.3}$$

and spring potential

$$U_S/k_BT = b(r - r_1)^2/r_0^2 + u_s, \tag{4.4}$$

where k_BT is the thermal energy, $2a$ is the diameter of the primary particles, r is the particle pair center-to-center distance, A, B, n, a, b, r_0, r_1, u_f, u_s are parameters determining the form of the potentials. Typical forms of Lennard-Jones-Yukawa (L-J-Y) potential with FENE or spring potential are shown in Figure 4.1 and Figure 4.2, with parameters $a = 0.1$, $r_0 = 2.3$, $b = 100$, $A = 5$, 10 and $r_1 = 2.0$. u_f and u_s are constants and will not affect the force form deriving from the potential $\mathbf{F} = -\nabla U(\mathbf{r})$ ($\nabla u_f = \nabla u_s = 0$).

4.2.2 Bond length in different potentials

A direct way to observe the impact of various potentials on the particles is to study an isolated pair of particles. Figure 4.3 shows the interparticle distance of two-particle system with various potentials between them as function of the simulation time. This is a two-dimensional calculation. The initial distance between the two particles was set to be $r_0 = 2.3$ a, in the energy minimum of the potential. It is shown in the figure that, without interparticle forces, due to Brownian motion, the distance between the pair is very random, varying from to $r = 2.3$ - 6.8 a and generally increasing with time. In the Lennard-Jones potential, interparticle distance fluctuates around $r = 2.3$ a. In an ideal case, with only FENE potential, the distance between the two particles is near $r = 2.0$ a.

4.2.3 Structure evolution of clusters with FENE or spring bonding potentials

Particles with $N = 529$ are initially randomly distributed in with a two-dimensional square simulation box of side length 84 radii. They move due to Brownian motion, under the influence of the interparticle potential. When particles approach each other within a certain distance, the attractive bonding force will bring them

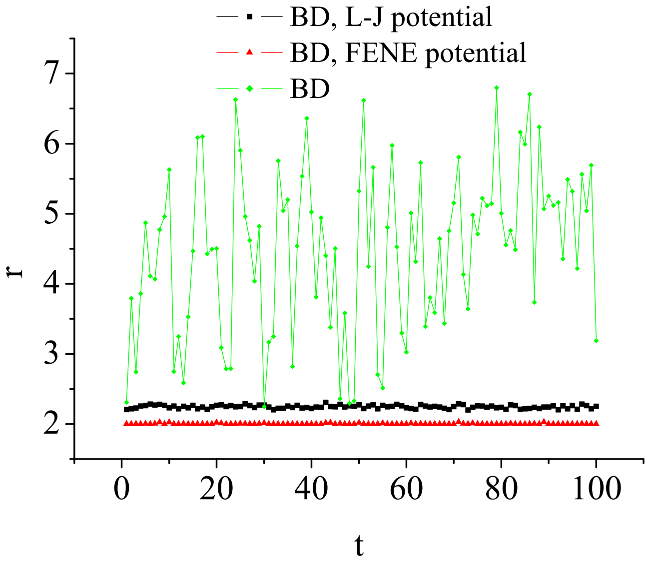

Figure 4.3: Interparticle distance of a pair of particles under various potentials.

closer, into the energy minimum. Their relative motion is then restricted within the energy well. This section investigates the evolution of particle aggregates in two dimensions and their structures under various potentials.

Non-repulsive potential with non-restrictive bonding

Figure 4.4 shows the difference in the evolution of clusters during the aggregation process in systems without repulsive barrier ($A = 5$, $B = 0$). Two types of non-restrictive bonding potential were studied: FENE and spring potentials ($a = 0.1$, $r_0 = 2.5$, $b = 100$ and $r_1 = 2.0$). The systems start with homogeneously distributed particles, which aggregate into large condensed clusters without bonding potential; while systems with bonding potential develop more linear and chain-like clusters. Under the impact of FENE potential, clusters undergo structure rearrangement, showing more crystallized structure at later time. With spring

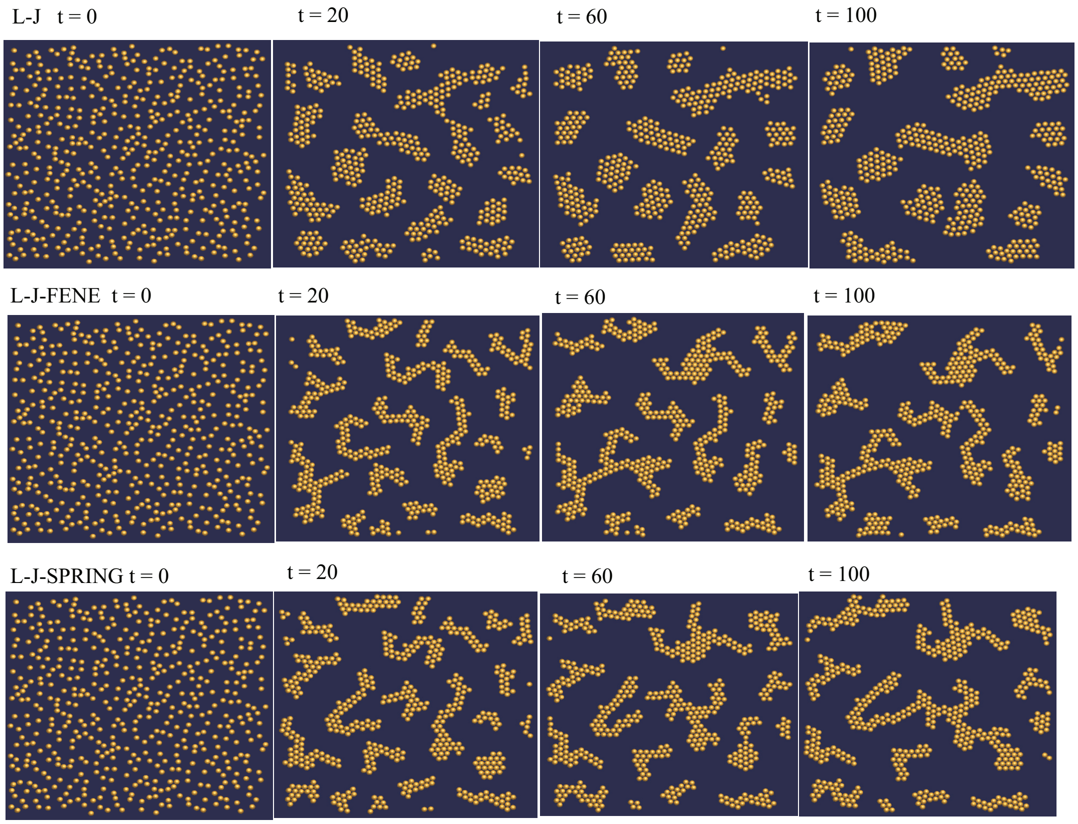

Figure 4.4: Evolution of clusters for systems with non-repulsive potential (L-J potential) with or without the bonding force (FENE and spring potentials);$A = 5$, $a = 0.1$, $r_0 = 2.5$, $b = 100$ and $r_1 = 2.0$.

potential, the aggregates do not lose as much linearity in structure. Instead, the clusters interconnect with each other during evolution and form large fractal objects.

The FENE potential is efficient in bringing the two approaching particles together. As the two particle get closer, the bonding force suddenly becomes weak. There is not enough bonding force to restrain the particles in their initial position, allowing structure rearrangement for clusters to explore the minimum energy. For systems with the spring potential, the bonding force is sufficiently strong to maintain two particles within the bonding distance, leading to the formation of large clusters with ramified structure, as shown in Figure 4.4. At same simulation time $t = 60$, the system with FENE bonding potential displays smaller scattered aggregates, compared with the larger fractal clusters for system with spring potential.

Repulsive potential with non-restrictive bonding

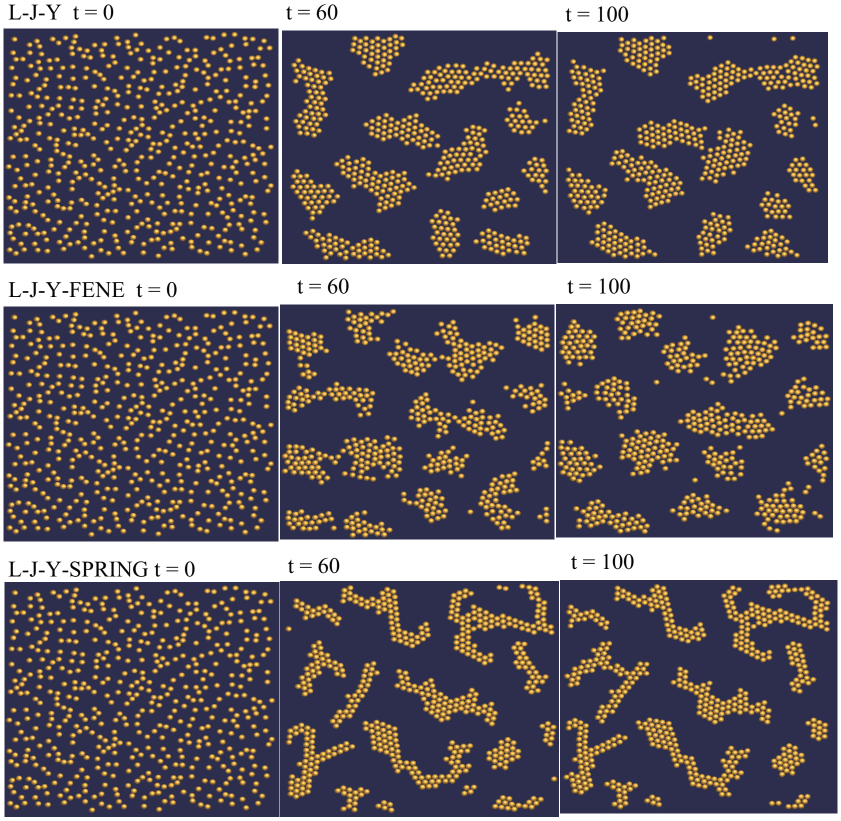

Figure 4.5: Evolution of clusters for repulsive potential and various bonding force. $A = 5$, $a = 0.1$, $r_0 = 2.5$, $b = 100$ and $r_1 = 2.0$

.

The structure evolution of clusters for systems with repulsive barrier (L-J-Y potential, $A = 5$ and $B = 5$) and non-restrictive bonding potentials (FENE and spring potentials, $a = 0.1$, $r_0 = 2.5$, $b = 100$ and $r_1 = 2.0$) are shown in Figure 4.5. When applying the FENE bonding potential, particles evolve into separate clusters with loose structure, which do not interconnect with each other as they evolve. Instead, large clusters split into small aggregates with more free primary particles (when compared at $t = 60$ and $t = 100$). This observation can be related with the findings in experiments, where stable diffusing clusters are found in regions of phase space near the gel transition line [107]. Particles in the clusters are charged. Clusters growing to a certain size accumulate enough charge to repel additional particles; this long-range repulsion introduces a second length scale, the characteristic maximum cluster size [6, 45]. The repulsive force in the simulation models the extra charge which prevents the aggregation of clusters. For the systems with spring potential, clusters show chain-like structure, which interconnect with each other to form large fractal aggregates as the systems evolve. A careful observation indicates that those fractal objects undergo structure rearrangement locally. Compared with FENE potential, the spring bonding potential has a better effect on simulating the bonding force to form a chain-like network structure.

4.2.4 Impact of particle concentration

From the previous investigation just discussed, the spring potential is found to be the most effective in representing the chemical or physical bonding between particles to form a chain-like network, which may percolate when the particle concentration is above a certain level. Three different particle concentrations were studied for a non-repulsive potential and spring bonding potential. The three simulation box sizes have size length $l = 60$, 70 and 84 radii, with $A = 5$, $b = 100$, $r_1 = 2.0$, and $r_0 = 2.5$ in the potential form. The particle volume fraction is calculated through $\phi_a = N \cdot \pi a^2/l^2$, which is $\phi_a = 0.46, 0.34, 0.24$ for the simulation boxes studied. The results are shown in Figure 4.6. For volume fraction $\phi_a = 0.46$, the particles form a large condensed cluster, which fills the whole space even at early time $t = 5$. The structure of the cluster does not change much except for some local rearrangement as the systems evolves (box size $l = 70$). For dilute systems, small clusters form at early time; these

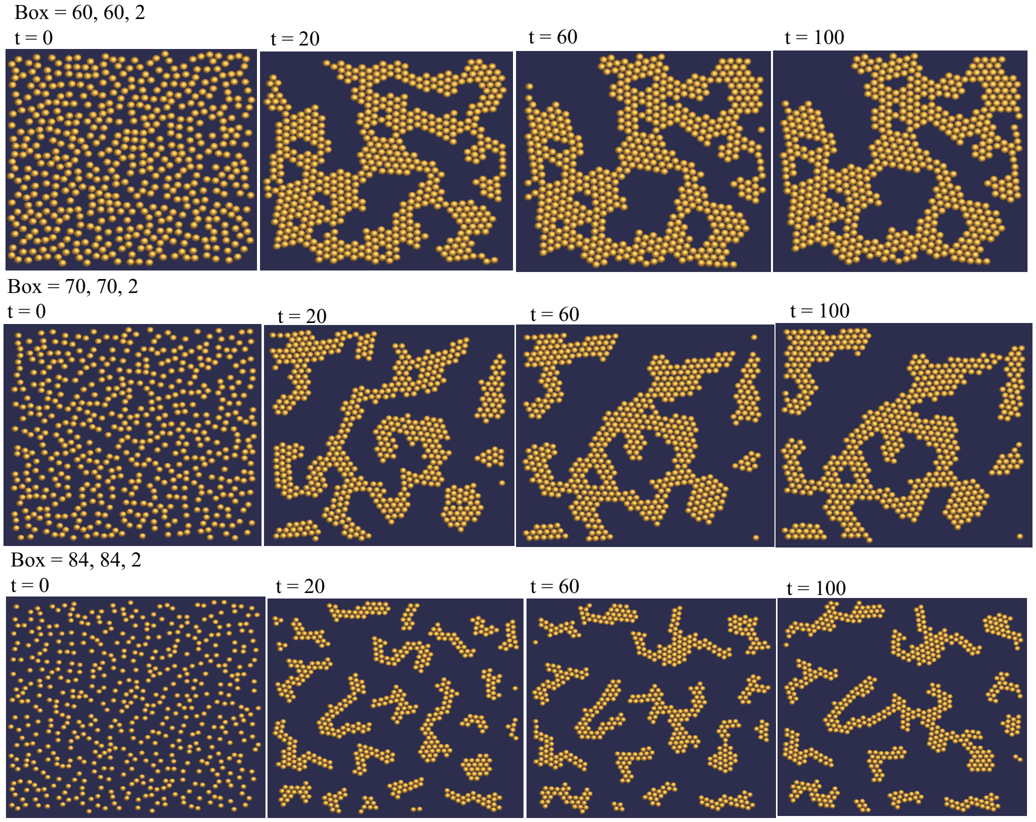

Figure 4.6: Evolution of clusters for various particle volume fraction. A = 5, b = 100, r_1 = 2.0, r_0 = 2.5, and ϕ_a = 0.46, 0.34, 0.24, representing box of 60, 70 and 84.

connect and evolve into large clusters at late time. In order to form a cluster that fills the whole volume, the particle concentration should be above some critical value.

4.2.5 Effect of the strength of the bonding force

The effect of the bonding strength of the spring potential was investigated for systems with L-J potential. Figure 4.7 shows the structural evolutions of clusters with bonding potential of various strength, characterized by b = 100, 200 and 300. For low spring force b = 100, particles form clusters with chain-like structure at early aggregation time t = 20, which evolve into condensed structure at late time t = 60 and 100. For high strength b = 200, small clusters attach to large ones

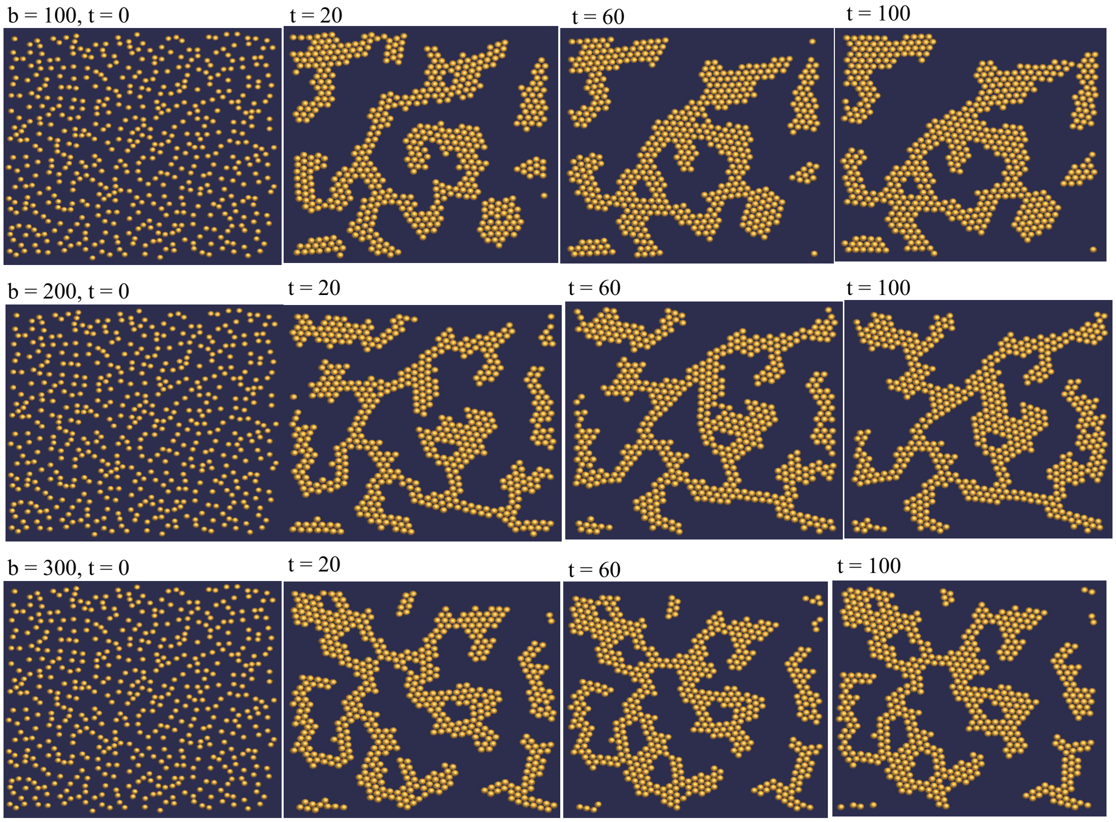

Figure 4.7: Evolution of clusters for different strength of bonding force $b = 100, 200, 300$, $A = 5$, $r_1 = 2.0$ and $r_0 = 2.5$.

during aggregation, with smaller changes in the linearity of the structure. Particles aggregate into a large cluster quickly at $t = 20$, which does not evolve much in the structure, for $b = 300$. The local rearrangements of particles in clusters have a strong dependence on the strength of the interparticle bonding during structure evolution. Images with periodic particles at time $t = 100$ are shown in Figure 4.8, which reveals the percolation information. Only the system with bonding strength $b = 200$ forms a percolated network in both x and y directions.

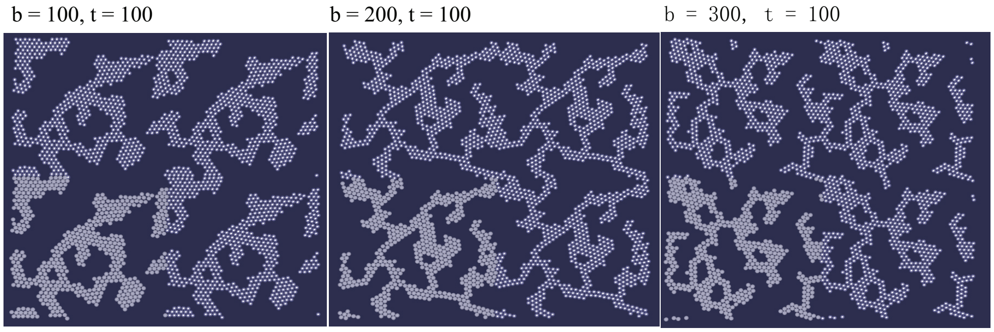

b = 100, t = 100 b = 200, t = 100 b = 300, t = 100

Figure 4.8: Images of percolated network with spring bonding potential with various strength of bond coefficient b, $A = 5$, $r_1 = 2.0$, $r_0 = 2.5$, $t = 100$.

4.3 Restrictive bonding potential

In Brownian Dynamics simulation, the angular motion of the particles is not usually calculated during the aggregation process. In order to probe the constraint on the angular motion due to the restrictive bonding potential, Stokesian Dynamic simulation is applied. From our previous study, it is shown that a gradually coarsening particle network will form when the generalized L-J potential plus a Yukawa potential is applied to model the particle interaction. In addition, for a three-dimensional system, an arrested network will form for particle volume fraction $\phi \geq 6$ %. However, for particle volume fraction $\phi < 6$ %, the systems will generate large aggregates which can move freely in the space.

Figure 4.9: Schematic figure of the formation of a restrictive irreversible bond between two particles.

It is of interest to know the effect of very strong chemical or physical bonds, which may stop the structure from coarsening. In simulation, we add an additional bonding potential, which reduces relative mobility in aggregating particle systems. In the process of gelation in colloidal suspension, the colloidal particles approach each other to form a chain-like structure. In the restrictive-bonding-potential approach, the rotational motion of each particle in the chains is confined by the bonded particles. The phenomena can be simulated by a bonding potential, between $surfaces\ of$ two particles.

The interparticle bonding is represented by a simple interaction potential, similar with the spring potential, which can be expressed as

$$U_b/k_BT = k_s(r - r_c)^2 - U_0/k_BT. \tag{4.5}$$

It is activated when two particles approach to less than a critical distance r_c. It involves the concept of contact points (A and B in Figure 4.9), which form on the surface of each particle. Only one bond can be formed per particle pair. Once the bond is formed between two particles, it becomes permanent. In other words, bond formation is deemed to be irreversible and once formed contact points on a particle retain roughly the same relative position. The algorithm is as follows:

1. Given the N - particle position $\mathbf{x}^N(t)$, define the separation vectors $\mathbf{r}_{ij} = \mathbf{x}_j - \mathbf{x}_i$.

2. If the particles are within the critical distance for activation of the bonding potential, a) A force is generated due to the bonding potential which will drive the particles towards the equilibrium point r_c between surfaces of two particles, with the force given by,

$$\mathbf{F}_{ij} = -2k_s(|\mathbf{r}_{AB}| - r_c)\mathbf{n}_{AB} = -\mathbf{F}_{ji}. \tag{4.6}$$

b) The torques arise from the bonding potential,

$$\mathbf{T}_{ij} = \mathbf{r}_{CA} \times \mathbf{F}_{ij} \mathbf{T}_{ji} = \mathbf{r}_{CB} \times \mathbf{F}_{ji} \tag{4.7}$$

3. With all forces and torques accounted, particle motions are computed. The particles' positions as well as the vector of contact points ($\mathbf{r}_{CA}$ and $\mathbf{r}_{CB}$) are updated. The form of the main potential, to which the bonding potential is added, is indicated in Figure 4.10 and is given by,

$$U(r)/k_B T = B[(2/r)^{2n} - (2/r)^{2n}] + A \exp(-r/2). \tag{4.8}$$

The parameter A is varied, using 0, 10, 20 and 50, while B =60 and n = 18.

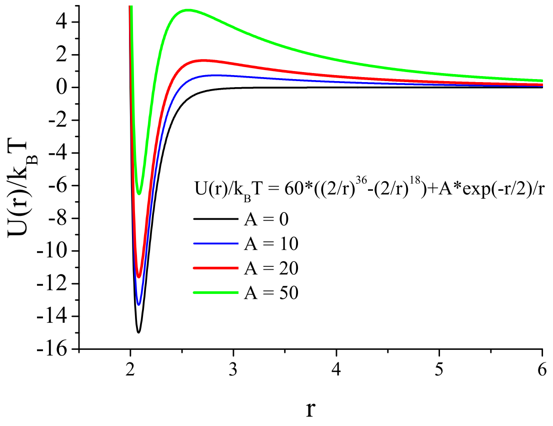

Figure 4.10: Illustration of the interparticle potential (Lennard-Jones-Yukawa) with the parameter A controlling the height of the repulsive barrier and depth of the energy minimum.

Figure 4.11 shows the interaction energy field for a third particle interacting with two particles at a distance of r = 2.09 a, without the bonding potential. The black area represents the excluded volume for a third particle. The cold color (blue to green) surrounding the two particle is the attractive zone; this is surrounded by a repulsive barrier. The color bar on the right indicates the scaled energy value. Region 1 and 2 are distinguished by the height of the repulsive barrier: Region 2 has slightly lower energy. This split of energy field will be used later to explain the particle motion and structure evolution.

Figure 4.11: Energy field of two particles with interparticle potential $U(r)/k_BT = 60[(2/r)^{36} - (2/r)^{18}] + 20\exp(-r/2)$. The distance between two particles (noted by the black area) is the energy minimum 2.09 a.

4.3.1 Effects of the repulsive barrier (2-D SD simulation)

Due to the limitation of the calculation speed in SD simulation, only $N = 256$ primary particles are used to investigate the hydrodynamic and repulsive barrier effect on the structure evolution of clusters in two-dimensional dispersions. The length of the square simulation box is fixed at $l = 50.1$ particle radii ($50.1a$). The volume fraction $\phi_a = N \cdot \pi a^2/l^2$, which equals 0.32. The bonding potential is activated at the critical interparticle distance $r_c = 2.09a$ to avoid sudden change in the interaction force. The spring coefficient k_c is set to be 80, which is large enough to bind two particles within the bonding distance. Images of the cluster evolution are shown in Figure 4.12. The results indicate that the repulsive barrier of the interparticle potential plays an important role in the aggregation kinetics and the structure of the aggregates. Without the repulsive barrier ($A = 0$), particles tend to have more close neighbor particles, generating a condensed cluster structure. Increasing the magnitude and range of the repulsive barrier ($A = 10$, 20, 50) leads to more ramified chain-like structure. Between two particles, the energy minimum, which is denoted with blue color in Figure 4.11, is thermodynamically the most favorable position for the third particle. In order to reach the energy minimum, the shortest distance for the third particle is to overcome the repulsive barrier (Region 1). However, the presence of the repulsive barrier largely reduces the chance of a particle approaching towards the potential minimum. The restriction was seen in the 3-particle simulations of Chapter 3. On the other hand, the possibility of a third particle approaching the two particles from region 2 is higher, leading to the formation of clusters with chain-like structure.

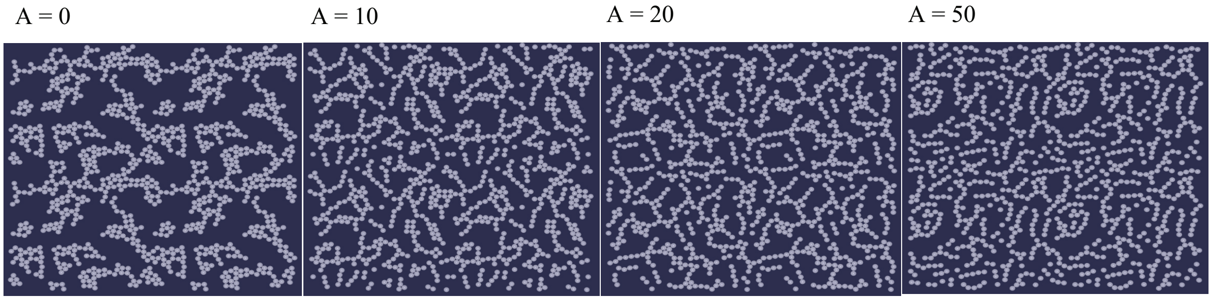

Figure 4.12: Snapshots of clusters for different strength of bonding force ($A = 0$, 10, 20 and 50) and $\phi_a = 0.32$ at time $t = 44$ (scaled by a^2/D_0). The data is shown together with three periodic images.

4.3.2 Bonds per particle (2-D SD simulation)

During the aggregation process, the total number of bonds is counted and divided by the number of particles, to give the bonds per particle. From the images of the systems with different potentials, one can easily deduce that the system without the repulsive barrier yields the largest number of bonds per particle. This is seen in the bonds per particle calculated as function of aggregation time, and shown in Figure 4.13. The systems all start with few bonds per particle, indicating homogeneously dispersed particles. The bonds increase rapidly at the early stage of aggregation. Once large clusters form, the rate of bond formation is greatly reduced due to lower mobility of large clusters and reduced number of isolated particles. The motion of the particles in the system is restrained by the combined effect of the hydrodynamic force and the long-ranged repulsive barrier together with the strong restrictive bonding potential. At late time, the clusters and particles evolve very slowly with little increase in bond formation. Small local movements of the particles continue. In most cases, the bonds per particle is between 1.0 to 1.5. For repulsive barrier with $A = 50$, the bonds per particle is less than 1.0, implying a linear structure with some unbonded particles.

4.3.3 The cross angle θ (2-D SD simulation)

In order to explore more thoroughly the structure of the clusters during the aggregation process, we consider the cross angle θ starting from the midpoint of the two particles to the center of the third particle. A schematic figure of the cross angle is shown in Figure 4.14. A histogram of the cross angle, noted as $g(\theta)$, is developed and normalized by the summation over all angles, as indicated in Figure 4.15; $g(\theta)$ shows a symmetric distribution along angles from $0°$ to $180°$. There is no difference between θ and $180° - \theta$. Three major peaks are found at about $\theta = 41, 90, and 139°$. The angle

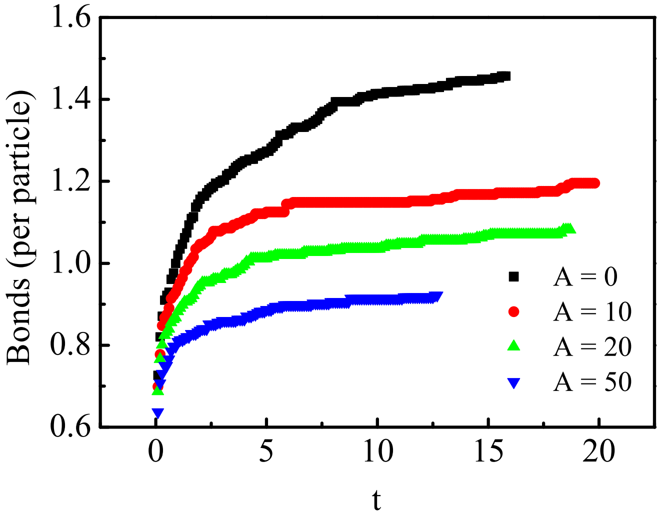

Figure 4.13: Bonds per particle during aggregation process for different strength of bonding force and $\phi_a = 0.32$.

$\theta = 90°$ is the location of the primary potential minimum, which is the favorable distance for the third particle in terms of total energy. The decrease of the peaks along with the increase of the repulsive barrier indicates the enhanced difficulty for the third particle to approach the potential minimum. The peaks at $\theta = 41 and 139°$ indicate some crystal structure formation. $g(\theta)$ is smallest in the range of 60° - 85° and 95° - 120°, in the energy field Region 1. This distribution shows that the repulsive barrier slows the third particle approach to the potential minimum, leading to a more linear structure.

4.3.4 The effects of the repulsive barrier in 3-D SD simulation

The following results from Stokesian Dynamics simulation show the application of the same restrictive bonding potential (as in the two dimensional system) to N

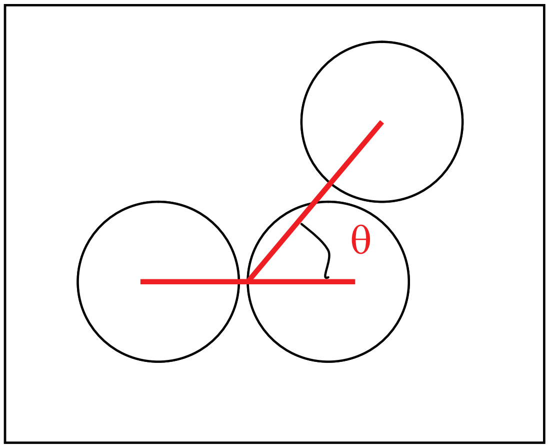

Figure 4.14: Schematic figure of the cross angle.

= 256 primary particles in three dimensions. Snapshots of aggregates for various potential systems of volume fraction $\phi = 0.1$ at $t = 33$ (scaled by a^2/D_0) are shown in Figure 4.16. Particles form large dense clusters for a non-repulsive system ($A = 0$). The clusters shows a more ramified structure for systems with repulsive barriers. For initial particle number as small as 256, the chance of forming a percolated network (connecting to their periodic image in three dimensions) relies on the structure of the largest cluster. We calculated the largest cluster, as shown in Figure 4.17. The particles attaching to the largest cluster strongly depend on the repulsive barrier, which prevents the bond formation of particle networks. The percolation results show that systems of $A = 10$ and 20 are percolated in three dimensions. The reason for system with $A = 0$ not forming a percolated network is that although most particles aggregate, they form a dense structure, with small radius of gyration. The fractal dimension is larger relative to the repulsive cases. For $A = 50$, the failure to percolate is due to the fact that not many particles attach to the cluster, but at much later time, this may change.

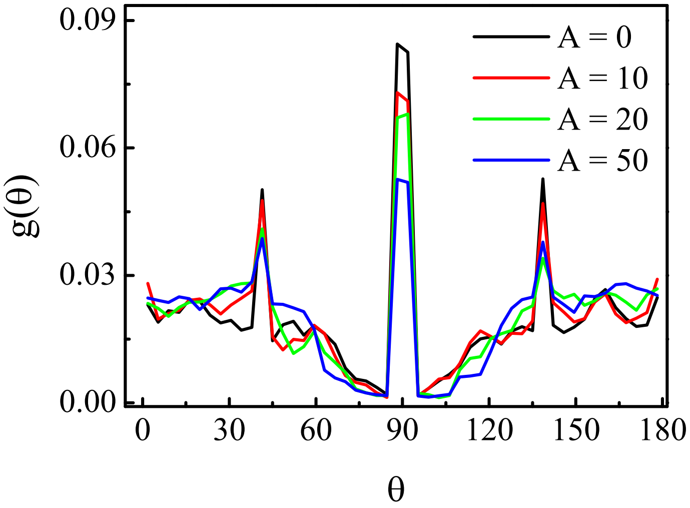

Figure 4.15: The cross angle for various bonding potential for systems with $\phi_a = 0.32$ and time $t = 44$, scaled by a^2/D_0.

4.3.5 Bonds per particle in 3-D SD simulation

Compared with the bonds per particle in a two dimensional system, in three dimensions the result is expected to be higher, and this is generally true, with values between 1.0 to 1.7; however, for the case of high repulsive energy, the bonds per particle is below 1.0. The presence of the repulsive barrier prevents the formation of bonds between particles, leading to a chain-like structure with a small number of bonds per particle. The system seems to reach to a state, where most of the particles and small chain cluster can only move locally without attaching to big clusters and forming a space-spanning particle network.

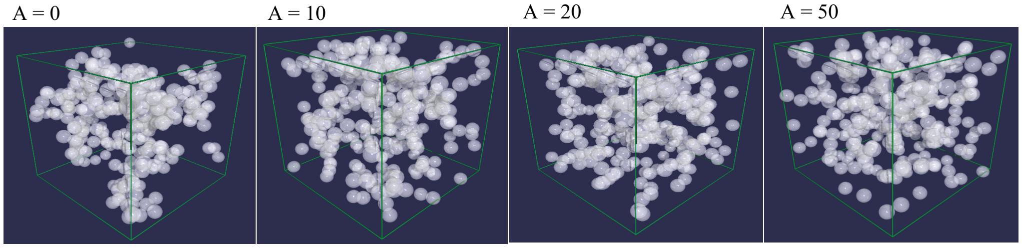

Figure 4.16: Snapshots of aggregates for various repulsive barrier systems of volume fraction $\phi = 0.1$ with restrictive bonding potential at simulation time $t = 33$, scaled by a^2/D_0.

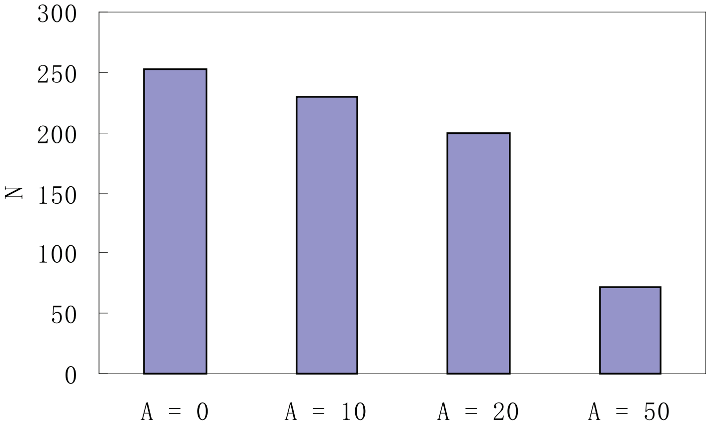

Figure 4.17: Number of primary particles in the largest cluster for various repulsive barrier characterized by parameter A, at $t = 33a^2/D_0$ and $\phi = 0.1$, from SD simulation.

4.4 Conclusion

Two types of bonding potentials (FENE and spring) were studied in a system of $N = 529$ in two dimensional systems. Without the bonding potential, particles form large crystallites. For systems with no repulsive barrier, the bonding force causes particles to evolve into clusters with linear chain-like structure. There are some differences between FENE and spring forces in the case of no repulsive barrier. Particles within the cluster undergo structure rearrangement, which will split into smaller clusters as the system evolves for the presence of FENE potential; for the spring potential, small clusters interconnect with each other to form large clusters.

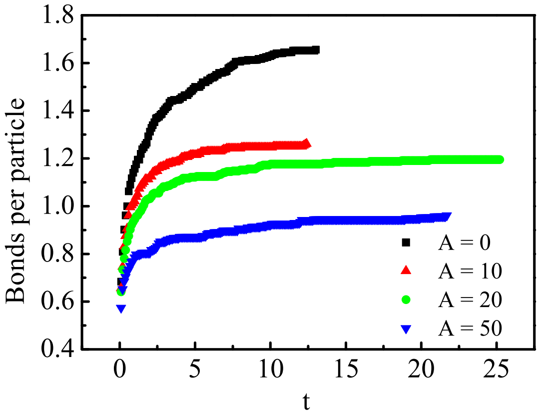

Figure 4.18: The bond evolution of particles with various repulsive potential characterized by parameter A in three dimensional system.

However, with no repulsive barrier, particles with the FENE bonding potential form loose clusters without chain-like structure. The particle volume fraction ϕ_a also affects the structure of clusters. For high $\phi_a = 0.23$, particles form a large cluster that fills the whole space at early time, after which the structure of the cluster evolves little with local particle rearrangement. At low ϕ_a, particles form individual clusters. The strength of the spring bonding potential was also studied. At large spring forces, the largest cluster fills the space and forms a percolated network.

Another type of bonding potential was also investigated, with restrictions in both the rotational and translational motion of the particles. Due to the combined effect of the bonding potential and the repulsive barrier, particles form one dimensional chain-like structure. The structure was further investigated by the application of the angle made by triplets or the “cross angle”, which shows lowest probability of occurrence in the range of 60° - 85° and 95° - 120°. The study of the energy field between two particles reveals that the repulsive barrier determines preference of the position of the third particle both due to kinetic and thermodynamic effects. The effect of the restrictive bonding was also investigated in three dimensions.

Chapter 5

Stress relaxation and frequency dependent rheological properties during the gelation process

5.1 Introduction

In our previous simulational study of Chapter 3 and 4, most results and discussion are focused on the structural evolution of particle clusters. However, in the exploration of gelation, both the structure and the rheological properties are of interest. In this chapter, we present the results of rheological analysis of simulation data.

Our results in Chapter 3 show that the stress increases and evolves into a plateau as the particles form aggregates and finally a space-filling network. It is interesting to learn the stress relaxation as it reflects the visco-elasticity properties of the gel system. The stress relaxation of gel systems has been experimentally explored for many years [108, 109, 78, 110, 111, 76, 112]. Jokinen *et al*. [78] investigated the viscoelastic characteristics of three different sol-gel derived silica gels. They found that the mechanisms of aggregation have an influence on the gel structure. Drabarek *et al*. [76] studied the evolution of storage and loss modulus with/without shear for colloidal silica dispersions. The stress relaxation of aggregated particle systems were also studied numerically [85, 41]. In 1996, Whittle *et al.* [85] simulationally studied the stress response by applying a time-dependent sinusoidal strain $\gamma(t)$ to the system consisting of soft spherical particles. The applied strain was kept small enough not to disrupt the structure. This technique closely mimics the experimental process of small strain oscillatory rheometry. Later Lodge *et al.* [41] applied the small strain limit stress relaxation function $C_s(t)$ to completely describe the linear viscoelasticity response of transit colloidal gels simulated through Brownian Dynamics technique. In the linear viscoelastic regime, where there is a small perturbation by the strain, $C_s(t)$ equals the shear stress autocorrelation function, a statistical mechanical function that quantifies the time dependence of the shear stress fluctuations in an unsheared system [41].

Before going further, a brief introduction about the correlation function is needed to clarify understanding. A correlation function is the correlation between variables (for the same variable A, this is autocorrelation function) in time or space. A schematic figure of fluctuation of variable $A(t)$ as function of time t is shown in Figure 5.1. The time axis is divided into discrete intervals, Δt for the calculation. The time average of variable $A(t)$ is the stationary part, which can be expressed as:

$$< A >= \lim_{T\to\infty}\frac{1}{T}\int_0^T dtA(t) \cong \lim_{N\to\infty}\frac{1}{N}\sum_{j=1}^{N}A_j, \tag{5.1}$$

where A_j is the value in an interval Δt in Figure 5.1. The autocorrelation function of parameter A is

$$< A(0)A(\tau) >= \lim_{T\to\infty}\frac{1}{T}\int_0^T dtA(t)A(t+\tau) \cong \lim_{N\to\infty}\frac{1}{N}\sum_{j=1}^{N}A_jA_{j+n}. \tag{5.2}$$

This provides the algorithm to calculate the stress relaxation function $C_s(t)$, defined by [23, 41],

$$C_s(t) = (V/k_BT)\langle \sigma_{xy}(0)\sigma_{xy}(t)\rangle, \tag{5.3}$$

where σ_{xy} is the xy-component of the stress tensor σ, xy denotes any two combinations out of the three directions. For each instantaneous configuration, the off-diagonal elements of the stress tensor resulting from the potential can be expressed as:

$$\sigma = \frac{1}{V}\sum_{i=1}^{N-1}\sum_{j+1}^{N}\left(\frac{\mathbf{r}_{ij}\mathbf{r}_{ij}}{r_{ij}}\frac{dU_{ij}}{dr}\right), \tag{5.4}$$

where U_{ij} is the interaction potential between particle i and j. In the linear response regime, the complex shear modulus $G^*(\omega)$ can be calculated as:

$$G^*(\omega) = i\omega\int_0^{\infty} C_s(t)e^{-i\omega t}dt. \tag{5.5}$$

The noted method proposed by Whittle *et al.* [85] applies a sinusoidal strain of form:

$$\gamma(t) = \gamma_0 \sin(\omega t), \tag{5.6}$$

where γ_0 is the magnitude of the strain and $\omega/2\pi$ is the frequency. An integral number of oscillations are applied to obtain a straightforward extraction of the shear moduli, which has the following relationship:

$$\sigma(t)/\gamma_0 = G'(\omega)\sin(\omega t) + G''(\omega)\cos(\omega t), \tag{5.7}$$

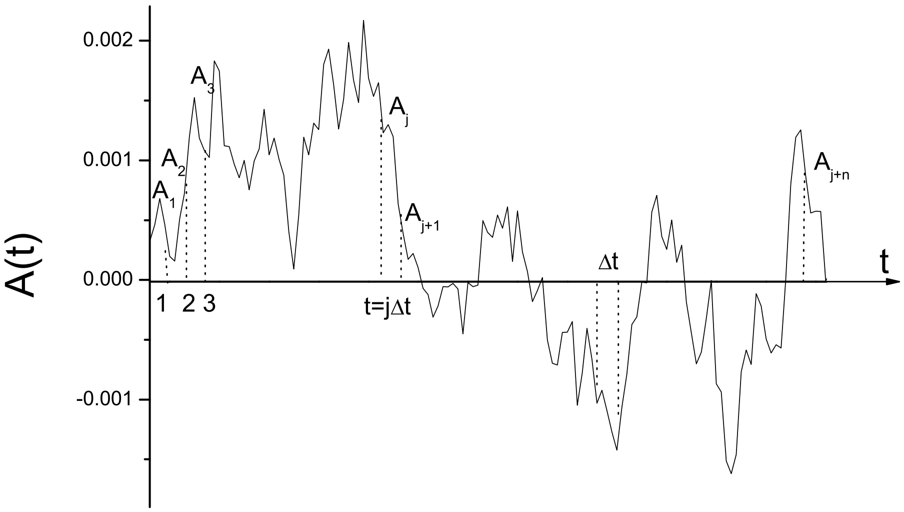

Figure 5.1: Illustration of parameter A as function of time.

where storage modulus G' and loss modulus G'' can be extracted through:

$$G'(\omega) = \frac{\omega}{n\pi\gamma_0} \int_0^{\frac{2n\pi}{\omega}} \sigma(t)\sin(\omega t)dt, \tag{5.8}$$

$$G''(\omega) = \frac{\omega}{n\pi\gamma_0} \int_0^{\frac{2n\pi}{\omega}} \sigma(t)\cos(\omega t)dt. \tag{5.9}$$

In rheology, $G^*(\omega) = G'(\omega) + iG''(\omega)$, where $G'(\omega)$ is the storage modulus representing an elastic part of response and $G''(\omega)$ is the loss modulus indicating a viscous fluid-like response. Systems in which C_s does not decay to zero will induce errors in all frequencies during the calculation of G' and G''. Lodge *et al.* [41] derived a method that allow direct calculation of G' and G'' from the stress tensor, skipping the intermediate step of the stress correlation function.

5.2 Results

The stress relaxation function was investigated in a simulation box containing of $N = 512$ particles through the ASD method, as discussed in Chapter 3. The particle volume fraction studied is $\phi = 0.1$, and periodic boundary conditions are applied. The interparticle potential is as follows:

$$\mathbf{U}(r)/k_BT = A[(\frac{2a}{r})^{2n} - (\frac{2a}{r})^{n}] + B\exp[-\kappa r]/r, \tag{5.10}$$

where $A = 40$, $n = 6$, $B = 40$ and $\kappa = 0.5$.

5.2.1 Shear stress relaxation functions

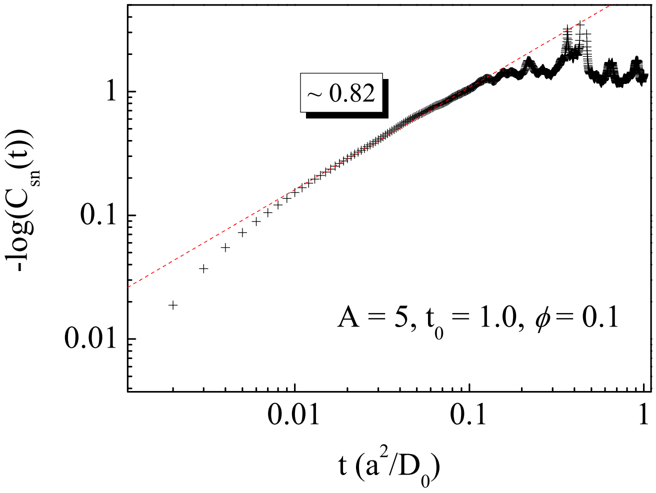

Figure 5.2: The normalized stress relaxation function $C_{sn}(t) = C_s(t)/C_s(0) \sim k_BT/a^3$ for $\phi = 0.1$ and $t = 1.0$ ($t \sim a^2/D_0$).

The small strain limit stress relaxation function, $C_s(t)$, contains a complete

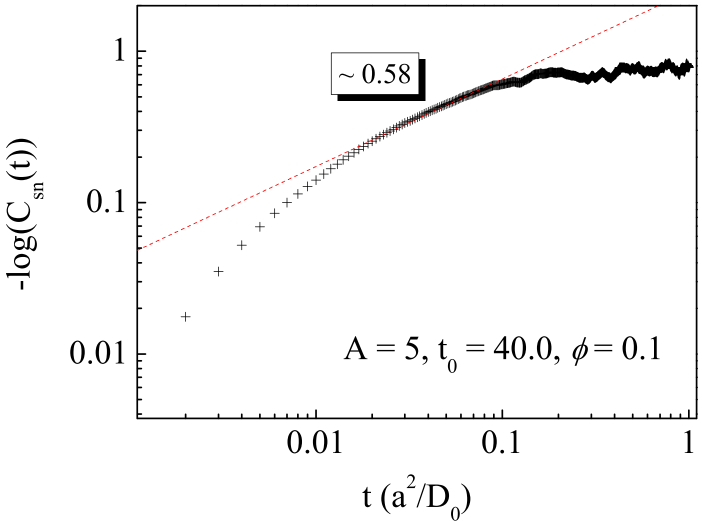

Figure 5.3: The normalized stress relaxation function $C_{sn}(t) = C_s(t)/C_s(0) \sim k_BT/a^3$ for $\phi = 0.1$ and $t = 40.0$ ($t \sim a^2/D_0$).

description of the linear viscoelastic response. Figures 5.2 and 5.3 show a power-law decay of the normalized stress relaxation function $C_{sn}(t) = C_s(t)/C_s(0)$ for $\tau > 0.01a^2/D_0$ for $t_0 = 1.0$ and $t_0 = 40.0$. As indicated by the linear dashed lines in the figures of the log-log plot of $\log(C_{sn}(t))$ vs $\log(t)$, the expression can be written as $C_{sn}(t) \propto t^{-\nu}$. The coefficient ν has a broad range $\nu \approx 0.14-1.00$ in literature [41, 113]. From $t = 1.0$ to $t = 40.0$, ν decreases from 0.82 to 0.58, indicating the formation of viscoelastic materials. At early time, particles aggregate to small clusters, which display rapid relaxation. As the small clusters and other particles evolve into large clusters, which fill the whole space for high volume fraction, the stress fluctuations become highly correlated with a smaller value of ν. Our images and percolation studies also show that the system has aggregated into gel-like network at $t = 40.0$, as seen in Figure 5.5.

The exponential behavior of $C_s(t)$ is also indicated in Figure 5.4 for both $t = 1.0$ and $t = 40.0$. $C_s(t)$ decays to a lower plateau for $t = 1.0$, showing a rapid dissipation of

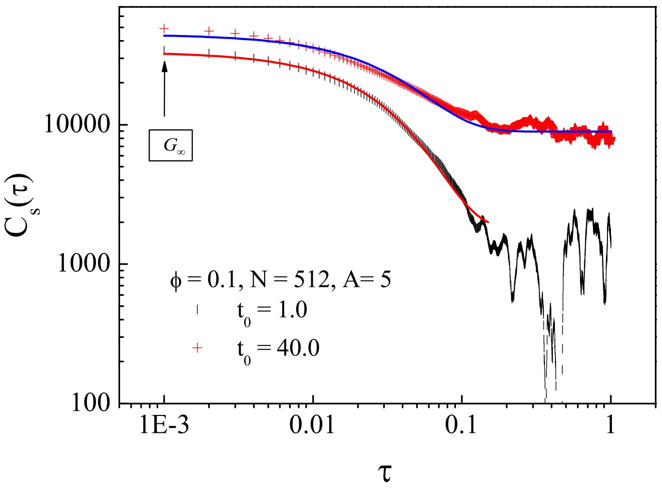

Figure 5.4: Stress relaxation function $C_s(t)$ for $\phi = 0.1$ at $t = 1.0$ and $t = 40.0$ a^2/D_0 during aggregation. Solid lines are fittings to $C_s = C_{s0} + k\exp(-t/\tau)$ ($C_s \sim k_BT/a^3$). For fits, see Table 5.1.

stress, compared with the system at $t = 40.0$. For the unbonded systems, a stretched exponential function is usually applied to describe the stress correlation function. For bonded systems, which relax more slowly at long times, Whittle *et al.* [85] complemented a stretched exponential function with an extra exponential term, which fits their data well. We applied a simpler exponential model to achieve a good fit. The lines in Figure 5.4 show the fittings of exponential decay, $C_s = C_{s0} + k\exp(-t/\tau)$. The values of the parameters in the fitting process is indicated in Table 5.1. This plateau indicates the residual stress, due to the particles forming a percolated network with small mobility.

The value of the plateau was refer to as equilibrium modulus G_{eq} [114], which also reflects a system resisting to an applied shear. For approximation, G_{eq} can be obtained by the plateau of the exponential decay, which equals the value of C_{s0}. Lodge *et al.* showed an increase of G_{eq} with decreasing temperature and increasing particle volume

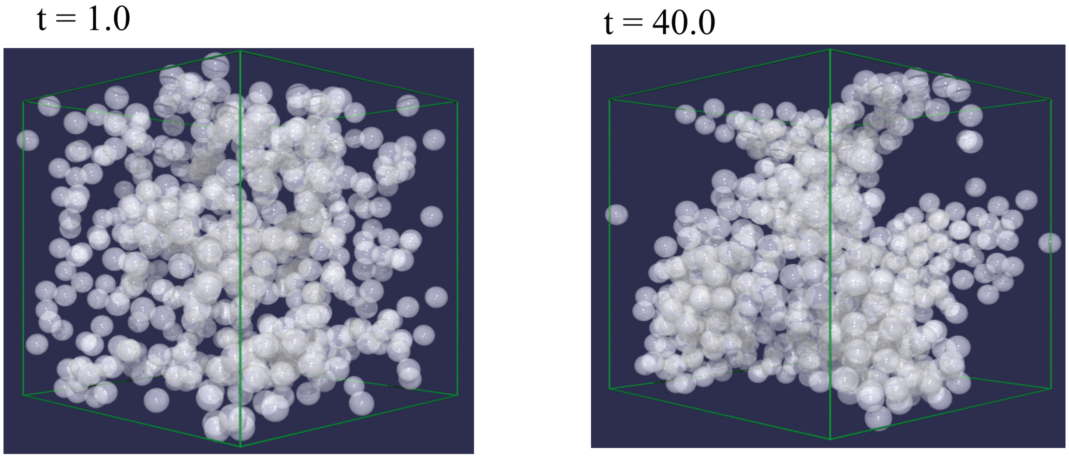

Figure 5.5: Snapshots of aggregates for $\phi = 0.1$ at $t = 1.0$ and $t = 40.0$ a^2/D_0.

[41]. They indicated that G_{eq} is related with the formation of a percolated network or the gel point, and continues to grow after the gel formation [113, 115, 116]. Our data (Table 5.2) show a larger G_{eq} at $t = 40.0$, when large clusters form due to particle interaction. The interconnection between particles in the large clusters contributes to the elasticity of the network. The infinite frequency shear rigidity modulus G_∞ also equals to the value of $C_s(0)$ from the Fourier transform of the stress correlation in equation 5.5, indicated by the arrow in Figure 5.4. G_∞ measures the immediate elastic response of the stress to the strain. Lodge *et al.* indicated that G_∞ is larger and more density-dependent than G_{eq} [41]. They also showed power-law dependence of G_{eq} on time t. The results of G_∞ together with G_{eq} for $t = 1.0$ and $t = 40.0$ are shown in Table 5.2. As the system evolves into large clusters, G_∞ increases from 33950 to 48920.

Table 5.1: Fitting parameters for $C_s/(k_BT/a^3)$ in Figure 5.4, $C_s = C_{s0} + k\exp(-t/\tau)$.

$t_0/(a^2/D_0)$	$C_{s0}/(k_BT/a^3)$	k	$\tau/(a^2/D_0)$
1.0	8937	35616	0.0353
40.0	1784	31536	0.0300

Table 5.2: G_∞ and $G_{eq}/(k_BT/a^3)$ for $\phi = 0.1$ at $t = 1.0$ and $t = 40.0$.

$t_0/(a^2/D_0)$	$G_\infty/(k_BT/a^3)$	$G_{eq}/(k_BT/a^3)$
1.0	33950	8940
40.0	48920	1780

5.2.2 Dynamic modulus

The dynamic moduli G' and G'' were calculated through (5.5) for systems with $\phi = 0.1$ at $t = 1.0$ and 40.0, as shown in Figure 5.6. At $t = 1.0$, when the system forms small aggregates, G'' is greater than G' for low frequency, up to $\omega \cong 20$ (D_0/a^2). G' and G'' cross over at frequency about $\omega = 28$, after which G' increases faster and evolves into a plateau at high frequency. The G' and G'' curves as function of frequency indicate typical behavior of viscoelastic fluid. As the system evolves into large clusters ($t = 40.0$), G' becomes greater than G'' at a lower frequency, with a cross-point at about $\omega = 1$, which is similar to results for gelling dispersions. The system grows into stronger networks at late time, with a larger G' at the later time in experiment. The high-frequency and low-frequency G' and G'' reflects the short-time and long-time response of the stress relaxation [41].

5.3 Conclusion

The stress relaxation function $C_s(t)$ was investigated for a system of $\phi = 0.1$. During the particle aggregation, $C_s(t)$ decays more rapidly at early simulation time with a lower plateau value; while for late time, the decay rate of $C_s(t)$ is less rapid and evolves to a higher plateau. The behavior of the stress relaxation function can be simply described by an exponential decay $C_s = C_{s0} + k\exp(-t/\tau)$. The plateau value of the exponential decay equals the equilibrium modulus G_{eq}, which reflects the ability of the system to resist shear. A high value of G_{eq} indicates a stiff network with

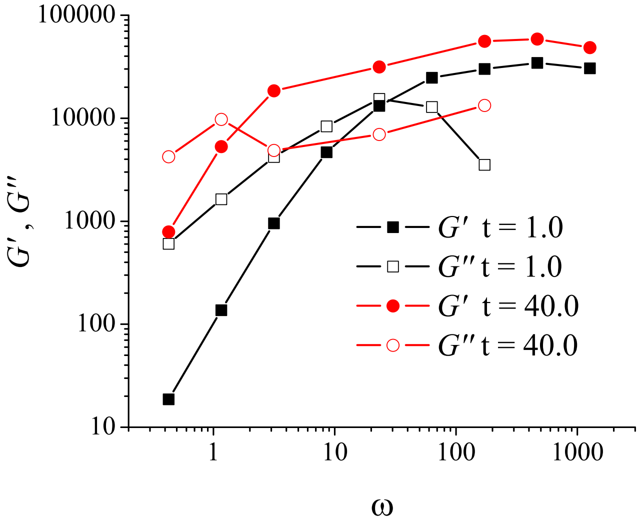

Figure 5.6: G' and G'' ($\sim k_BT/a^3$) as function of frequency ω for system with $\phi = 0.1$ at $t = 1.0$ and 40.0 a^2/D_0.

a yield stress. Another parameter for characterizing the strength of the system is the infinite frequency shear rigidity modulus G_∞, which can be obtained from $C_s(0)$. It measures the immediate elastic response of stress after applying a strain infinitely rapidly.

From the stress relaxation function, the storage modulus G' and loss modulus G'' can be calculated through the Fourier transform of $C_s(t)$, as shown in (5.5). G'' is greater than G' up to frequencies of 28 at early aggregation time $t = 1.0$, indicating a typical fluid-like behavior; while for $t = 40.0$, G' and G'' cross at $\omega \approx 1.0$ with a fast growth for G' after the cross point, which is related with large clusters and large-scale network formation. As small aggregates and clusters continue attaching to the network, the system becomes stiffer, showing an increase in G'.

Bibliography

[1] R. G. Larson, The structure and rheology of complex fluids, Oxford University Press. Inc.

[2] V. Trappe, V. Prasad, L. Cipelletti, D. A. Weitz, Jamming phase diagram for attractive particles, Nature 411 (2001) 772–775.

[3] M. Mellema, J. H. J. van Opheusden, T. van Vliet, Relating colloidal particle interactions to gel structure using Brownian dynamics simulations and the Fuchs stability ratio, J. Chem. Phys. 111 (1999) 6129–6135.

[4] S. Jabbari-Farouji, G. H. Wegdam, D. Bonn, Gels and glasses in a single system: Evidence for an intricate free-energy landscape of glassy materials, Phys. Rev. lett. 99 (2007) 065701.

[5] J. A. Lewis, Colloidal processing of ceramics, J. Am. Ceram. Soc. 83 (2000) 2341.

[6] P. J. Lu, J. C. Conrad, H. M. Wyss, A. B. Schofield, D. A. Weitz, Fluids of clusters in attractive colloids, Phys. Rev. lett. 96 (2006) 028306.

[7] M. Whittle, E. Dickinson, Brownian dynamics simulation of gelation in soft sphere systems with irreversible bond formation, Mol. Phys. 90 (1997) 739–757.

[8] A. S. Zackrisson, A. Martinelli, A. Matic, J. Bergenholtz, Concentration effects on irreversible colloid cluster aggregation and gelation of silica dispersions, J. Colloid Interface Sci. 301 (2006) 137–144.

[9] J. Baileya, T. Nagasea, S. Broberga, M. Mecartney, Microstructural evolution and rheological behavior during the gelation of ceramic sols, J. Non-Cryst. Solids 109 (1989) 198–210.

[10] R. Buscall, P. Mills, R. Stewart, D. Sutton, L. White, G. Yates, The rheology of strongly-flocculated suspensions, J. Non-Newtonian Fluid Mech. 24 (1987) 183–202.

[11] P. Sandkühler, J. Sefcik, M. Morbidelli, Kinetics of aggregation and gel formation in concentrated polystyrene colloids, J. Phys. Chem. B 108 (2004) 20105C20121.

[12] W. Shih, W. Y. Shih, S. Kim, J. Liu, I. A. Aksay, Scaling behavior of the elastic properties of colloidal gels, Phys. Rev. A. 42 (1989) 4772–4779.

[13] P. N. Pusey, A. D. Pirie, W. C. K. Poon, Dynamics of colloid polymer mixtures, Physica A 201 (1993) 322–331.

[14] M. L. Kilfoil, E. E. Pashkovski, J. A. Masters, D. A. Weitz, Dynamics of aggregated colloidal particles, Phil. Trans. R. Soc. Lond. A 361 (2003) 753–766.

[15] M. G. M. D. Haw, W. C. K. Poon, Effects of phase behavior on the drying of colloidal suspensions, Langmuir 18 (2002) 1626C1633.

[16] L. B. Sandra Rdöner, Effect of crystallization rate and colloidal stability on structural rearrangements during growth of colloidal monolayers, J. Colloid Interface Sci. 265 (2003) 29–35.

[17] N. M. Alford, J. D. Birchall, K. Kendall, High-strength ceramics through colloidal control to remove defects, Nature 330 (1987) 51–53.

[18] L. J. Gauckler, T. Graule, F. Baader, Ceramic forming using enzyme catalyzed reactions, Mater. Chem. Phys. 61 (1999) 78–102.

[19] C. G. d. K. R. Tuinier, Phase separation, creaming, and network formation of oil-in-water emulsions induced by an exocellular polysaccharide, J. Colloid Interface Sci. 218 (1999) 201–210.

[20] M. Lattuada, P. Sandkuhler, H. Wu, J. Sefcik, M. Morbidelli, Aggregation kinetics of polymer colloids in reaction limited regime: experiments and simulations, Adv. Colloid Interface Sci. 103 (2003) 33–56.

[21] E. Dickinson, Structure and rheology of simulated gels formed from aggregated colloidal particles, J. Colloid Interface Sci. 225 (2000) 2–15.

[22] L. G. B. Bremer, B. H. Bijsterbosch, P. Walstra, T. van Vliet, Formation, properties and fractal structure of particle gelsadv. colloid interface sci. 46, 117 (1993), Adv. Colloid Interface Sci. 46 (1993) 117–128.

[23] E. Dickinson, Short-range structure in aggregates, gels, and sediments, J. Colloid Interface Sci. 118 (1987) 286.

[24] E. Dickinson, Structure and rheology of simulated gels formed from aggregated colloidal particles, J. Colloid Interface Sci. 225 (1999) 2–15.

[25] C. J. Lin, K. J. Lee, N. F. Sather, Slow motion of two spheres in a shear field, J. Fluid. Mech. 43 (1970) 35–47.

[26] S. Richter, R. Matzker, K. Schröter, Why do "classical" methods like oscillatory shear rheology and dynamic light scattering for characterization of the gelation threshold sometimes not provide identical results especially on thermoreversible gels?, Macromol. Rapid Commun. 26 (2005) 1626–1632.

[27] Q. Ying, J. Zhang, D. Liang, W. Nakanishi, H. Isobe, Fractal behavior of functionalized fullerene aggregates.i. aggregation of two-handed tetraaminofullerene with dna, Langmuir 21 (2005) 9824–9831.

[28] D. W. Schaefer, J. E. Martin, Fractal geometry of colloidal aggregates, Phys. Rev. Lett. 52 (1984) 2372–2374.

[29] C. Aubert, D. S. Cannell, Restructuring of colloidal silica aggregates, Phys. Rev. Lett. 56 (1985) 738–741.

[30] G. Dietler, C. Aubert, D. Cannell, Gelation of colloidal silica, Phys. Rev. lett. 57 (1986) 3117–3120.

[31] J. E. Martin, Slow aggregation of colloidal silica, Phys. Rev. A 36 (1987) 3415–3426.

[32] M. Carpineti, F. Ferri, M. Giglio, Salt-induced fast aggregation of polystyrene latex, Phys. Rev. A 42 (1990) 7347–7354.

[33] M. Lattuada, H. Wu, M. Morbidelli, Estimation of fractal dimension of colloidal gels in the presence of multiple scattering, Phys. Rev. E 64 (2001) 061404.

[34] J. Innerlohinger, H. M. Wyss, O. Glatter, Colloidal systems with attractive interactions: Evalution of scattering data using hte generalize indirect fourier transformation method, J. Phys. Chem. B 108 (2004) 18149–18157.

[35] H. H. Winter, M. Mours, Rheology of polymers near their liquid-solid transitions., Adv. Polym. Sci. 134 (1997) 165.

[36] Y. Aoki, H. Watanabe, Rheology of carbon black suspensions.3.sol-gel transition system., Rheol. Acta 43 (2004) 390–395.

[37] A. D. Dinsmore, V. Prasad, I. W. D. A. Weitz, Microscopic structure and elasticity of weakly aggregated colloidal gels, Phys. Rev. lett. 96 (2006) 185502.

[38] M. Smoluchowski, Z. Phys. Chem. 92 (1917) 129.

[39] N. Fuchs, Z. Phys. 89 (1934) 736.

[40] T. F. Tadros, Correlation of viscoelastic properties of stable and flocculated suspensions with their interparticle interactions, Adv. Colloid Interface Sci. 68 (1996) 97.

[41] J. F. M. Lodge, D. M. Heyes, Rheology of transient colloidal gels by Brownian dynamics computer simulation, J. Rheol. 43 (1999) 219–244.

[42] E. Zaccarelli, I. Saika-Voivod, S. V. Buldyrev, A. J. Moreno, P. Tartaglia, F. Sciortino, Gel to glass transition in simulation of a valence-limited colloidal system, J. Chem. Phys. 124 (2006) 124908.

[43] G. Foffi, C. D. Michele, F. Sciortino, P. Tartaglia, Arrested phase separation in a short-ranged attractive colloidal system: A numerical study, J. Chem. Phys. 122 (2005) 224903.

[44] M. T. A. Bos, J. H. J. van Opheusden, Brownian dynamics simulation of gelation and aging in interacting colloidal systems, Phys. Rev. E 53 (1995) 5044–5050.

[45] F. Sciortino, S. Mossa, E. Zaccarelli, P. Tartaglia, Equilibrium cluster phases and low-density arrested disordered states: The role of short-range attraction and long-range repulsion., Phys. Rev. lett. 93 (2004) 055701.

[46] P. Charbonneau, D. R. Reichman, Phase behavior and far-from-equilibrium gelation in charged attractive colloids, Phys. Rev. E 750 (2007) 50401R.

[47] A. Kumar, J. Z. Wu, Structural and dynamic properties of colloids near jamming transition, Colloids and Surfaces A: Physicochem. Eng. Aspects 247 (2004) 145–151.

[48] D. T. Seaton, S. J. Mitchell, D. P. Landau, Developments in wang-landau simulations of a simple continuous homopolymer, Brazilian Journal of Physics 38 (2007) 48–53.

[49] P. A. Sánchez, J. J. Cerdà, V. Ballenegger, T. Sintes, O. Piro, C. Holmb, Semiflexible magnetic filaments near attractive flat surfaces: a Langevin dynamics study, Soft matt. 7 (2011) 1809C1818.

[50] J. Koplik, T. S. Lo, M. Rauscher, S. Dietrich, Pearling instability of nanoscale fluid flow confined to a chemical channel, Phys. Fluids 18 (2006) 032104.

[51] M. Carpineti, M. Giglio, Aggregation phenomena, Adv. Colloid Interface Sci. 46 (1993) 73.

[52] D. Ramkrishna, Population Balances, Academic Press, New York, USA, 2000.

[53] S. Ramakrishnan, V. Gopalakrishnan, C. F. Zukoski, Clustering and mechanics in dense depletion and thermal gels, Langmuir 21 (2005) 9917–9925.

[54] J.-Z. Xue, D. J. Pine, S. T. Milner, X. L. Wu, P. M. Chaikin, Nonergodicity and light scattering from polymer gels, Phys. Rev. A. 46 (1992) 6550–6563.

[55] J. G. H. Joosten, J. L. McCarthy, Dynamic and static light scattering by aqueous polyacrylamide gels, Macromolecules 24 (1991) 6690–6699.

[56] T. Coviello, W. Burchard, Criteria for the point of gelation in reversibly gelling systems according to dynamic light scattering and oscillatory rheology, Macromolecules 25 (1992) 1011–1012.

[57] S. Richter, V. Boyko, R. Matzker, K. Schröter, Gelation studies: comparison of the critical exponents obtained by dynamic light scattering and rheology, Macromol. Rapid Commun. 25 (2004) 1504–1509.

[58] Y. Otsubo, Relation between bridging conformation and rheology of suspensions, Advances in Colloid and Interface Science 53 (1994) 1–32.

[59] J. Sefcik, R. Grass, P. Sandkühler, M. Morbidelli, Microstructure and rheological behaviour of electrosterically stabilized silica particle suspensions, Colloids and Surfaces A: Physicochem 190 (2001) 89–98.

[60] J. So, S. Yang, C. Kim, J. C. Hyun, Microstructure and rheological behaviour of electrosterically stabilized silica particle suspensions, Colloids and Surfaces A: Physicochem 190 (2001) 89–98.

[61] V. Trappe, P. Sandkühler, Colloidal gels low-density disordered solid-like states, Curr. Opin. Colloid Interface Sci. 8 (2004) 494–500.

[62] V. Prasad, V. Trappe, A. D. Dinsmore, P. N. Segre, L. Cipelletti, D. A. Weitz, Universal features of the fluid to solid transition for attractive colloidal particles, Faraday Discuss. 123 (2002) 1–12.

[63] W. Götze, L. Sjögren, Scaling properties in supercooled liquids near glass transition, J. Phys. C: Solid State Phys. 21 (1988) 3407–3421.

[64] W. van Megen, S. M. Underwood, Glass transition in colloidal hard spheres: Mode-coupling theory analysis, Phys. Rev. Lett. 70 (1993) 2766–2769.

[65] D. R. Reichman, P. Charbonneau, Mode-coupling theory, J. of Stat. Mech.: Theory and Experiments.

[66] C. Beck, W. Härtl, R. Hempelmann, The glass transition of charged and hard sphere silica colloids, J. Chem. Phys. 111 (1999) 8209–8213.

[67] H. E. Bergna, Colloid chemistry of silica: An overview, Phys. Rev. Lett. 57 (1986) 3117.

[68] M. Y. Lin, H. M. Lindsay, D. A. Weitz, R. C. Ball, R. Klein, P. Meakin, Universal reaction-limited colloid aggregation, Phys. Rev. A 41 (1990) 2005–2020.

[69] C. J. Rueb, C. F. Zukoski, Viscoelastic properties of colloidal gels, J. Rheol. 41 (1997) 197–217.

[70] H. J. M. Hanley, C. D. Muzny, B. D. Butler, G. C. Straty, J. Bartlett, E. Drabarek, Shear-induced restructuring of concentrated colloidal silica gels, J. Phys.: Condens. Matter 11 (1999) 1369–1380.

[71] A. H. Krall, D. A. Weitz, Internal dynamics and elasticity of fractal colloidal gels, Phys. Rev. Lett. 80 (1997) 778–781.

[72] T. Matsunaga, M. Shibayama, Gel point determination of gelatin hydrogels by dynamic light scattering and rheological measurements, Phys. Rev. E 76 (2007) 030401.

[73] G. Dietler, C. Aubert, D. S. Cannell, Gelation of colloidal silica, Colloidal Silica: Fundamentals and Applications (2006) 9.

[74] P. J. Flory (Ed.), Principles of Polymer Chemistry, Cornell Univ. Press, 1953.

[75] H. H. Winter, F. Chambon, Linear viscoelasticity of a crosslinking polymer at the gel point, J. Rheol. 31 (1987) 683–697.

[76] E. Drabarek, J. Bartlett, H. J. M. Hanley, J. L. Woolfrey, C. D. Muzny, Effect of processing variables on the structural evolution of silica gels, Int. J. of Thermophysics 23 (2002) 145.

[77] J. W. Jansen, C. de Kruif, A. Vrij, Attractions in sterically stabilized silica suspension. experimens on phase separation induced by temperature variation., J. Colloid Interface Sci. 114 (1986) 481–491.

[78] M. Jokinen, E. Györvary, J. B. Rosenholm, Viscoelastic characterization of three different sol-gel derived silica gels, Colloids and Surfaces A: Physicochemical and Engineering Aspects 141 (1998) 205–216.

[79] M. J. Snowden, P. A. Williams, M. J. Garvey, I. D. Robb, Phase separation of concentrated aqueous silica dispersions in the presence of nonadsorbed polyelectrolytes, J. Colloid Interface Sci. 166 (1994) 160–167.

[80] L. Lue, L. V. Woodcock, Depletion effects and gelation in a binary hard-sphere fluid, Mol. Phys. 96 (1999) 1435–1443.

[81] M. A. Bevan, S. N. Petris, D. Y. C. Chan, Solvent quality dependent continuum van der waals attraction and phase behavior for colloids bearing nonuniform adsorbed polymer layers, Langmuir 18 (2002) 7845–7852.

[82] E. N. Scheer, K. S. Schweizer, Haloing, flocculation, and bridging in colloid-nanoparticle suspensions, J. Chem. Phys. 128 (2008) 164905.

[83] T. D. Iracki, D. J. Beltran-Villegas, S. L. Eichmann, M. A. Bevan, Charged micelle depletion attraction and interfacial colloidal phase behavior, Langmuir 26 (2010) 18710–18717.

[84] A. I. Campbell, V. J. Anderson, J. van Duijneveldt, Bartlett, Dynamical arrest in attractive colloids: The effect of long-range repulsion, Phys. Rev. Lett. 94 (2005) 208301.

[85]

[86] R. Yamamoto, K. Kim, Y. Nakayama, K. Miyazaki, D. R. Reichman, On the role of hydrodynamic interactions in colloidal gelation, Europhysics Letters.

[87] A. Furukawa, H. Tanaka, Key role of hydrodynamic interactions in colloidal gelation, Phys. Rev. lett. 104 (2010) 245702.

[88] H. Tanaka, T. Araki, Simulation method of colloidal suspensions with hydrodynamic interactions: Fluid particle dynamics, Phys. Rev. Lett. 85 (2000) 13381341.

[89] P. Meakin, Adv. Colloid Interface Sci 28 (1988) 249.

[90] X. J. Cao, H. Z. Cummins, J. F. Morris, Structural and rheological evolution of silica nanoparticle gels, Soft Matter 6 (2010) 5425–5433.

[91] P. Pieranski, Colloidal crystals, Contemporary Physics 24 (1983) 25–73.

[92] E. Zaccarelli, S. Andreev, F. Sciortino, D. R. Reichman, Numerical investigation of glassy dynamics in low–density systems, Phys. Rev. lett. 100 (2008) 195710.

[93] A. Sierou, J. F. Brady, Accelerated Stokesian Dynamics simulation, J. Fluid. Mech. 448 (2001) 115–146.

[94] J. Brady, G. Bossis, Stokesian dynamics, Ann. Rev. Fluid Mech. 20 (1988) 111–157.

[95] M. P. Allen, D. J. Tildesley, Computer Simulation of Liquids, Oxford University Press, 1989.

[96] A. J. Banchio, J. F. Brady, Accelerated stokesian dynamics: Brownian motion, J. Chem. Phys. 118 (2003) 10323.

[97] Q. J. Meng, J. J. L. Higdon, Large scale dynamic simulation of plate-like particle suspensions. part i: Non-brownian simulation, J. Rheol. 52 (2008) 1–36.

[98] Q. J. Meng, J. J. L. Higdon, Large scale dynamic simulation of plate-like particle suspensions. part ii: Brownian simulation, J. Rheol. 52 (2008) 37–66.

[99] S. Kim, S. J. Karrila, Mircohydrodynamics, Dover Publications, Mineola, New York, USA, 1989.

[100] T. W. Healy, Stability of aqueous silica sols, Colloidal Silica: Fundamental and Applications, CRC Press (2005) 247–259.

[101] F. Sciortino, P. Tartaglia, E. Zaccarelli, One-dimensional cluster growth and branching gels in colloidal systems with short-range depletion attraction and screened electrostatic repulsion, J. Phys. Chem. B 109 (2005) 21942–21953.

[102] S. D. Kulkarni, J. F. Morris, Ordering transition and structural evolution under shear in brownian suspensions, J. Rheol. 53 (2009) 417.

[103] S. A. Shah, Y. L. Chen, S. Ramakrishnan, K. S. Schweizer, C. F. Zukoski, Microstructure of dense colloidcpolymer suspensions and gels, J. Phys.: Condens. Matter 15 (2003) 4751.

[104] H. Tanaka, J. Meunier, D. Bonn, Nonergodic states of charged colloidal suspensions: Repulsive and attractive glasses and gels, Phys. Rev. E 69 (2004) 031404.

[105] V. Becker, E. Schlauch, M. Behr, H. Briesen, Restructuring of colloidal aggregates in shear flows and limitations of the free-draining approximation, J. Colloid Interface Sci. 339 (2009) 362–372.

[106] H. Grubmüller, B. Heymann, P. Tavan, Ligand binding: Molecular mechanics calculation of the streptavidin-biotin rupture force, Science 271 (1996) 997–999.

[107] P. N. Segrè, V. Prasad, A. B. Schofield, D. A. Weitz, Glasslike kinetic arrest at the colloidal-gelation transition, Phys. Rev. lett. 86 (2001) 6042C6045.

[108] D. F. Hodgson, E. J. Amis, Dynamic viscoelasticity during a sol-gel reaction, Phys. Rev. A 41 (1989) 1182.

[109] P. A. gren, J. B. Rosenholm, Phase behavior and structural changes in tetraethylorthosilicate-derived gels in the presence of polyethylene glycol, studied by rheological techniques and visual observations, J. Colloid Interface Sci. 204 (1998) 45C52.

[110] R. H. W. Wientjes, M. H. G. Duits, J. W. P. Bakker, R. J. J. Jongschaap, J. Mellema, Linear viscoelastic behavior of enzymatically modified guar gum solutions: Structure, relaxations, and gel formation, Macromolecules 34 (2001) 6014–6023.

[111] B. S. Chiou, S. R. Raghavan, S. A. Khan, Effect of colloidal fillers on the cross-linking of a uv-curable polymer: Gel point rheology and the winter.chambon criterion, Macromolecules 34 (2001) 4526–4533.

[112] G. J. Yin, M. J. Solomon, Soft glassy rheology model applied to stress relaxation of a thermoreversible colloidal gel, J. Rheol. 52 (2008) 785–800.

[113] C. Michon, G. Cuvelier, B. Launay, Concentration-dependence of the critical viscoelastic properties of gelatin at the gel point, Rheol. Acta 32 (1993) 94C103.

[114] R. I. Tanner, Engineering Rheology, CRC Press, Oxford University Press, New York.

[115] D. F. Hodgson, E. J. Amis, Dynamic viscoelasticity during a sol–gel reaction, Phys. Rev. A 41 (1990) 1182C1185.

[116] Derrida, D. S. B., H. J. Herrmann, J. Vannimenus, Transfer-matrix calculation of conductivity in 3d-dimensional random resistor networks at percolation threshold, J. Phys. (France) Lett. 44 (1983) L701CL706.